# PROTECT2024

9th International Colloquium on Performance, Protection & Strengthening of Structures Under Extreme Loading & Events

13 - 16 August 2024 I Singapore

## CONFERENCE PROCEEDINGS

Organised by

NANYANG TECHNOLOGICAL UNIVERSITY SINGAPORE

NTU CEE Alumni Association

# LIST OF TECHNICAL PAPERS

| ID Number | Authors (s) – Paper Title |
|---|---|
| PS-34 | ***Ola Wattad, Hezi Grisaro*** – Performance Evaluation Of Aluminum Foam-Cladded Structures Across A Broad Blast Load Spectrum: Pi Diagrams Analysis |
| PS-36 | ***An He, Dun-Cong Zheng, Qing-Jun Chen, Jia-Bin Ye –*** Influence Of Grouting Defects On The Dynamic Tensile Behaviour Of Grouting Sleeve Connections |
| PS-37 | ***Tusshar Goel, Shashank Pathak*** – Peak Displacement Of Large Structures Subjected To Air Explosions |
| PS-39 | ***Jinxian Lyu, Hao Wu, Gongqing Chen, Yuehua Cheng*** - Residual Axial Capacity Of Grouting Sleeve Connected Precast Concrete Columns After Explosions |
| PS-41 | ***Gongqing Chen, Hao Wu, Jinxian Lyu, De Chen*** - Experimental And Numerical Study On Dynamic Behaviors Of Precast Concrete Composite Slabs Under Blast Loading |
| PS-42 | ***Liangliang Ma, Hao Wu*** - An Insight Into The Blast-induced Collapse Of Simply-supported Highway Bridges Abstract |
| PS-43 | ***Jialu Ma, Wuhan Li, Zhenxing Zhang -*** Fatigue Issues of BFRP Protective Door in Metro Tunnel Subjected to Train-Induced Wind Pressure |

# PERFORMANCE EVALUATION OF ALUMINUM FOAM-CLADDED STRUCTURES ACROSS A BROAD BLAST LOAD SPECTRUM: PI DIAGRAMS ANALYSIS

*Ola Wattad [1] and Hezi Grisaro[2]*

[1] Ph.D. Student, Faculty of Civil and Environmental Engineering, Technion – Israel Institute of Technology. Technion City, Haifa 32000, Israel. olawattad@campus.technion.ac.il

[2] Assistant Professor, Faculty of Civil and Environmental Engineering, Technion – Israel Institute of Technology. Technion City, Haifa 32000, Israel. hezi@technion.ac.il

**Corresponding Author: Ola Wattad.**

Ph.D. Student, Faculty of Civil and Environmental Engineering, Technion – Israel Institute of Technology. Technion City, Haifa 32000, Israel

**Email:** olawattad@campus.technion.ac.il

## ABSTRACT

Among the methods for mitigating blast-induced damage to protected structures (PSs) is the installation of sacrificial claddings on structures under threat. Various materials can be used for these claddings, including Aluminium Foams (AFs). AFs, known for their energy-absorbing properties, effectively reduce peak overpressure from blast loads. Existing research has primarily focused on foams with uniform density, neglecting the coupled dynamic response between the PS and cladding. Moreover, structures that experience plasticity were seldom considered. Previous studies evaluated AF efficiency by comparing structural responses with and without AF. This method inadequately addresses the foam as an active energy absorber, as the AF contributes additional mass to the dynamic system that influences structural deformations, even in a fully compacted state. Furthermore, available research is often limited to specific blast loads, hindering a comprehensive understanding of AF assessments across a broader load spectrum. In this study, a numerical model for predicting the dynamic response of a non-uniform foam PS was developed by employing the shock front theory. The model was utilized to generate pressure-impulse diagrams and better understand the response of the coupled system to blast loads, obtaining unprecedented results regarding the AF effect on the PS.

***Keywords:*** *Blast Mitigation, Structural Cladding, Aluminium Foams, Shock Front Theory, Energy Absorption.*

# INTRODUCTION

Structures within urban landscapes are increasingly vulnerable to extreme loadings, particularly blast loads, which can cause severe damage and necessitate innovative protection methods. Blast loads, arising from accidental explosions or terrorist attacks, pose considerable challenges in structural design due to their extreme overpressure and short duration. Traditional retrofitting approaches, frequently demand substantial alterations to the structural shield, yielding marginal improvements to structural integrity. Post-blast scenarios often require extensive replacements or repairs, prompting a shift in mitigation strategies.

Non-conventional methods to reduce structural damage include the use of novel technologies, such as sacrificial elements formed from various materials with different geometries, which include metallic honeycomb layers, metallic foams, metallic tubes, and even beverage cans [1–5]. Sacrificial layers are used to redirect the damage from the Protected Structure (PS) to the sacrificial layer, i.e. from the structural element to the non-structural and replaceable element. Particularly, the current work is cantered around the intricate properties and applications of Aluminum Foams (AFs).

Metallic foams, particularly AFs, are a set of materials with unique properties and porous structures resulting from their air-cell composition. Extensive research has been conducted on their ability to absorb energy during compression, offering a promising solution to mitigate structural damage caused by blast loads. As the air cells collapse during compression, a lower pressure is transmitted to the PS instead of the extreme pressure generated by the blast wave, resulting in energy absorption capabilities [6].

The compaction of the Aluminum Foam (AF) has been implemented through various models, ranging from simpler, low-ranked models to more sophisticated ones. In the literature, a commonly used model is the Shock Front Theory (SFT), which simplifies the process by envisioning a plastic wave traversing the thickness of the AF, creating a shock front that delineates compacted and non-compacted regimes. Previous works utilizing the SFT made various assumptions about the dynamic system behavior, such as neglecting structural response during AF compaction phase [5, 7–9], assuming a structure that cannot develop plastic hinges [10, 11]. Despite these assumptions, the overarching interpretation from models that used the SFT was that there is an immediate correlation between the mitigation of structural damage and energy absorption, but there was no deeper examination of the underlying phenomena. Moreover, commonly previous works have only examined the foam behavior when considering very specific loads, and focused on foams with uniform densities along their thickness.

One of the methods to investigate the foam performance is through a wide response spectrum of the applied loads, and one of the methods to implement it is through Pressure-Impulse (PI) diagrams. Due to limited research on the coupled system of AF and the PS, even fewer number of works exist on constructing PI diagrams for the coupled system [10–12]. These works included construction of PI diagrams for uniform AFs, and the non-linearity of the protected structures was commonly neglected [10, 11]. Consideration of different types of foams (e.g. non-uniform foams) does not exist, and validation of common assumptions in the literature regarding the foam efficiency for impulsive loads was not conducted as works on PI diagrams are very limited. Thus, a thorough investigation into the effectiveness of the foam for a large

load spectrum is notably absent. Key components in the dynamic response, such as the effect of the mass component and the effective load applied to the structure, remain largely unexplored.

In this work, to thoroughly investigate the foam performance and test its efficiency, a mathematical model using the SFT is adopted, considering foams with possible varying density. The model is utilized to construct PI diagrams aiming to investigate the foam behavior over a large load spectrum and test the common assumption regarding its efficiency. Moreover, a methodology regarding testing the foam efficiency is discussed.

# MODELING THE COUPLED RESPONSE USING THE SFT

## Model Formulation

The current section briefly presents a general model to simulate the coupled response of the AF and the PS, which then will be used for constructing the PI diagrams. The coupled response of the suggested system is composed of two components, the compaction of the foam and the response of the PS. In general, the structural response includes a continuous system with infinite Modes of Vibration (MoVs) and frequencies [13–16]. However, as the response is commonly governed by a single Modes of Vibration (MoV), the structural dynamic response can be modeled using an equivalent Single Degree of Freedom (SDOF) [15–17] as presented in Figure 1, which simulates a key displacement value along the structure (e.g. in a simply supported beam, the midspan is selected). The equivalent SDOF system is presented as following:

$$K_{LM}(y)M \cdot \ddot{y}(t) + R(y) = A \cdot F(t) \tag{1}$$

Where $M$ and $R$ are the total mass and resistance function of the PS, respectively, $y(t)$ and $\ddot{y}(t)$ are the displacement and acceleration of the PS at the location of the selected displacement, respectively, and $A$ is the loaded area. $F(t)$ is a general dynamic pressure applied on the PS. $K_{LM}(y)$ is the equivalent Load-Mass factor and can be found in literature for various boundary conditions and loading patterns [15, 16]. In the case of a structure protected by AF, $F(t)$ is the actual pressure transfer by the foam, which corresponds to the AF compaction.

The compaction of the AF is modeled by assigning correlated related Degrees of Freedom (DOFs) to the foam. The displacement of the cover plate of the foam is represented by $u(t)$, and the location of the shock front is represented by $s(t)$ (see Figure 1). The shock front separates the compacted and non-compacted regimes along the foam thickness, in which the non-compacted regime is attached to the PS. The compacted regime of the foam is subjected to the compaction stress of the foam ($\sigma_D$) and the non-compacted regime is subjected to the plateau stress of the AF ($\sigma_{pl}$) and transmits this stress to the PS. The mentioned stresses are

global mechanical foam features and are related to the foam local characteristics, i.e., the AF density $\rho(z)$. Ashby et al. [6] suggested the following relation between the varying foam density and its plateau stress and compaction strain:

$$\varepsilon_D(z) = \left(\alpha - \lambda \frac{\rho(z)}{\rho_s}\right) \tag{2}$$

$$\sigma_{pl}(z) = C_1 \sigma_{ys} \left(\frac{\rho(z)}{\rho_s}\right)^m \tag{3}$$

Where $\sigma_{pl}(z)$ and $\varepsilon_D(z)$ are the plateau stress and compaction strain along the AF, respectively, $\sigma_{ys}$ is the yield stress of aluminum, $\rho_s$ is the density of full solid scale aluminum, $z$ is the location along the AF thickness and $C_1$, m, $\alpha$ and $\beta$ are empirical parameters suggested in Ashby's book.

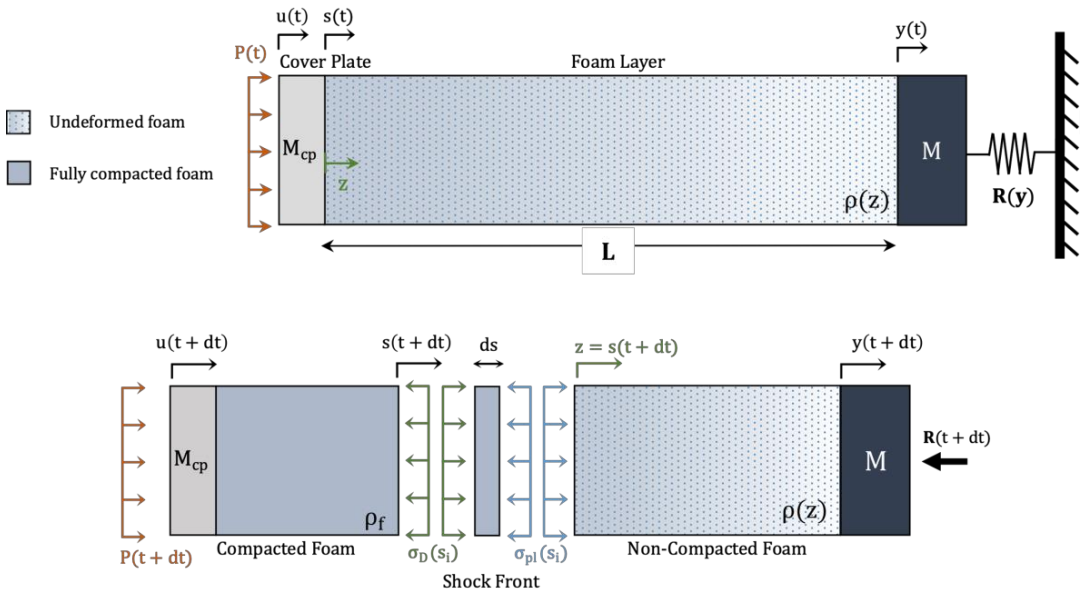


**Figure 1.** Propagation of a Shock Front along the Non-uniform AF thickness over Time.

The relation between the DOFs of the AF can be derived through mass conservation in the foam, in which the total mass of the foam being conserved during AF compaction. In other words, the mass of the compacted foam regime together with the mass of non-compacted regime must equal the mass of the foam before compaction. The previous derives the following relation:

$$u(t) = \frac{A\int_{s(t)-y(t)}^{L}\rho(z)dz - M_0}{A\rho_f} + s(t) \tag{4}$$

Where $M_0$ is the mass of the foam before compaction, $L$ is the foam thickness and $\rho_f$ is the foam density at full compaction of the foam.

The compaction stress $\sigma_D$ can be derived through momentum conservation on non-compacted foam facing the shock front before and after compaction. Overall, using Newton's second law on the compacted and noncompacted masses, and by incorporating Eqs. (1)-(4), the following Equations of Motion (EOMs), referred to as phase 1, are derived:

$$\begin{aligned}&\left[M_{cp} - A\left(\int_{s(t)-y(t)}^{L}\rho\,(z)dz\right) + M_0\right]\left[-\frac{[\ddot{s}(t)-\ddot{y}(t)]\rho(s(t)-y(t))}{\rho_f} - \frac{[\dot{s}(t)-\dot{y}(t)]^2\frac{\partial}{\partial t}[\rho(s(t)-y(t))]}{\rho_f} + \ddot{s}(t)\right] + \\ &\left[\sigma_{pl}(s(t)-y(t)) + [\dot{s}(t)-\dot{y}(t)]\rho(s(t)-y(t))\left[-\frac{(\dot{s}(t)-\dot{y}(t))\rho(s(t)-y(t))}{\rho_f} + \dot{s}(t)-\dot{y}(t)\right] - P(t)\right]A = 0\end{aligned} \tag{5}$$

$$\left[A\left(\int_{s(t)-y(t)}^{L}\rho\,(z)dz\right) + K_{LM}(y)M\right]\ddot{y}(t) + R(y) - C_1\left[\frac{\rho(s(t)-y(t))}{\rho_s}\right]^{\frac{3}{2}}\sigma_{ys}A = 0 \tag{6}$$

Where $M_{cp}$ is the mass of the AF cover plate and $P(t)$ is the blast pressure-time history. When the AF is no longer an active participant in absorbing energy during the dynamic response (see following text), phase 2 is initiated and is described as follows:

$$[M_{cp} + M_0 + K_{LM}(y)M]\ddot{y}(t) + R(y) - P(t)A = 0 \tag{7}$$

In phase 2, the AF is considered as an additional mass to the structure and is assumed to be fully attached to the PS. Using Newmark's $\beta$ method [18], the described EOMs and DOFs are transformed into time-stepping algebraic equations. To ensure the quality of the numerical simulation, stability, and convergence tests were performed, and an adequate time-step was chosen for the numerical solution. Experimental results were used to validate the numerical solution. This paper does not elaborate on the validation process and further details regarding the formulation of the model and validation can be found in work of Wattad [19] and in Wattad and Grisaro [20].

### Remarks regarding the model and numerical simulations

The following remarks highlight crucial details regarding the model assumptions and criteria for the numerical simulations -

1. According to the SFT, a shock front will only develop if the plateau stress $\sigma_{pl}$ at the loaded end is lower than the external load pressure at $t = 0$. This requirement implies that, at the coordinate $z = 0$ the plateau stress function must satisfy the condition for shock front development (i.e., $\sigma_{pl}(z = 0) < P(t = 0)$). Phase 2 is immediately initiated if the previous is not met with a system at rest conditions, and the foam compaction is not considered.

2. When foam compaction is considered and phase 1 is initiated, there are two potential outcomes for ending phase 1 and starting phase 2, each defined by specific initiation conditions to embody continuity criteria, as follows:

   - *Shock front stopped propagating* - in the case where the shock front velocity attained zero, the compaction wave stopped propagating (i.e., cases where the foam is not fully compacted), and the velocity and displacement of the PS at the end of phase 1 are the initial conditions for phase 2.

   - *Foam is fully compacted* - the AF is fully compacted, the strain at the end of the compacted regime reaches the full compaction strain of the foam which is defined as follows:

$$\varepsilon_{D_{tot}} = \frac{1}{L}\int_0^L \varepsilon_D(z)dz \tag{8}$$

   If the condition is met, the compacted foam is assumed to impact the PS with the velocity of the shock front, and momentum conservation must be applied to consider the combined velocity in which phase 2 is initiated.

3. Zero velocity of the PS is a stopping factor in cases where the peak displacement of the PS is the objective of the numerical analysis. The previous is applied only for phase 2, and is a primarily relevant for the formation of the PI diagrams as the objective is the structural peak displacement.

4. In the case where the AF applied in the simulations is considered to have uniform density distribution (i.e., $\rho(z) = constant$), the parameters which vary along the foam thickness become constant values as well, e.g. $\sigma_{pl}(z) = \sigma_{pl}$ and $\varepsilon_D(z) = \varepsilon_D$.

# PRESSURE IMPULSE DIAGRAMS

## Methodology

This section aims to shed light on the foam performance over a large load spectrum and examine its behavior when compared to appropriate cases. The primary methodology for comparison proposes that the application of AF to the structure fundamentally alters the mass component of the system, even before accounting for energy absorption capabilities of the foam. Thus, a suitable standard for evaluating the AF involves comparing the results of an AF protected structure to a structure with an additional mass equivalent to the AF mass but lacking

energy absorption capabilities. Furthermore,, a set of a structure and two types of sacrificial layers are utilized to construct PI diagrams. The layers include a layer with uniform density distribution and another with non-uniform density distribution that follows a linear density gradient along the thickness (linear density function) which leads to large density at the end facing the external load (specific characteristics available in [19]).
The diagrams associated with the foams were constructed based on the model developed in the previous section and by using a numerical search algorithm. Overall, PI diagrams for four scenarios were developed, with the objective of illustrating the previously suggested methodology: (1) an unprotected structure, (2) a structure with additional mass equal to the foam mass, (3) a structure protected by uniform AF, and (4) a structure protected by non-uniform AF with nonuniform density, where the density varies linearly within the foam thickness, such that the higher density facing the loaded area (scenarios 1, 2, 3 and 4, respectively). Note that the total mass of the AFs implemented in scenarios 3 and 4 equates to the mass of the additional mass in scenario (2).

## Selected Examples

Utilizing the aforementioned scheme, curves were constructed corresponding to different Levels of Performance (LOPs), each associated with a specific peak displacement of the structure. The results present two cases of LOPs ($LOP_1$ and $LOP_2$, i.e. two limit values of the peak displacement). The overall structure of these figures comprises a graph featuring curves associated with the four scenarios mentioned earlier. Additionally, two supplementary graphs are incorporated to visually represent the foam state at the end of the numerical simulations. These states include: (a) foam at full compaction, (b) shock front stopped propagating at a certain location along the foam thickness, and (c) no initiation of a shock front (i.e., the peak overpressure was smaller than the plateau stress of the first foam layer). Note that in order to construct each curve on the PI diagrams, a large number of structural analyses were performed using the developed model and numerical algorithm.

Figure 2(a) illustrates the curves constructed for a peak displacement associated with $LOP_1$. Generally, moving the PI curve upwards and to the right signifies a larger safe zone, indicating better damage mitigation. By analyzing the curves within the figure, the curve associated with scenario (1) (depicted in red) exhibits the smallest safe zone, positioned to the left among the four curves, as anticipated. Conversely, the curve associated with scenario (2) (depicted in green) displays an enlarged safe zone, supporting the fundamental assertion that altering the system mass only (with no energy absorption capabilities) can impact the response of the dynamic system and, in this case, enhance structural behavior, resulting in improved damage mitigation.
In contrast, the curve associated with scenario (3) (depicted in black) demonstrates superior performance compared to scenario (2), as it shifts further to the right. This suggests that the improvement might be attributed to energy absorption capabilities, i.e., by comparing scenarios (2) and (3) (and not by comparing scenarios 1 and 3 as done in many previous studies), an indirect evaluation of the energy absorption performed by the foam can be assumed. Notably, the deviation in the curve associated with scenario (2) becomes more pronounced with increasing pressure, particularly evident in the change in foam state depicted in Figure 2(b). It

is essential to highlight that the curves of the first three scenarios follow the general shape of traditional PI diagrams.

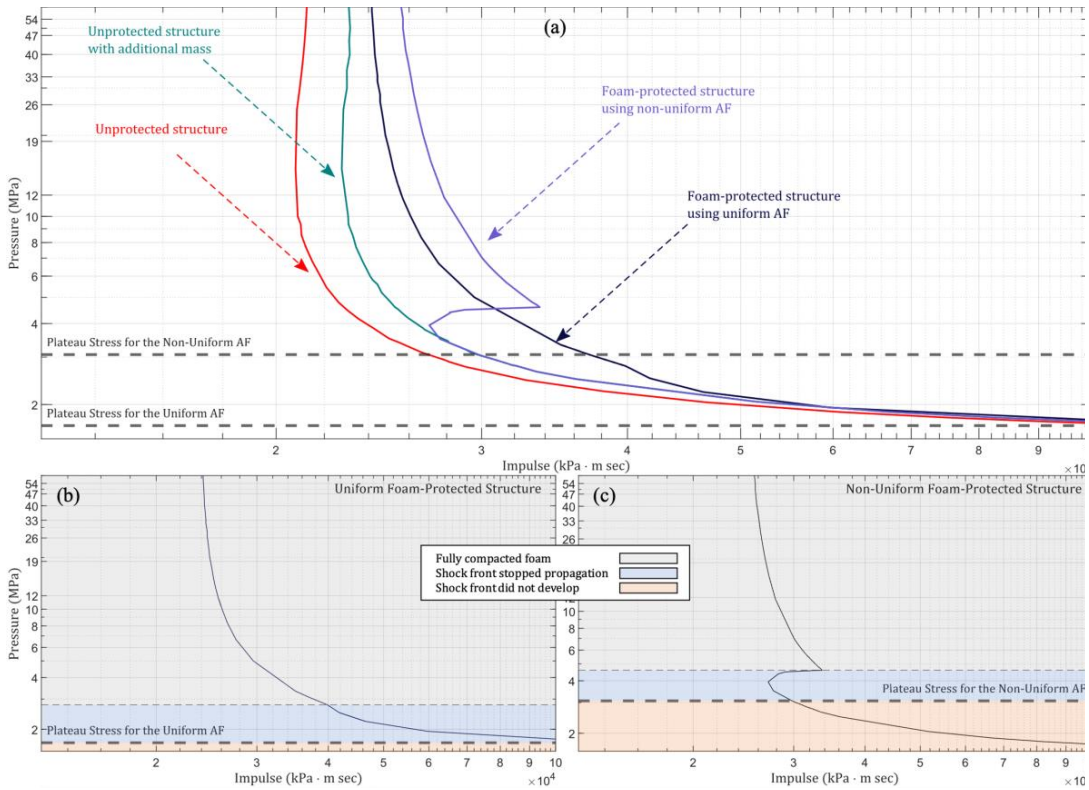


**Figure 2.** : PI Diagrams for $LOP_1$. (a) Comparison of PI Diagrams for the Four Suggested Scenarios. (b) State Division of Uniform AF Along its PI Curve. (c) State Division of Non-Uniform AF Along its PI Curve.

However, scenario (4) diverges from this pattern. The curve associated with scenario (4) (depicted in purple) initially aligns with the curve of scenario (2) in cases where the peak external pressure is smaller than the plateau stress associated with the density facing the load. In this case, the SFT suggests no development of a shock front, treating the foam as an additional mass (illustrated in Figure 2(c) in the foam state of no shock front initiation). In other words, the non-uniform foam initially performs similarly to the additional mass scenario, while a uniform AF can offer better damage mitigation within this range of loads. As the pressure surpasses the plateau stress, the curve associated with scenario (4) diverges from the curve of scenario (2), resulting in enhanced damage mitigation. However, a sharp shift across the impulse causes the curve of scenario (4) to intersect the curve associated with scenario (3), creating a larger safe zone with increasing pressure when compared with the other three scenarios. It is noteworthy that this shift, illustrated in Figure 2(c), occurs as the foam transitions between state (c) to (b) with the increase in pressure. This phenomenon warrants further investigation for a more comprehensive understanding. This behavior is detailed and examined in the next section by unraveling the time-histories of strategic points along the curve.

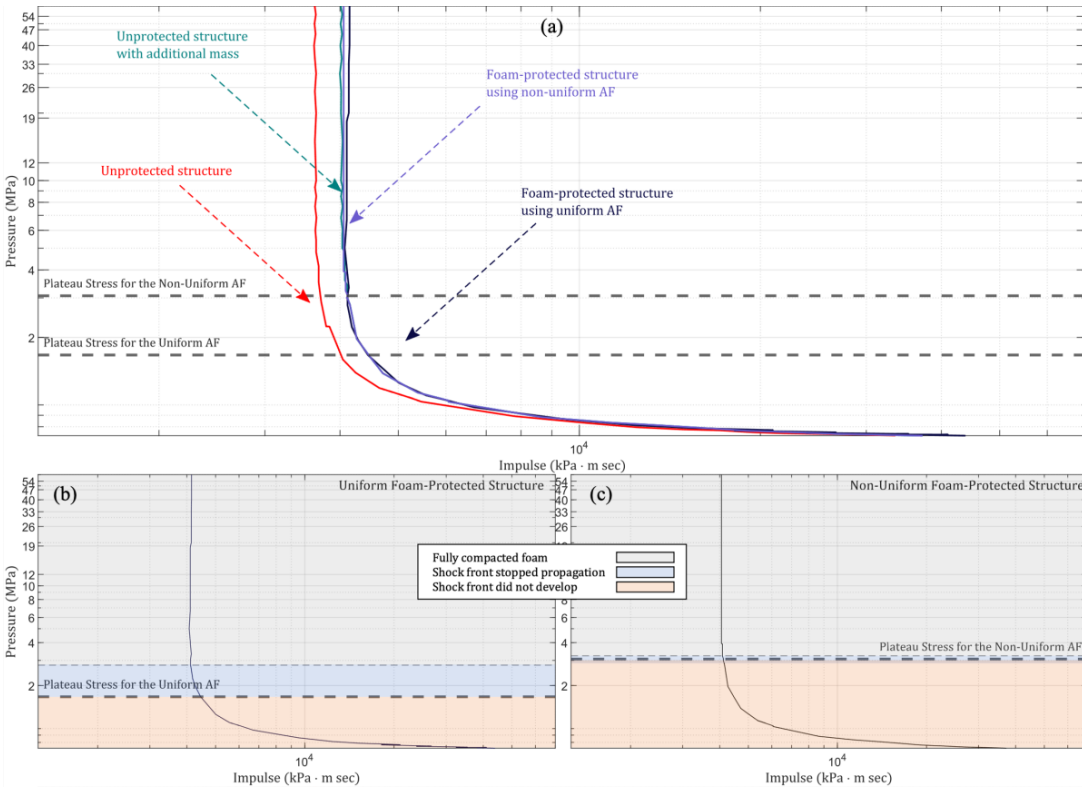


**Figure 3.** : PI Diagrams for $LOP_2$. (a) Comparison of PI Diagrams for the Four Suggested Scenarios.(b) State Division of Uniform AF Along its PI Curve. (c) State Division of Non-Uniform AF Along its PI Curve

Results of the scenario corresponding to $LOP_2$, presented in Figure 3(a), display a distinct behavior from the ones corresponding to $LOP_1$. Similar to the previous case, four curves are displayed, each associated with the previously mentioned scenarios. As observed previously, the curve associated with scenario (1) exhibits the smallest safe zone. However, in this instance, the curves associated with scenarios 2, 3, and 4 align and produce almost identical safe zones across all load combinations, as depicted in the figure. Notably, the curves associated with scenarios (3) and (4) manifest different foam states (ranging from states (a) to (c)), as displayed in Figures 3(b)-(c). Despite these varying states, no significant deviation from the other scenarios is observed. This suggests that the AF performance depends on its density distribution, mass, and the applied load and, therefore must be designed accordingly after understanding these main principles.

## Selected Examples

The PI diagrams for case no.1, characterized by non-uniform density distribution, revealed unprecedented behavior. This section delves into the sharp transition observed in the curve associated with scenario (4). The analysis involves examining two specific points on the PI diagram associated with the non-uniform foam. Each point represents a unique pressure-impulse combination, and their time-histories are explored in detail. The characteristics of these points are listed in Table 1.

**Table 1:** Load combinations of the selected points

| Point no. | Peak pressure [MPa] | Impulse [KPa · ms] | Load duration [ms] |
|---|---|---|---|
| Point no. 1 | 3.9 | 27,000 | 13.8* |
| Point no. 2 | 4.6 | 33,643 | 14.6* |

* The load duration is estimated based on the triangular load approximation.

Point no.1, marking the beginning of the observed shift, corresponds to a state where the shock front has stopped propagation without impacting the PS. In contrast, point no.2, located at the opposite end of the shift, represents a state of a fully compacted foam where the anticipated impact has occurred, leading to an expected increase in the velocity of the PS (refer to Figure 4 to visualize the points selected). This distinction underpins the main difference between the two cases. The structural displacement and velocity for both load combinations are depicted in Figure 5. A comparison between the velocity time-histories of the structure and the shock front is displayed in Figure 5. All figures feature three vertical lines to signify the load duration for point no.1 ($t_{01}$) at point no.2 ($t_{02}$), and the impact time associated with point no.2 ($t_{imp}$), respectively.

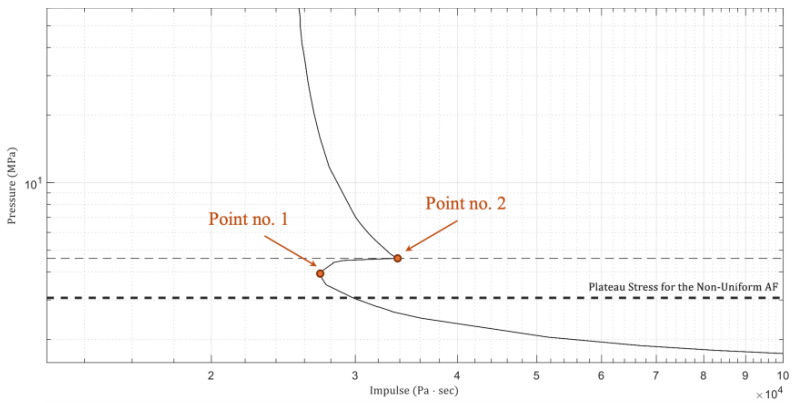


**Figure 4.** : Point Selection from the PI Diagram of $LOP_1$ used for the Detailed Time-History Investigation.

Figure 5(a) displays the displacement time histories for the selected points. Both curves derive a peak displacement of 14 [cm], aligning with the defined Level of Performance (LOP) for the PI diagram. The curve for Point 1 exhibits no inflection point throughout the duration, indicative of the foam not achieving full compaction under this load combination. As a result, the displacement time history of the structure remains unchanged (refer to Figure 5(a)). In contrast, the curve for point 2 presents an inflection point at $t_{imp} \approx 18.2\, ms$, marking the juncture at which the foam attains full compaction and impacts the structure at $t_{imp}$. This event triggers an increase in the velocity of the structure, as inferred from the derivative of the displacement time-history and leads to a noticeable alteration in the gradient of the displacement curve.

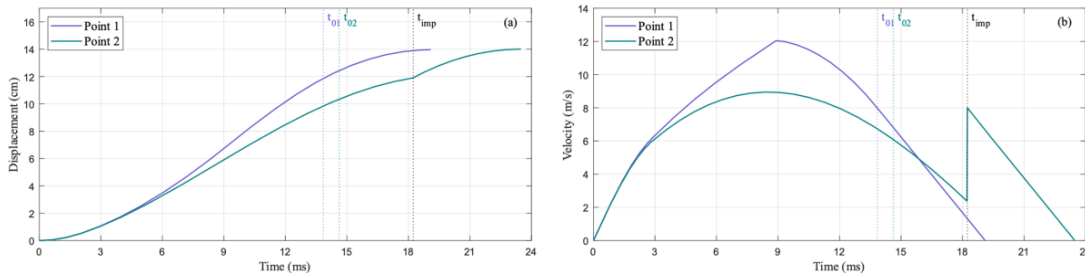


**Figure 5.** : Time histories of the detailed points. (a) Displacements time-histories (b) velocity time-histories.

The observed phenomenon is pictured in Figure 5(b), which illustrates the velocity time-histories. The curve for Point 2 shows a consistent behavior up to $t_{imp}$, the time when the foam achieves full compaction. Notably, at this juncture, the relative velocity of the shock front has not been reduced to zero, a detail that will be elaborated upon in subsequent discussions. This case, governed by the principle of momentum conservation, leads to a sharp increase in the structural velocity, thereby sustaining the structural response beyond this point. It is important to note that the impact time is closely aligned with the moment when the curve for point 1 indicates zero velocity (at the peak displacement $\approx$ 19 ms). In conditions excluding the impact, the peak displacement attributable to the load combination for Point 2 would have been lower, thus not manifesting within the PI diagram for this LOP. Additionally, the curve for point 1 undergoes a change in slope around $\approx$ 9 ms, attributed to modifications in the transmitted pressure behavior.

To further explain the above, the comparison between the shock front and structure velocity-time history is discussed in Figure 6. Within this figure, both subfigures (a and b) utilize dashed curves to represent the shock front velocity and solid curves for the structure velocity. Specifically, Figure 6(a) details the case for Point 1, where the shock front stopped propagating. The previous is graphically depicted as the shock front velocity decreasing until it aligns with the velocity of the structure, resulting in a relative velocity of zero. This convergence marks the transition to Phase 2 at approximately 9 ms. Subsequently, as the pressure transmitted to the structure diminishes, the velocity of the structure approaches zero, culminating in the peak displacement for this particular case.

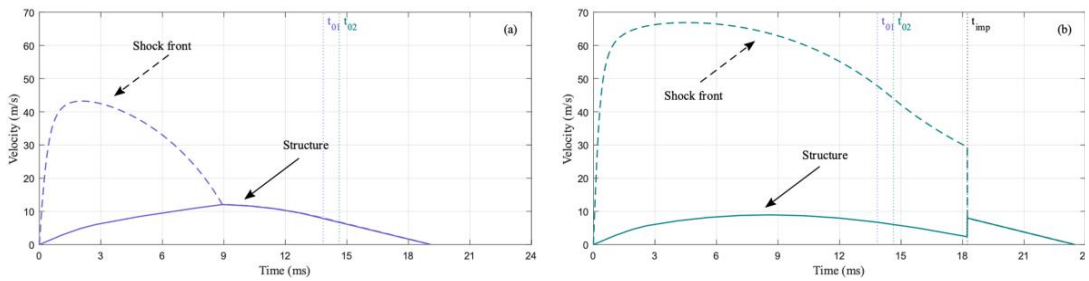


**Figure 6.** : Comparison of shock front and structure velocity time histories. (a) Velocity time histories of point no.1 (b) Velocity time histories of point no.2.

Figure 6(b) illustrates the case where the foam achieves full compaction. In this case, the shock front velocity remains above zero at the moment of impact, as indicated in the figure. At $t_{imp}$, the velocity of shock front velocity triggers an increase in the structure velocity, in accordance with the principle of momentum conservation. Following this impact, the velocity gradually declines during Phase 2, as the transmitted pressure to the structure drops to zero.

# SUMMARY AND CONCLUSIONS

To summarize, this study focuses on an exploration of the AF behavior with varying densities, encompassing both uniform and non-uniform density distributions, under a wide range of load combinations. A mathematical model was adopted to account for foam compaction, which is characterized by a general density distribution function along its thickness. This model facilitated the construction of PI diagrams aimed at dissecting AF behavior across a broad load spectrum. A methodology to assess AF performance was outlined through these diagrams. Notably, the curve representing non-uniform density AF exhibited unconventional behavior, necessitating a thorough analysis through detailed time histories of key load combinations. These investigations unveiled several interesting facets of foam performance, including the observation that the diagrams often adopt non-traditional shapes, and that the efficiency of foam performance varies, particularly when compared against relevant scenarios.

## ACKNOWLEDGMENTS

The support extended to Ola Wattad by the Edmond de Rothschild Foundation through the Ariane de Rothschild Women's Doctoral Program is warmly appreciated.

## REFERENCES

[1] Sivakumar Palanivelu et al. “Low velocity axial impact crushing performance of empty recyclable metal beverage cans”. In: *International Journal of Impact Engineering*, 38.7 (2011), pp. 622–636. issn: 0734-743X. doi: https://doi.org/10.1016/j.ijimpeng.2011.02.008.

[2] S. Chung Kim Yuen, G. Cunliffe, and M.C. du Plessis. “Blast response of cladding sandwich panels with tubular cores”. In: *International Journal of Impact Engineering,* 110 (2017). Special Issue in honor of Seventy Fifth Birthday of Professor N. K. Gupta, pp. 266–278. issn: 0734-743X. doi: https://doi.org/10.1016/j.ijimpeng.2017.04.016.

[3] J. Sousa-Martins et al. “Behaviour of sandwich structures with cork compound cores subjected to blast waves”. In: *Engineering Structures*, 46 (2013), pp. 140–146. issn: 0141-0296. doi: https://doi.org/10.1016/j.engstruct.2012.07.030.

[4] Jianjun Zhang, Guoxing Lu, and Zhong You. “Large deformation and energy absorption of additively manufactured auxetic materials and structures: A review”. In: *Composites Part B:*

*Engineering*, 201 (2020), p. 108340. issn: 1359-8368. doi: https://doi.org/10.1016/j.compositesb.2020.108340.

[5] AG Hanssen, L Enstock, and M Langseth. "Close-range blast loading of aluminium foam panels". In: *International journal of impact engineering*, 27.6 (2002), pp. 593–618. doi: https://doi.org/10.1016/S0734-743X(01)00155-5.

[6] Michael F Ashby et al. *Metal foams: a design guide.* Elsevier, 2000.

[7] D.Karagiozova, G.S.Langdon,and G.N. Nurick. "Propagation of compaction waves in metal foams exhibiting strain hardening". In: *International Journal of Solids and Structures*, 49.19 (2012), pp. 2763–2777. issn: 0020-7683. doi: https://doi.org/

10.1016/j.ijsolstr.2012.03.012.

[8] P.J. Tan et al. "Dynamic compressive strength properties of aluminium foams. Part II—'shock' theory and comparison with experimental data and numerical models". In: *Journal of the Mechanics and Physics of Solids,* 53.10 (2005), pp. 2206–2230. issn: 0022-5096. doi: https://doi.org/10.1016/j.jmps.2005.05.003.

[9] Hongyuan Zhou et al. "Energy absorption of graded foam subjected to blast: A theoretical approach". In: Materials & Design

84 (2015), pp. 351–358. doi: https://doi.org/10.1016/j.matdes.2015.06.124.

[10] ZQ Ye and GW Ma. "Effects of foam claddings for structure protection against blast loads". In: *Journal of Engineering Mechanics,* 133.1 (2007), pp. 41–47. doi: https://doi.org/10.1061/(ASCE)0733-9399(2007)133:1(41).

[11] G.W. Ma and Z.Q. Ye. "Analysis of foam claddings for blast alleviation". In: *International Journal of Impact Engineering,* 34 (2005), pp. 60–70. issn: 0734-743X. doi: https://doi.org/10.1016/j.ijimpeng.2005.10.005.

[12] Ye Xia, Chengqing Wu, and Zhong-Xian Li. "Optimized design of foam cladding for protection of reinforced concrete members under blast loading". In: *Journal of Structural Engineering*, 141.9 (2015), p. 06014010. doi: https://doi.org/10.1061/(ASCE)ST.1943-541X.0001190.

[13] Jagmohan Humar. *Dynamics of Structures*. CRC press, 2012.

[14] A.K. Chopra. *Dynamics of Structures*. Pearson Education, 2007. isbn: 9788131713297.

[15] J.M. Biggs. *Introduction to Structural Dynamics*. McGraw-Hill, 1964. isbn: 9780070052550.

[16] T. Krauthammer. *Modern Protective Structures*. Boca Raton, 2008. isbn: 9780429118890. doi: https://doi.org/10.1201/9781420015423.

[17] USACE. Unified Facilities Criteria (UFC)- *Structures To Resist The Effects Of Accidental Explosions*. UFC, 2008.

[18] Nathan M Newmark. "A method of computation for structural dynamics". In*: Journal of the engineering mechanics division*, 85.3 (1959), pp. 67–94.

[19] Ola Wattad. "*Dynamic behavior of structures with energy absorption protection layer under blast loads*, M.Sc. Thesis, [Supervision: Hezi Grisaro]". In: Technion - Israel Institute of Technology. (2023), p. doi: https://technion.primo.exlibrisgroup.com/permalink/972TEC_INST/q1jq5o/alma9926907874103971.

[20] Ola Wattad and Hezi Grisaro. "*Dynamic Behavior of Structures with Energy Absorption Protection Layer under Blast Loads*". In: (May 2023). Ed. by James S. Davidson and Catherine S. Stephens, pp. 250–258.

# INFLUENCE OF GROUTING DEFECTS ON THE DYNAMIC TENSILE BEHAVIOUR OF GROUTING SLEEVE CONNECTIONS

*An He[1], Dun-Cong Zheng[2], Qing-Jun Chen[3], and Jia-Bin Ye[4]*

[1] PhD., South China University of Technology, hean@scut.edu.cn.

[2] Mr., South China University of Technology, ctdczheng@mail.scut.edu.cn.

[3] PhD., South China University of Technology, qjchen@scut.edu.cn.

[4] PhD., South China University of Technology, jb_ye@foxmail.com.

**Corresponding Author: Jia-Bin Ye, PhD.**

381 Wushan Road, Tianhe District, Guangzhou, Guangdong, China, 510641

**Email:** jb_ye@foxmail.com

## ABSTRACT

The grouting sleeve is commonly used for the reinforcement connection between precast reinforced concrete components. During construction, the compactness of the grout in the sleeve may have defects, affecting the mechanical performance of the connection. The behaviour of the grouting sleeve connection with grouting defects subjected to dynamic tensile loads was numerically investigated in this paper. Finite element (FE) models of the grouting sleeve connection incorporating various types of defects were developed and validated against the test results. A comprehensive parametric study was conducted to evaluate the effects of the steel rebar diameter, the defect type, the rebar anchorage length, and the tensile rate on the bearing capacity and the failure mode of the grouting sleeve connection. The results indicate that the yield load and ultimate load increase with the increase of steel rebar diameter. Defects located in the middle of the connection exhibited a more significant detrimental effect on performance compared to those at the ends. Furthermore, an increase in defect length resulted in decreasing ultimate loads and a shift in failure mode from steel bar fracture to pull-out. This pull-out failure mode was more likely to occur at a higher tensile rate. Considering the influence of the defect type and the tensile rate, a formula was proposed to predict the bond strength of the grouting sleeves. The predicted bond strengths demonstrated good agreement with both the experimental and FE model results.

***Keywords:*** *Grouting Sleeve, Finite Element Model, Defects, Dynamic Behaviour, Bond Strength.*

# 1. INTRODUCTION

The grouting sleeve connection is widely used in the rebar connection of prefabricated structures because of its broad applicability, reliable performance and easy installation [1]. However, the challenge of controlling grouting quality during construction often results in defects such as voids in the sleeve, thereby directly diminishing the effective anchorage length of the reinforcement [2][3]. The defects may weaken the strength of the grouting sleeve connections, potentially leading to premature failure of the connections and the prefabricated structures [4][5].

Prefabricated bridge piers with grouting sleeve connections are susceptible to impact loads such as explosions and vehicle collisions during service. The impact loads generally result in substantial peak force with transient action. Thus, the mechanism of the precast structures under impact loads is significantly different from that under static loads [6][7]. This induces a dynamic effect in the reinforcement and grout sleeve connections, which notably impacts the strength of these connections [8][9]. However, investigations into the dynamic tensile behaviour of the grout sleeves are currently limited, particularly with regard to the inclusion of grouting defects in the connections.

This paper investigates the dynamic tensile behaviour of the grouting sleeve connections with the grouting defects considered. Finite element (FE) models of the grouting sleeve connections are first established and validated against the test results. Parametric studies are then carried out to investigate the effects of the defect type, the reinforcement anchorage length and the tensile rate on the bearing capacity and failure mode of grouting sleeve connections. Finally, a formula for calculating the bond strength of grouting sleeves with grouting defects is proposed.

# 2. FINITE ELEMENT MODELLING

## 2.1. Previous experimental investigation

Sixteen grouting sleeve connection specimens considering the end and middle defects have been fabricated and utilised for tensile tests [10]. The detailing of the specimens is depicted in **Figure 1**, which includes the connected rebars and a grouting sleeve. According to JGJ 355-2015 [11], the anchorage length in the sleeve should be eight times the diameter of the rebar (8$d$). In the experiments, defect lengths of 2.5$d$, 3$d$, 3.5$d$, and 4$d$ were respectively set at the middle and the end of the grouting segment, corresponding to anchor lengths of 5.5$d$, 5$d$, 4.5$d$, and 4$d$. The defects were introduced by covering the rebars with plastic film before casting the grout into the sleeve. The geometric dimensions of the grouting sleeves are listed in **Table 1**.

Grade HRB400 rebars and the carbon steel sleeve with a nominal strength of 600 MPa were used to fabricate the connection. The yield strength and the ultimate strength of the rebars were derived by tensile tests and were 410.7 MPa and 610.2 MPa, respectively. High-strength grout with a nominal compressive strength of 80 MPa was adopted to fill the gap between the rebar and the sleeve. Tensile tests were conducted on the grouting sleeve connections using a universal testing machine. Two levels of loading rates (i.e., 5 mm/min and 1000 mm/min)

were considered in the experiments. During the tests, an extensometer was arranged between the rebars and the sleeve to measure the slip deformation. More details relating to the test results can be found in the published literature [10].

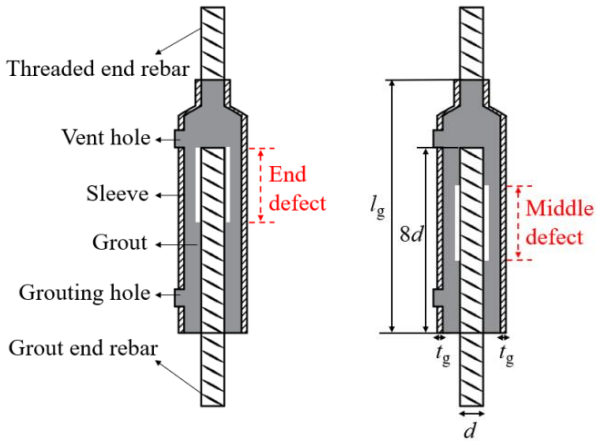


(a) End defect (b) Middle defect

**Figure 1.** Detailing of the grouting sleeve connection specimens.

**Table 1.** Geometric dimensions of the grouting sleeves

| Type of grouting sleeve | Diameter of rebar ($d$) | Length of grouting sleeve ($l_g$) | Thickness of grouting sleeve ($t_g$) |
|---|---|---|---|
| G12 | 12 mm | 135 mm | 4 mm |
| G16 | 16 mm | 175 mm | 4 mm |

## 2.2. Details of FE model

The finite element software ABAQUS was used to simulate the dynamic tensile behaviour of the grouting sleeve connections, as shown in **Figure 2**. The concrete plastic damage model was used to simulate the grout material of the specimens. The elastic modulus of the grout was set equal to $3.65\times10^4$ MPa, and the Poisson ratio was 0.2. The elastic-plastic model was adopted for the rebars with elastic modulus and the Poisson's ratio set equal to $2\times10^5$ MPa and 0.3, respectively. The experimental results have indicated that the sleeve behaved elastically during the test. Therefore, the ideal elastic model was used for the sleeve, with the elastic modulus and Poisson's ratio consistent with that of the rebar.

The cohesion model in ABAQUS was adopted to simulate the bond-slip behaviour between the rebar and the grout. A “tie” contact approach was utilised between the grout and the sleeve since any bond slip between them was neglected, as observed in the experiments. The components were partitioned using a structured mesh, and C3D8R elements were utilised for each component unit. The mesh size of each component was set equal to 5 mm after trial calculation. The grout defect was simulated by deleting the solid elements of the grout adjacent to the rebar at a specific length, as shown in **Figure 2**.

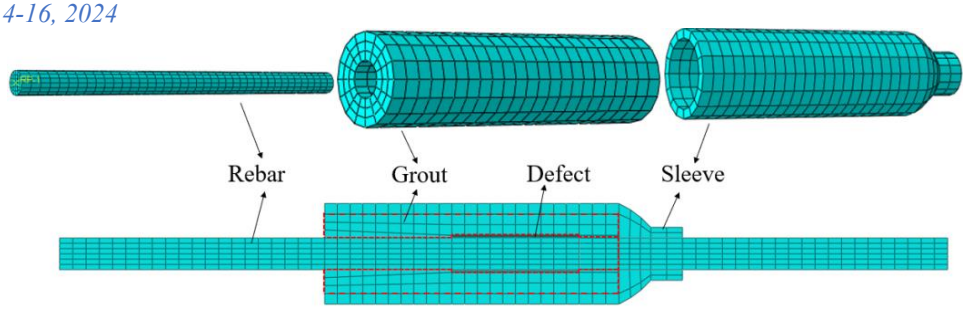


**Figure 2.** Finite element model.

## 2.3. Validation of FE model

The test and simulated load–slip curves for two typical specimens with the end defect length equal to 2.5 times the diameter are shown in **Figure 3**, in which the test curves were found to be well replicated by the ones derived from the FE models. The test ultimate loads of the specimens G12-E-2.5d-5 and G12-E-2.5d-1000 are 68.93 kN and 75.19 kN, respectively, and those obtained by the FE models are 69.32 kN and 76.44 kN, respectively, with the errors less than 5%. Moreover, the simulation results of these two specimens indicate steel bar fracture failure and steel bar pull-out failure, respectively, which is also consistent with the test results. Therefore, it can be concluded that the established model is capable of simulating both static and dynamic tensile behaviour of the grouting sleeve connections and is deemed to be validated.

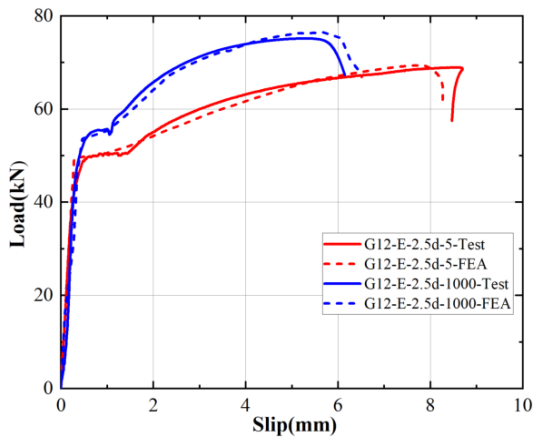


**Figure 3.** Comparisons of load–slip curves between test and FE results.

## 2.4. Parametric analysis of FE model

Based on the validated FE model, parametric studies were carried out to study the influence of the rebar diameter (i.e., 12 mm and 16 mm), the defect type (i.e., end defect and middle defect), the defect length (2.5*d*, 3*d*, 3.5*d* and 4*d*), and the tensile velocity (5 mm/min, 100 mm/min and 1000 mm/min) on the tensile behaviour of the grouting sleeve connections.

**Table 2** summarizes the ultimate loads and the failure modes of the FE models. The label of each FE model starts with the rebar diameter of the connection, followed by the defect type 'E' (indicating end defect) or 'M' (indicating middle defect) and the defect length, and ends with the loading velocity.

**Table 2.** Results of all specimens.

| Specimen | Ultimate load (kN) | Failure mode | $\tau$ (MPa) | Specimen | Ultimate load (kN) | Failure mode | $\tau$ (MPa) |
|---|---|---|---|---|---|---|---|
| G12-E-2.5d-5 | 69.32 | Fracture | 27.88 | G12-M-2.5d-5 | 67.07 | Pull-out | 26.97 |
| G12-E-3d-5 | 62.95 | Pull-out | 27.84 | G12-M-3d-5 | 61.10 | Pull-out | 27.03 |
| G12-E-3.5d-5 | 57.75 | Pull-out | 28.38 | G12-M-3.5d-5 | 55.06 | Pull-out | 27.1 |
| G12-E-4d-5 | 54.81 | Pull-out | 30.31 | G12-M-4d-5 | 52.37 | Pull-out | 28.96 |
| G16-E-2.5d-5 | 121.99 | Fracture | 27.59 | G16-M-2.5d-5 | 114.04 | Pull-out | 25.79 |
| G16-E-3d-5 | 113.77 | Pull-out | 28.31 | G16-M-3d-5 | 109.33 | Pull-out | 27.20 |
| G16-E-3.5d-5 | 105.90 | Pull-out | 29.28 | G16-M-3.5d-5 | 100.72 | Pull-out | 27.84 |
| G16-E-4d-5 | 94.80 | Pull-out | 29.48 | G16-M-4d-5 | 92.53 | Pull-out | 28.78 |
| G12-E-2.5d-100 | 71.69 | Pull-out | 28.83 | G12-M-2.5d-100 | 67.26 | Pull-out | 27.05 |
| G12-E-3d-100 | 67.92 | Pull-out | 30.04 | G12-M-3d-100 | 63.00 | Pull-out | 27.87 |
| G12-E-3.5d-100 | 61.02 | Pull-out | 29.99 | G12-M-3.5d-100 | 57.36 | Pull-out | 28.19 |
| G12-E-4d-100 | 56.62 | Pull-out | 31.31 | G12-M-4d-100 | 54.51 | Pull-out | 30.14 |
| G16-E-2.5d-100 | 127.34 | Pull-out | 28.80 | G16-M-2.5d-100 | 125.75 | Pull-out | 28.44 |
| G16-E-3d-100 | 115.99 | Pull-out | 28.86 | G16-M-3d-100 | 118.13 | Pull-out | 29.39 |
| G16-E-3.5d-100 | 111.03 | Pull-out | 30.69 | G16-M-3.5d-100 | 106.94 | Pull-out | 29.56 |
| G16-E-4d-100 | 100.54 | Pull-out | 31.27 | G16-M-4d-100 | 96.12 | Pull-out | 29.89 |
| G12-E-2.5d-1000 | 76.44 | Pull-out | 30.74 | G12-M-2.5d-1000 | 70.88 | Pull-out | 28.50 |
| G12-E-3d-1000 | 68.95 | Pull-out | 30.50 | G12-M-3d-1000 | 67.44 | Pull-out | 29.83 |
| G12-E-3.5d-1000 | 64.56 | Pull-out | 31.73 | G12-M-3.5d-1000 | 62.82 | Pull-out | 30.87 |
| G12-E-4d-1000 | 59.76 | Pull-out | 33.04 | G12-M-4d-1000 | 58.60 | Pull-out | 32.40 |
| G16-E-2.5d-1000 | 133.21 | Pull-out | 30.13 | G16-M-2.5d-1000 | 125.97 | Pull-out | 28.49 |
| G16-E-3d-1000 | 123.29 | Pull-out | 30.68 | G16-M-3d-1000 | 116.31 | Pull-out | 28.94 |
| G16-E-3.5d-1000 | 114.82 | Pull-out | 31.74 | G16-M-3.5d-1000 | 109.24 | Pull-out | 30.20 |
| G16-E-4d-1000 | 103.75 | Pull-out | 32.27 | G16-M-4d-1000 | 100.71 | Pull-out | 31.32 |

The obtained load–slip curves from parametric studies are shown in **Figure 4**. It can be found that the yield loads and ultimate loads of the connections with a rebar diameter of 16 mm are significantly higher than those with a rebar diameter of 12 mm. The connections experience reinforcement fracture when the end defect length is not greater than 2.5$d$ under static loads with a loading speed of 5 mm/min, while reinforcement pull-out failure occurs when the end defect length exceeds 2.5$d$. Moreover, the ultimate load of each specimen decreases with increasing defect length, indicating that the presence of defects has an adverse effect on the ultimate loads of the grouting sleeve connections, eventually leading to a transition in failure mode towards the pull-out of the reinforcement.

Compared to the end defect, the pull-out failure mode was found on all the connections with middle defects. Additionally, the ultimate loads of the connections with middle defects are lower than those of their counterparts with end defects, indicating that middle defects have a more detrimental impact on the tensile resistances of the grouting sleeve connections.

With the increase in loading rate, the connections are more prone to failure through reinforcement pull-out. For example, specimens G12-E-2.5d-5 and G16-E-2.5d-5, subjected

to a loading rate of 5 mm/min, ultimately failed due to reinforcement fracture. Conversely, their counterparts tested at 100 mm/min and 1000 mm/min exhibited failure through rebar pull-out. This phenomenon can be attributed to the concentrated tensile deformation of the reinforcement within the grout near the sleeve opening under dynamic tension. Consequently, the grout in this region experiences more severe damage, diminishing the effective anchorage length of the reinforcement. This shift in failure mode, from reinforcement fracture under static tension to pull-out under dynamic tension. Additionally, both the yield loads and ultimate loads of the connections increased with higher loading rates, attributed to the strain rate effect under dynamic loading.

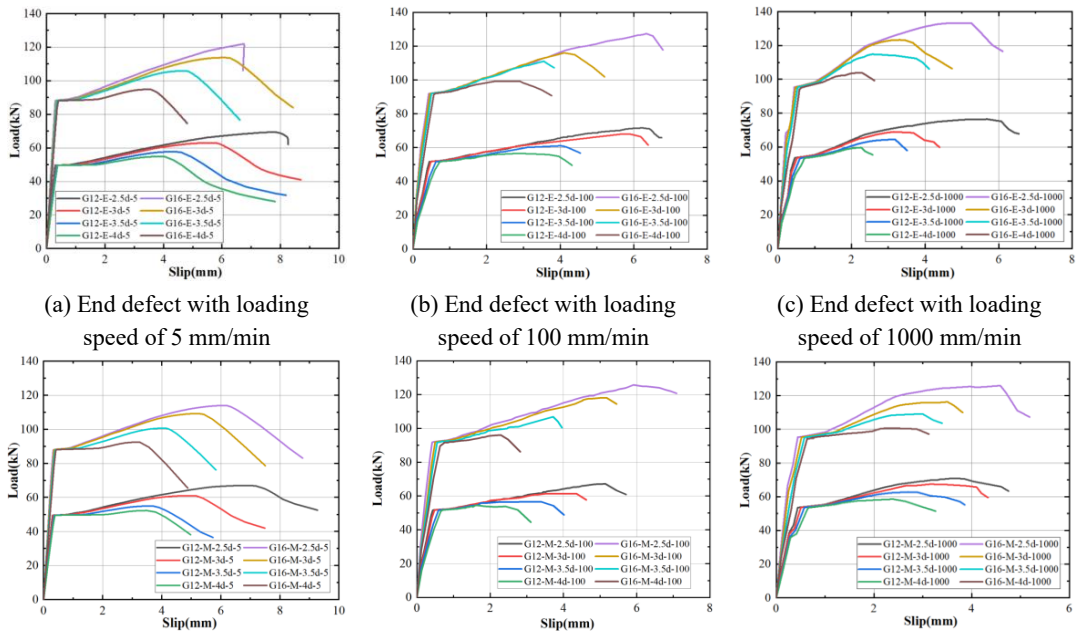


(a) End defect with loading speed of 5 mm/min

(b) End defect with loading speed of 100 mm/min

(c) End defect with loading speed of 1000 mm/min

(d) Middle defect with loading speed of 5 mm/min

(e) Middle defect with loading speed of 100 mm/min

(f) Middle defect with loading speed of 1000 mm/min

**Figure 4.** Load–slip curves of all specimens.

Assuming that the bond strength is evenly distributed along the length of the steel bar, the bond strength of the grout $\tau$ can be calculated by Eq. (1), where $P$ is the ultimate load, $d$ is the diameter of rebar, and $l$ is the effective anchor length.

$$\tau = P/(\pi\, d\, l) \tag{1}$$

The bond strength of each grouting sleeve connection was determined by Eq. (1), as listed in **Table 2** and displayed in **Figure 5**. It was found that the bond strengths of the connections range from 25.79 MPa to 33.04 MPa. With the increase in defect length, a clear rising trend of the bond strength was observed in **Figure 5**. Conversely, a slight decrease in bond strength was observed with increasing diameter of the rebar. Additionally, the bond strength of

grouting sleeve connections exhibited an increase when subjected to higher tensile rates due to the strain rate effect of the grout material.

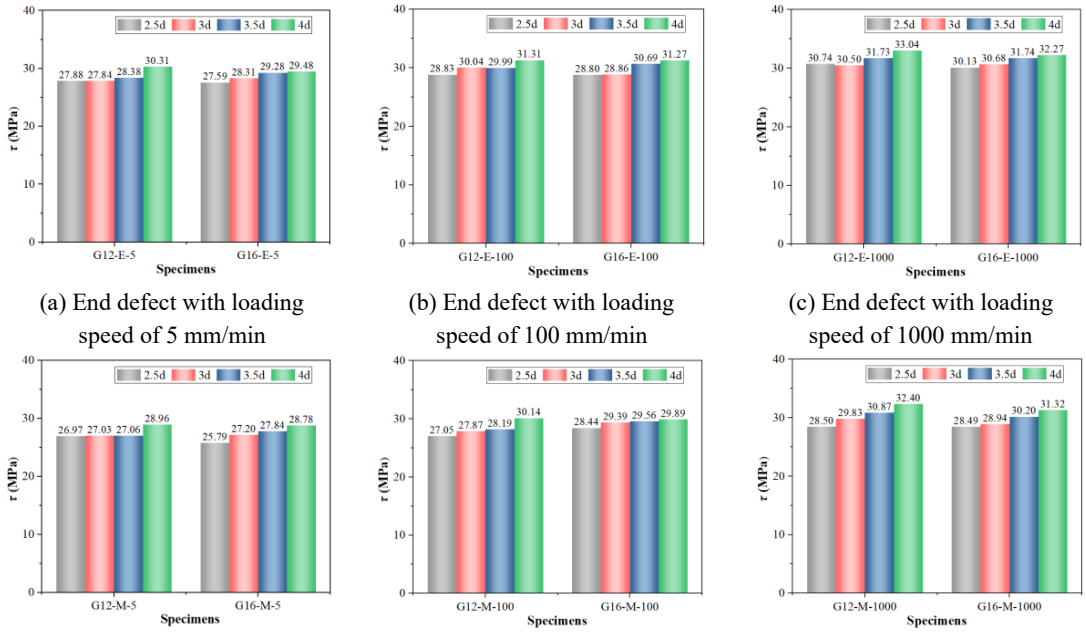


(a) End defect with loading speed of 5 mm/min

(b) End defect with loading speed of 100 mm/min

(c) End defect with loading speed of 1000 mm/min

(d) Middle defect with loading speed of 5 mm/min

(e) Middle defect with loading speed of 100 mm/min

(f) Middle defect with loading speed of 1000 mm/min

**Figure 5.** The bond strengths of the grouting sleeve connections.

## 3. CALCULATION OF BOND STRENGTH

When subjected to tensile loads, the bond strength of the grouting sleeve connection is primarily determined by the mechanical interlocking forces between the reinforcement and grout, as depicted in **Figure 6**. If the mechanical interlocking force between the rebar and grout exceeds the tensile strength of the reinforcement, the connection undergoes tensile failure of the rebar. Otherwise, pull-out failure of steel rebar occurs.

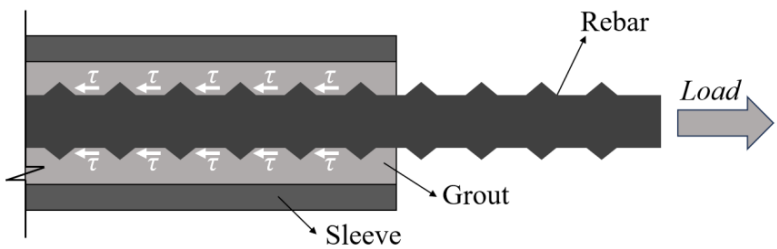


**Figure 6.** Force transmission model of the grouting sleeve connection.

The factors affecting the bond strength (i.e., mechanical interlocking force) between rebar and grout under dynamic tensile include the circumferential constraint force of the sleeve ($u_n$), the rebar anchorage length ($l$), the compressive strength of the grout material ($f_g$) and the

strain rate. The formula proposed by Untrauer and Henry [12] for predicting the bond strength of rebars was adopted, as given by Eq. (2). The circumferential constraint force of the sleeve can be determined by Eqs. (3)–(5) [13], in which $T_t$ and $f_t$ are the tensile force and the transverse tensile stress in the sleeve, $\varepsilon_t$ and $E_g$ are strain and the modulus of elasticity of the grouted sleeves, respectively. The transverse tensile strain of the sleeve was set equal to 200με, based on the experimental observation from tensile tests [10]. This leads to the circumferential constraint force for the G12 and G16 type sleeves equal to 10.67 MPa and 8.89 MPa, respectively.

$$\tau_0 = (1.49+0.45\sqrt{u_n}\sqrt{f_g}) \tag{2}$$

$$u_n = 2T_t/(d\ l) \tag{3}$$

$$T_t = f_t\ t_g\ l \tag{4}$$

$$f_t = \varepsilon_t\ E_g \tag{5}$$

The effect of strain rate on bond strength is considered through the enhancement of the grout compressive strength. According to the general empirical formula, the increase of compressive strength of grout can be regressed linearly related to the logarithm of strain rate, as given by Eq. (6), where $f_{g,d}$ and $f_{g,s}$ are respectively the compressive strength of grout under dynamic and quasi-static conditions, $\dot{\varepsilon}_d$ is the strain rate under dynamic condition, and $\dot{\varepsilon}_s$ is the strain rate under quasi-static conditions and is equal to $10^{-5}s^{-1}$.

$$\frac{f_{g,d}}{f_{g,s}} = 1.0+0.05\lg\left(\frac{\dot{\varepsilon}_d}{\dot{\varepsilon}_s}\right) \tag{6}$$

To consider the effect of the grouting defect on the bond strength of the connection, an influence coefficient $\lambda$ was introduced in Eq. (2), as given by Eq. (7). The grouting defect diminishes the effective anchorage length of the rebar and thus reduces the bond strength, which is reflected by the ratio of the effective anchorage length to the rebar diameter ($l/d$). The impact of the defect type on the bond strength is reflected through the coefficient $\alpha$, with the values of 0.068 and 0.075 assigned to end defects and middle defects, respectively. The final formulation for predicting the bond strength of the grouting sleeve connection with grouting defect is given by Eq. (8).

$$\tau_c = \tau_0 \cdot \lambda = \tau_0\left(1.36-\alpha\frac{l}{d}\right) \tag{7}$$

$$\tau_c = (1.49+0.45\sqrt{u_n})\sqrt{f_{g,d}}\left(1.36-\alpha\frac{l}{d}\right) \tag{8}$$

The bond strengths of the grouting sleeve connections were determined by Eq. (8) and compared against the FE results, as shown in **Figure 7**. It can be seen that the proposed formula is applicable for calculating the bond strengths of grouting sleeve connections under dynamic tension considering defects.

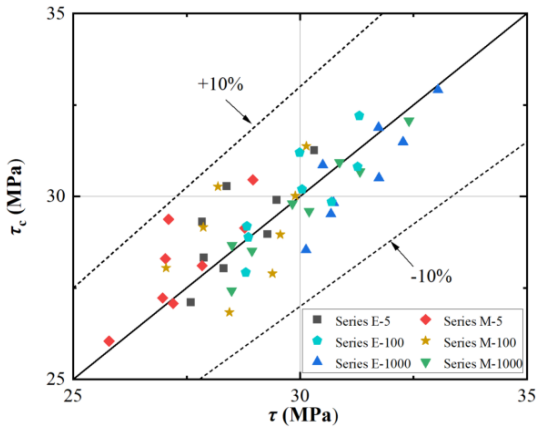


**Figure 7.** Comparisons between bond strength obtained by the formula and FE model

## 4. CONCLUSIONS

(1) The behaviour of the grouting sleeve connection considering grouting defects was numerically studied in this paper. The failure mode and the bearing capacity of the proposed FE models were consistent with the test results.

(2) The parametric studies reveal that the yield load and ultimate load increase with the increase of steel bar diameter. Defects located in the middle of the connection exhibited a more detrimental impact on performance compared to those at the ends. Furthermore, an increase in defect length resulted in decreasing ultimate loads and a shift in failure mode from steel bar fracture to pull-out. This pull-out failure mode was more likely to occur at a higher tensile rate.

(3) Taking into account the influence of defect types and tensile rate, a formula was proposed for calculating the bond strength of grouting sleeves. The predicted bond strengths exhibited good agreement with both experimental and FE model results.

## ACKNOWLEDGMENTS

Funding for this research project was provided by National Natural Science Foundation of China (No. 52108143), GuangDong Basic and Applied Basic Research Foundation (2021A1515110109), Science and Technology Program of Guangzhou, China (202201010590), Youth Talent Support Programme of Guangdong Provincial Association for Science and Technology (SKXRC202307), Science and Technology Planning Project of

Guangzhou Municipal Construction ([2022]-KJ013; [2022]-KJ032; [2023]-KJ052). The support for the research acknowledged with thanks.

## REFERENCES

[1] Li, X., Xiao, S., Gao, R., Harries, K. A., Wang, Z., Xu, Q. (2021). Effects of grout sleeve defects and their repair on the seismic performance of precast concrete frame structures. *Engineering Structures*, 242, 112619.

[2] Xiao, S., Wang, Z., Li, X., Harries, K. A., Xu, Q., Gao, R. (2021). Study of effects of sleeve grouting defects on the seismic performance of precast concrete shear walls. *Engineering Structures*, 236, 111833.

[3] Cao, D., Pan, Z., Zhang, Z., Zeng, B. (2023). Experimental and numerical study on detection of sleeve grouting defect with impact-echo method. *Structures*, 52, 632-650.

[4] Zhang, W., Wang, J., Zhang, J., Cao, Y., Qin, P., Yi, W. (2020). Experimental study on post-fire performance of half grouted sleeve connection with construction defect. *Construction and Building Materials*, 244, 118165.

[5] Guo, T., Yang, J., Wang, W., Li, C. (2022). Experimental investigation on connection performance of fully-grouted sleeve connectors with various grouting defects. *Construction and Building Materials*, 327, 126981.

[6] Tran, D. T., Pham, T. M., Hao, H. (2024). Experimental and analytical investigations of prefabricated segmental concrete beams post-tensioned with unbonded steel/FRP tendons subjected to impact loading. *International Journal of Impact Engineering*, 186, 104868.

[7] Li, R. W., Zheng, X. X., Wu, H. (2023). Influence of stirrup ratio on vehicular impact resistance of double-column RC bridge piers. *Engineering Structures*, 289, 116309.

[8] Li, H., Chen, W., Huang, Z., Hao, H., Ngo, T. T., Pham, T. M., et al. (2022). Dynamic response of monolithic and precast concrete joint with wet connections under impact loads. *Engineering Structures, 250, 113434.*

[9] Zhao, W., Feng, H., Ye, J., Qian, J. (2022). Performance of precast concrete bridge piers with grouted sleeve connections against vehicle impact. *Structures, 44*, 1874-1885.

[10] Wu Z., He A., Ye J. (2023). Influence of grouting defects on dynamic connection performance of steel sleeve. *South China Journal of Seismology, 43(02)*, 143-150.

[11] JGJ 355-2015. (2015). Technical specification of grout sleeve splicing for reinforcements. *Beijing: China Architecture & Building Press*.

[12] Untrauer, R. E., & Henry, R. L. (1965). Influence of normal pressure on bond strength. *ACI Structural Journal*, 65, 577-585.

[13] Ling, J. H., Rahman, A. B. A., Ibrahim, I. S., Hamid, Z. A. (2016). Tensile capacity of grouted splice sleeves. *Engineering Structures*, 111, 285-296.

# PEAK DISPLACEMENT OF LARGE STRUCTURES SUBJECTED TO AIR EXPLOSIONS

*Tusshar Goel[1], and Shashank[2]*

[1] Research Scholar, Indian Institute of Technology (IIT) Mandi, India, d21070@students.iitmandi.ac.in.

[2] Assistant Professor, Indian Institute of Technology (IIT) Mandi, India, shashank@iitmandi.ac.in.

**Corresponding Author: Shashank Pathak, PhD, IIT Mandi.**

School of Civil and Environmental Engineering, IIT Mandi, H.P., India 175005

**Email:** shashank@iitmandi.ac.in

## ABSTRACT

For large structures subjected to air explosions, there is spatial variation in scaled distance and angle of incidence ($\alpha$) on the structural surface. Currently, the reflection coefficient $C_r$ is estimated either considering normal reflection or including the effect of $\alpha$; however, there is no consensus on a single approach, which may lead to a significant difference in the estimated reflected pressure. Hence, the objective of this study is to investigate the effect of the estimation of $C_r$ on the peak displacement of large homogeneous structures subjected to air explosions. In this study, a finite element model of a large structure, a concrete gravity dam without reservoir, with a height of 60 m and a slope of 0.8:1 on one side with a rigid foundation is considered. The Kinney-Graham, Newmark, and CONWEP models for blast parameters are used to estimate the spatially varying load-history. It is found that there is a difference of 66.7% between the peak crest displacement estimated using the two different approaches. Thereafter, the possibility of using equivalent models is investigated to enhance the computational efficiency. The results of the equivalent model are compared with a full-order model to assess the trade-off between accuracy and computational efficiency.

***Keywords:*** *Concrete gravity dam, Air-blast, Dynamics, Crest displacement.*

# 1. INTRODUCTION

An explosion is a complex phenomenon that releases energy in a radially outward direction and transmits it into the surrounding medium in the form of a shock wave. When the shock wave interacts with a surface, it exerts an incident pressure called peak overpressure, which depends upon the type of explosion, charge weight, detonation location, and angle of incidence. Due to this complexity, it is quite challenging to find the blast load acting on the surface of interest [1]. However, there are several simple techniques available in the literature to find the blast load on structures. One of the most commonly used methods is to assume the formation of Mach Stem before the shock wave arrives at the structure. This is also known as the planar wave assumption, which is very useful to find the blast load parameters such as peak overpressure, reflection coefficient, and positive time duration that act uniformly on the surface [2]. This assumption holds good for small structures compared to the distance of detonation. However, in the case of large structures such as towers, tall buildings, bridges, dams, and others, the surface of interest experiences a spherical shock wave. Therefore, each point on the surface experiences spatially varying blast load parameters.

For the estimation of peak overpressure at a point, various empirical equations are available in the literature based on scaled distance $Z$ (m/kg$^{1/3}$). Several studies have used these empirical relations to determine $P_{so}$ at different points on the structure [1, 3–6]. When the shock wave interacts with the surface at an angle of incidence ($\alpha$), it gets reflected, and the surface experiences an amplified pressure called reflected pressure. This reflected pressure $P_r$ is related to peak overpressure $P_{so}$ as $P_r = C_r P_{so}$, where $C_r$ is the reflection coefficient. The reflection coefficient, in turn, depends upon $P_{so}$ and $\alpha$. Although some studies consider the effect of scaled distance on $P_{so}$, they assume that the shock wave hits the surface at the normal angle of incidence (Fig.1(a)).

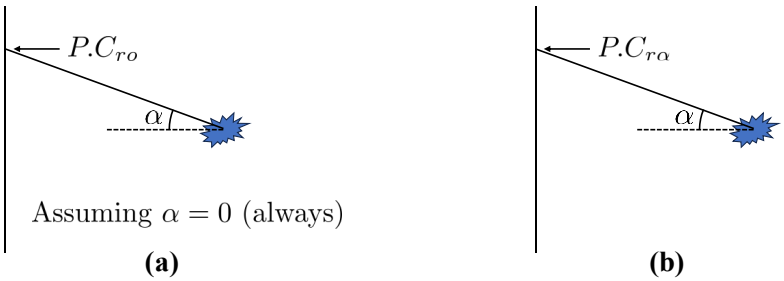


**Figure 1.** Approach used to estimate $Cr$ for **(a)** normal reflection, and **(b)** CONWEP

Due to this, the normal reflection coefficient $C_{ro}$ is used in the calculations [7, 8]. On the other hand, some studies have also considered the influence of angle of incidence $\alpha$ on $C_r$ by estimating $C_r$ based on $P_{so}$ and $\alpha$ (Fig.1(b)). The most common method of finding $C_r$ is using the reflection coefficient chart from the Technical Manual TM 5-1300 [9,10]. Another approach is to use the CONWEP model for the estimation of reflection coefficients [11–14]. Due to this difference in methods of predicting reflection coefficient, the estimated reflected pressure on the surface of interest will also be different. Currently, there is no study available in the literature that highlights this difference in the estimation of blast load and its effect on

the response of structure. Hence, the purpose of this study is to investigate the effect of the estimation of refection coefficient on the response of large structures with and without considering the angle of incidence.

The flow of the paper flows like this: (i) the geometry, mesh convergence, and frequency response function of the 2D model are discussed; (ii) the verification of the finite element model with results reported in the literature is shown; (iii) the approaches for estimation of the blast load are elaborated; (iv) the difference in the response and base shear is pointed out; (v) next, the use of the equivalent models is discussed; and (vi) lastly, the key observations of the study are concluded.

## 2. GEOMETRY AND MESH CONVERGENCE OF SELECTED STRUCTURE

For the purpose of analyses, a typical homogeneous concrete gravity dam (CGD) of height 60 m and downstream slope of 0.8:1 with a rigid foundation and empty reservoir is considered. The dam is subjected to an air explosion on the downstream side of the dam, as shown in Fig.2(a).

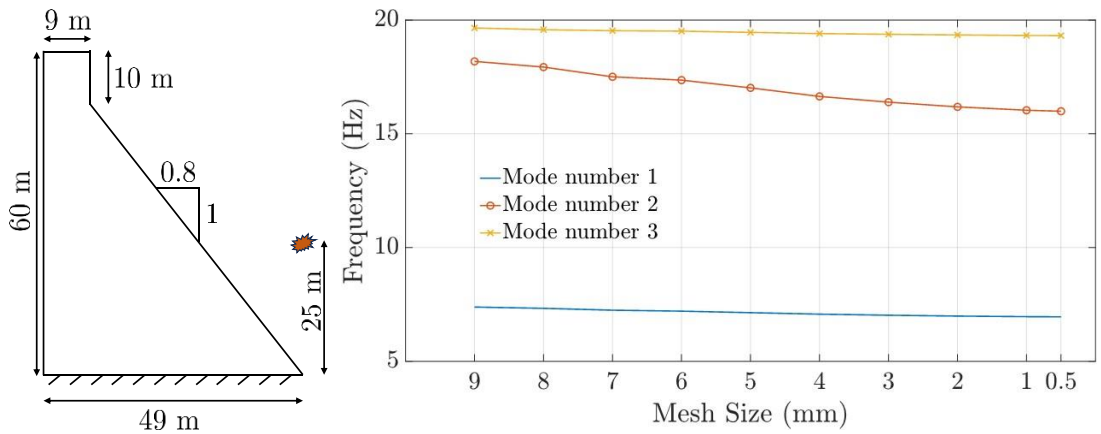


**Figure 2**. **(a)** Typical layout of concrete gravity dam, and **(b)** mesh convergence study of 2D model

A 2D finite element model of the structure is prepared in the Structural Dynamic Toolbox (SDT) of MATLAB [6]. The base of the dam is kept fixed by fixing all degrees of freedom for the nodes at the base. On the other hand, the rest of the nodes of the model are kept free in x, y, and $\theta_z$ directions. The Mindlin shell element of thickness 1 m is employed in the model. The density of the concrete is taken as 2750 kg/m$^{1/3}$, Poisson's ratio 0.2, elastic modulus 34.3 × 10$^9$ N/m$^2$, and damping ratio $\zeta$ as 10%. The mesh convergence study for the model is based on the frequency of the first three modes of the structure, as shown in Fig.2(b) since they have the main contribution in the dynamic response, which is discussed later.

The mesh convergence study clearly indicates that the frequency of the second mode converges for a mesh size of 0.5 m. Furthermore, when a dam is subjected to an air explosion on the downstream side, each point on the downstream side will experience a blast load. Therefore, in order to check the number of modes having the main contribution in the dynamic response due to the applied load on the downstream side, the frequency response function (FRF) of the model is plotted between the crest displacement $x_c$ and the unit force $F$ applied in the x-direction at three mid-heights of the dam for the sake of brevity (Fig.3).

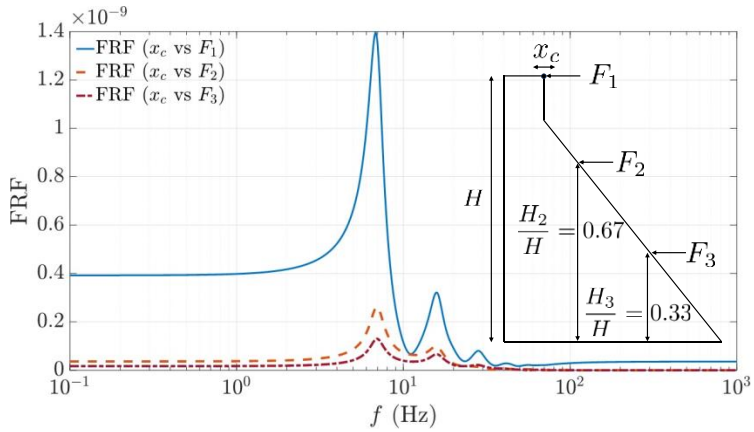


**Figure 3**. Frequency response function (FRF) of 2D model between crest displacement ($x_c$) and forces ($F$) at three mid heights.

The plot suggests that the first three modes of the model will have the main contribution to the dynamic response (crest displacement) of the dam. Please note here that these observations will be used while applying the model reduction technique in further sections. It can also be inferred from Fig.3 that the scale of the FRF decreases as the distance between the node where the load is applied and the crest increases. Because, the contribution of the load applied nearer to the crest will have a greater contribution to the dynamic response compared to the faraway nodes.

## 3. VERIFICATION OF THE FINITE ELEMENT (FE) MODEL

Before further analysis is carried out, the FE model developed in this study is verified by using the results available in the literature for concrete gravity dams without reservoir subjected to ground motion [15]. The dam, with a height of 91.44 m and a downstream slope of 0.8:1, was modelled in SDT. Employing the same philosophy for mesh convergence as discussed in the previous section, the mesh size used for this model comes out to be 0.5 m. The model was fixed at the base by fixing all degrees of freedom at the base nodes. The physical properties of the system, like elastic modulus, Poisson's ratio, damping ratio, and density of concrete, respectively, are taken as $3.447 \times 10^{10}$ N/m$^2$, 0.17, 5%, and 2483 kg/m$^3$ given in Chakrabarti and Chopra [16]. The natural frequency of the dam comes out to be 34.87 rad/s, which is very close to the 36.17 rad/s reported in Chopra [17].

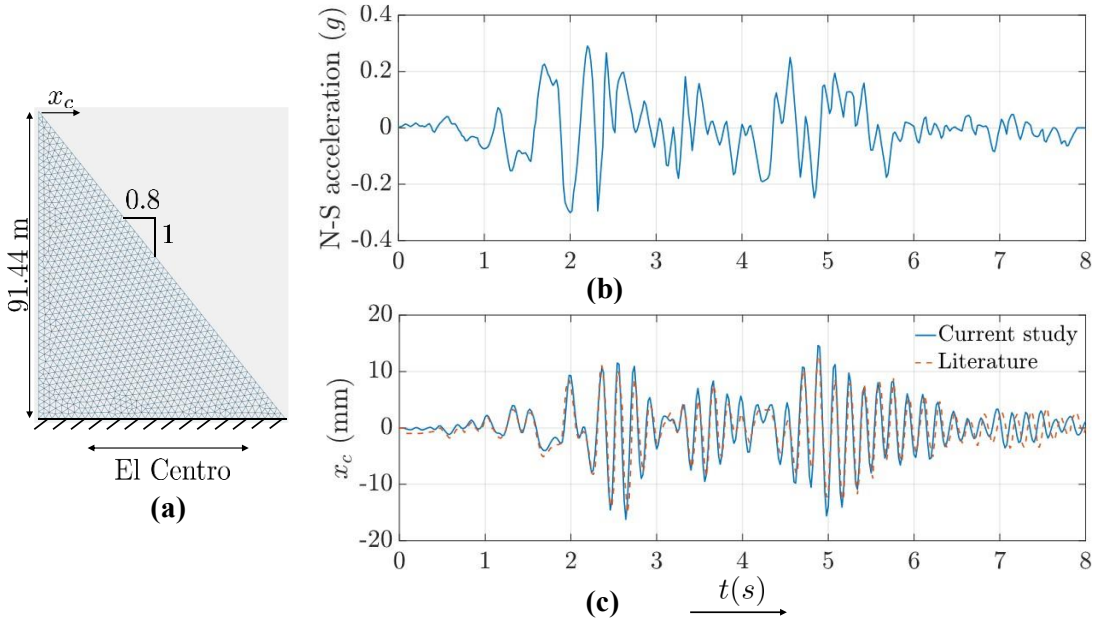


**Figure 4**. **(a)** Discretized 2D model of the dam **(b)** N-S horizontal ground motion of El Centro earthquake 1940 and **(c)** Dynamic response of concrete gravity dam subjected to ground motion for empty reservoir case

In order to simulate the ground motion (horizontal component of the El Centro earthquake, 1940), the plot between N-S ground acceleration and time was adopted from Chopra [16] as shown in Fig.4(a). The plot between the dynamic response of crest displacement ($x_c$) and time ($t$) given in Fig.4(b) suggests that the response in the current study agrees satisfactorily with the literature for empty reservoir case. Also, the peak crest displacement of the dam estimated using the FE model of this study is 16.21 mm, which is in agreement with the one (15.1 mm) reported in Chopra [16], respectively. Hence, it can be concluded that the FE model developed in the current study is verified. It is worth mentioning that the purpose of the current study is to investigate the effect of using different approaches to estimate $C_r$ on the peak displacement of the structure. Therefore, the FE model is verified for the linear elastic case only.

## 4. BLAST PARAMETERS

After the verification of the FE model, further analysis is carried out for the model discussed in Sec.2. The dam is subjected to an explosive charge of weight $W$ = 5 tons of TNT (corresponding to the truck load of FEMA 452 [18]) detonated at a height of 25 m from the toe of the dam (Fig.4(a)). When the shock wave generated by an air explosion interacts with the downstream side of the dam, it exerts pressure on the surface. Since each node on the downstream side has a different stand-off distance ($R$) from the detonation center (Fig.2), the scaled distance ($Z = R/W^{(1/3)}$) also varies spatially, leading to different blast load parameters such as $P_{so}$, $t_d$, and $C_r$. The peak over pressure $P_{so}$ is estimated here using empirical equation Eq.1 given by Kinney and Graham [1].

$$\frac{P_{so}}{P_a} = \frac{808\left[1+\left(\frac{Z}{4.5}\right)^2\right]}{\sqrt{1+\left(\frac{Z}{0.048}\right)^2}\sqrt{1+\left(\frac{Z}{0.32}\right)^2}\sqrt{1+\left(\frac{Z}{1.35}\right)^2}} \quad (1)$$

where $P_a$ is the atmospheric pressure in Pascals (Pa). The positive phase time duration $t_d$ (ms) is estimated using Eq.2 where $W$ is in kg [1].

$$\frac{t_d}{W^{1/3}} = \frac{980\left[1+\left(\frac{Z}{0.54}\right)^{10}\right]}{\left[1+\left(\frac{Z}{0.02}\right)^3\right]\left[1+\left(\frac{Z}{0.74}\right)^6\right]\sqrt{1+\left(\frac{Z}{6.9}\right)^2}} \quad (2)$$

As discussed previously, when a shock wave interacts with the surface, it gets reflected and experiences an amplified pressure called reflected overpressure. The estimation of reflected pressure requires a reflection coefficient, which can be calculated using two different approaches.

**(i) Normal reflection approach** - The most common approach assumes that the shock wave hits the surface at a normal angle of incidence, resulting in a normal reflection coefficient ($C_{ro}$), and disregards the effect of angle of incidence. There are several empirical relations available in the literature for the estimation of $C_{ro}$; however, in this study, it is calculated using the piece-wise equations Eq.3 given by Newmark [19].

$$C_{ro} = \begin{cases} 2 + \frac{6\,P_{so}}{P_{so}+7P_a}, & P_{so} \le 10^6 Pa \\ 4 + \log_{10}(P_{so}10^{-5}), & P_{so} \ge 10^6 Pa \end{cases} \quad (3)$$

**(ii) CONWEP approach** - The second approach considers the effect of angle of incidence ($\alpha$) on the calculation of reflection coefficient $C_{r\alpha}$ and can be estimated by Eq.4 as used in different studies [12, 14].

$$C_{r\alpha} = C_{ro}(\cos\alpha)^2 + (1-\cos\alpha)^2 \quad (4)$$

With the knowledge of the reflection coefficient and other parameters of blast load, the linearly decaying pressure-time history for each node on the downstream side can be estimated using equations as follows:

$$P(t) = \begin{cases} P_r\left(1-\frac{t}{t_d}\right), & t \le t_d \\ 0, & t \ge t_d \end{cases} \quad (5)$$

The different pressure-time histories were estimated using Eq.5, and the variation of the blast-load parameters was plotted with the height of the dam ($y$). It is important to note here that,

although the mesh size converges at 0.5 m (Fig.2(b)), which is also shown in Fig.5(a), there is still some error while estimating the angle of incidence ($\alpha$) as shown in Fig.5(b).

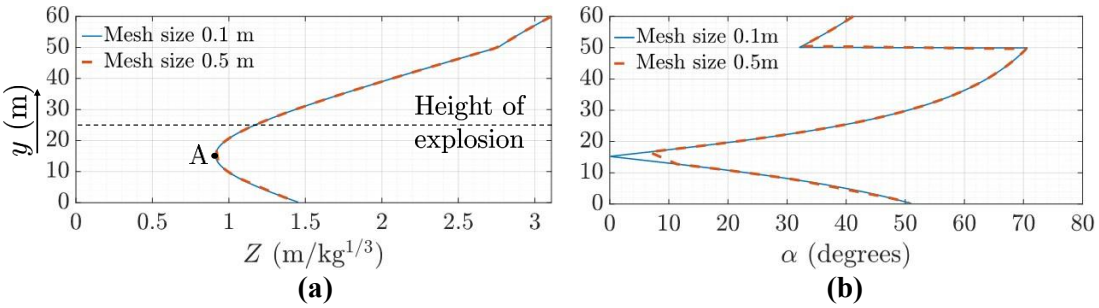


**Figure 5.** Variation of **(a)** scaled distance $Z$, and **(b)** angle of incidence $\alpha$ for mesh size of 0.5 m and 0.1 m with the downstream surface (height) of dam ($y$)

Therefore, in order to observe the variation of load parameters on the surface of the dam, a mesh size of 0.1 m is used for further analysis (Fig.5). It can be observed in Fig.5(a) that the scaled distance ($Z$) changes with each node, and the farthest node from the detonation location, which is the crest, has the largest scaled distance. It is also interesting to note that the height of burst and the height of point with the minimum scaled distance are different. The scaled distance is minimum at a height of 15.2 m (point A), where the angle of incidence is also minimum, i.e., 0° (Fig.5(b)). At the point of minimum scaled distance on the downstream side, $P_{so}$ is maximum (1.22 MPa) and $t_d$ is minimum (7.4 ms), as shown in Fig.6(a) and (b).

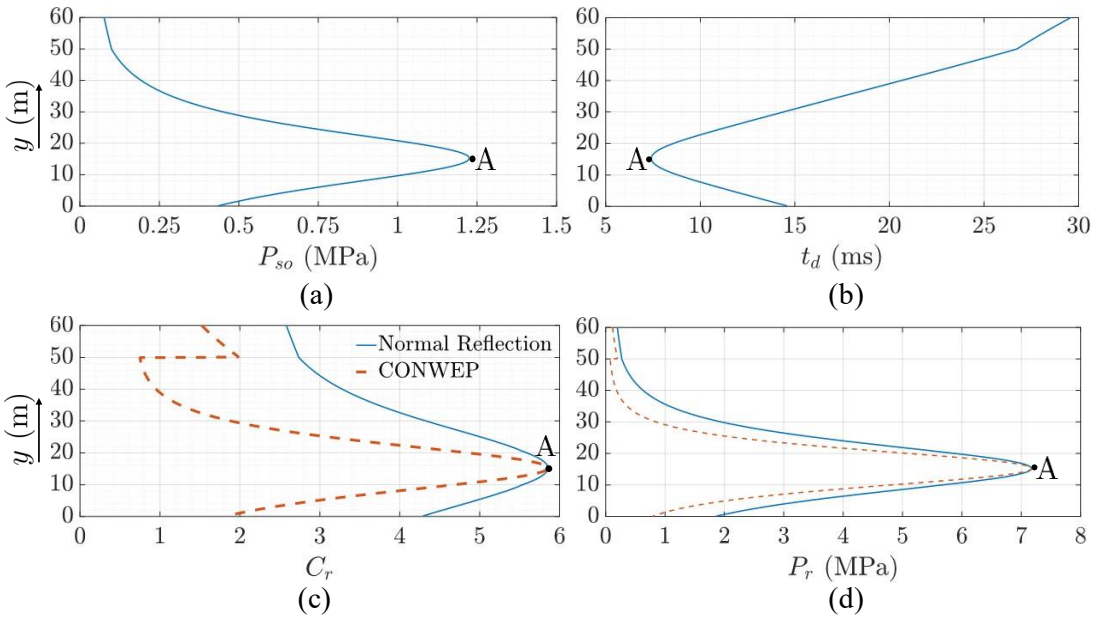


**Figure 6.** Variation of **(a)** peak over pressure ($P_{so}$), **(b)** positive phase time duration ($t_d$), **(c)** reflection coefficient ($C_r$), and **(d)** reflected over pressure ($P_r$) with the downstream surface (height) of dam ($y$)

Here, the incident wave will reflect normally from the surface, and the reflection coefficient will be at its maximum. This is also justified by the plot given in Fig.6(c), where the $C_r$ estimated by the two different approaches is the same, i.e., 5.85 and therefore the same $P_r$

(Fig.6(d)). It is also worth mentioning that there is a sudden change in the angle of incidence ($\alpha$) at a height of 50 m due to a change in the curvature from the crest to the downstream side of the dam (Fig.2(a)). This abrupt change in $\alpha$ is responsible for the abrupt change in $C_r$ estimated using CONWEP (Fig.6(c)), which is also reflected in the estimation of $P_r$ (Fig.6(d)).

# 5. RESPONSE ANALYSIS OF CGD

## Crest Displacement

In order to estimate the force at each node, the pressure is multiplied by its contributing area, which is equivalent to the product of the mesh size (0.1 m) and the width of the section (1 m). The load is estimated using two different approaches, i.e., (i) normal reflection and (ii) CONWEP, which are applied to the nodes of the downstream side in the negative x-direction. The FEM analysis is carried out to find the crest displacement of the dam.

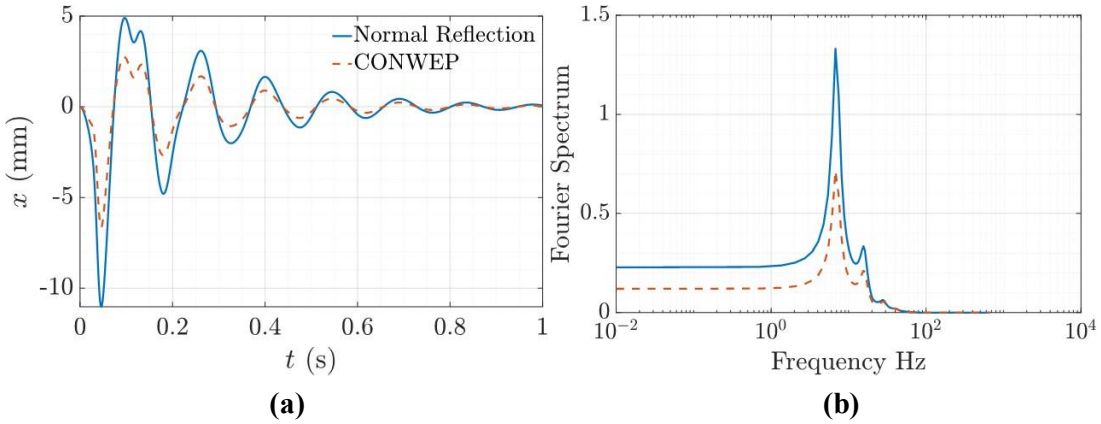


**Figure 7. (a)** Crest displacement-time history of the structure estimated using normal reflection coefficient and CONWEP, **(b)** Fourier spectrum of the crest displacement-time history

It can be observed from Fig.7(a) that the displacement due to normal reflected pressure is higher than the one estimated using CONWEP; however, both curves follow the same trend and the same frequency content (Fig.7(b)). The Fourier spectrum of the response of two approaches shows the same trend and has peaks at the first three natural frequencies of the model (6.77 Hz, 15.6 Hz, and 27.7 Hz), as shown in Fig.3. This is due to the fact that only the peak values of pressure and load for the nodes are different between the two approaches (Fig.6). The peak crest displacement of the structure comes out to be 11 mm and 6.6 mm for the two approaches, respectively. This shows that the normal reflection approach overestimates the peak displacement by 66.7 % in this case and therefore can lead to a highly over-conservative design.

## Total Force

For the loading part, since different pressure-time histories act on different nodes of the structure, it is not practical to analyse the frequency content of all the histories. Therefore, the authors believe that plotting the frequency content of the net total force ($F$) should give some insights. The total force to the blast load estimated using two approaches is evaluated by adding load-time histories at all the nodes (Fig.8(a)).

The peak values of the total load come out to be 200 MN and 150 MN for normal reflection and the CONWEP approach, respectively, with the difference between the two being 33.3%.

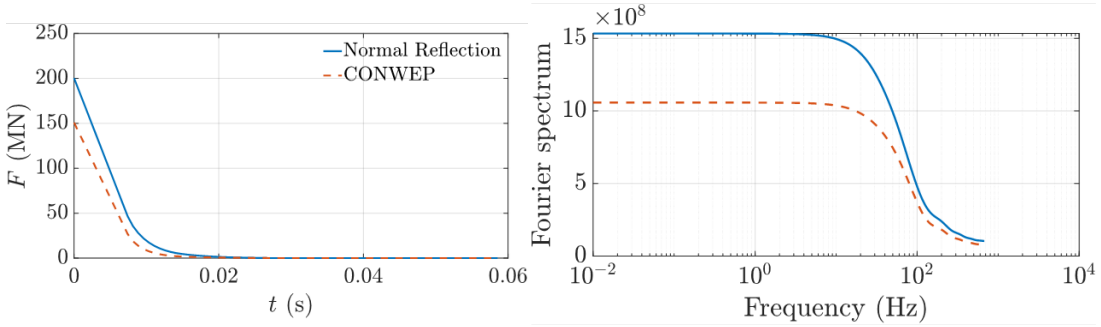


**(a)** **(b)**

**Figure 8. (a)** Total load-time history for the applied loading on dam, **(b)** frequency content of the total load

Furthermore, the frequency content of the total load indicates that the modes that have the main contribution to the dynamic response belong to the band of frequencies of the applied load. It also shows that since the contribution of higher frequencies of the applied load (Fig.8(b)) and higher modes of dam (Fig.3) decreases, their product (FRF × frequency content of applied load) also decreases significantly, which is already reflected in Fig.7(b). This observation can be used to increase computation efficiency, which will be explored in the next section.

# 6. EQUIVALENT MODEL FOR COMPUTATIONAL EFFICIENCY

In a previous study by Goel and Pathak [20], it was concluded that there is a significant difference in the computation time between the Newmark and state space approach with model reduction for planar shock waves. This study uses state space approach to further investigate the effect of the number of modes considered in the analysis of CGD subjected to a spherical shock wave. Since the model is discretized to accurately define the stiffness of the dam, there are N = 5,37,711 degrees of freedom (DOF) in the system, which further equals the number of modes. As the number of modes increases, the computation time of the analysis also increases. However, one can significantly increase the efficiency of the analysis by decreasing the number of modes [21].

The governing equation of motion after modal decomposition of the above system can be written as

$$\ddot{\boldsymbol{\eta}}_i + 2\zeta_i\omega_i\dot{\boldsymbol{\eta}}_i + {\omega_i}^2\boldsymbol{\eta}_i = \boldsymbol{\phi}_i^T \boldsymbol{d}F/\boldsymbol{\mu}_i \tag{6}$$

where $\boldsymbol{\eta}_i$, $\omega_i$, $\boldsymbol{\mu}_i$ and $\boldsymbol{\phi}_i$ are the modal coordinate, natural frequency, modal mass and mode shape of the $i^{th}$ mode, $\boldsymbol{d}$ is the influence vector such that the value is 1 for DOF where load is applied else equal to zero and $F$ is the applied force. Thus, the total response $\boldsymbol{x}_m$ of the $m^{th}$ DOF can be written as (if one considers only first 'n' modes where n < N)

$$\boldsymbol{x}_m = \sum_{i=1}^{n} \boldsymbol{\phi}_i(m)\boldsymbol{\eta}_i \quad + \text{ truncation error} \tag{7}$$

where $\boldsymbol{\phi}_i(m)$ is the element corresponding to $m^{th}$ DOF in $i^{th}$ mode shape vector. If $k^{th}$ mode is significant in the response, the equation of motion can be written as

$$\ddot{\boldsymbol{\eta}}_k + 2\zeta_k\omega_k\dot{\boldsymbol{\eta}}_k + {\omega_k}^2\boldsymbol{\eta}_k = \boldsymbol{\phi}_k(j)F/\boldsymbol{\mu}_k \tag{8}$$

where, $j$ is the DOF where load is applied, $\boldsymbol{\phi}_k(j)$ (which is equal to $\boldsymbol{\phi}_k(d)$ is the element corresponding to $j^{th}$ DOF in $k^{th}$ mode shape vector. Thus, the approximate response of the $m^{th}$ DOF due to load at the $j^{th}$ DOF (governed by $k^{\text{th}}$ mode only) can be written as

$$\boldsymbol{x}_{mj} \approx \boldsymbol{\phi}_k(j)\boldsymbol{\eta}_k \tag{9}$$

Substituting Eq.9 into Eq.8, we get an equation of SDOF system as

$$\frac{\boldsymbol{\mu}_k}{\boldsymbol{\phi}_k(m)}\ddot{\boldsymbol{x}}_{mj} + \frac{2\boldsymbol{\mu}_k\zeta_k\omega_k}{\boldsymbol{\phi}_k(m)}\dot{\boldsymbol{x}}_{mj} + \frac{\boldsymbol{\mu}_k\boldsymbol{\omega}_k^2}{\boldsymbol{\phi}_k(m)}\boldsymbol{x}_{mj} = \boldsymbol{\phi}_k(j)F \tag{10}$$

Since the load is applied on the nodes of downstream side of dam, the total response $x_c$ at crest will be the superposition of response of all SDOF systems subjected to point load $\phi_k(j)F$.

$$x_c = \sum_{\forall j} \boldsymbol{x}_{mj} \tag{11}$$

Also, the load is estimated here using the CONWEP approach only because the purpose is to investigate the computation efficiency. This method is very useful to reduce the computation time of the analysis; however, there will be some error due to the reduction of model, as shown in Fig.9.

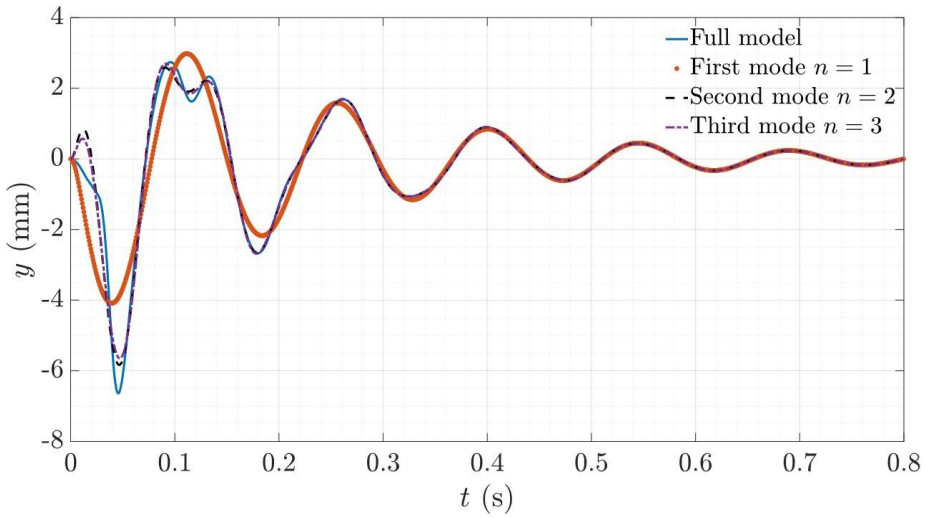


**Figure 9.** Comparison of response due to number of modes included in the analysis

The plot in Fig.9 suggests that as the number of modes included in the analysis increases, the responses tend to overlap with the full model. The curves have significant differences in the

transient state and overlap each other in the steady state. These observations show that the response of the structure can be estimated by only including the number of modes having the main contribution. The peak crest displacement of the plots for 1 mode, 2 modes, 3 modes, and the full model comes out to be 4, 5.82, 5.64, and 6.63 mm, respectively. Hence, the errors in the estimation of $x_c$ for the first three modes are 39.6%, 12.21%, and 14.93%. This difference is due to the accumulated contribution of the rest of the modes in the dynamic response. The computation time measured on a system with 192 GB RAM, an Intel Xeon Gold 6338N CPU, and a clock speed of 2.20 GHz using the state space approach along with the model reduction technique (30 modes + static correction), which is as good as a full model in terms of accuracy, came out to be 331.65 s. However, the computation time for the approximate response using the equivalent model with first 1 mode, first 2 modes and first 3 modes comes out to be 198.3 s, 207.09 s and 207.43 s. In a previous study by Goel and Pathak [20], it was reported that the Newmark method that uses the full model takes about 22 times more computation time than that of the state space approach with the model reduction technique. In this study, we have further attempted to enhance the efficiency by considering only the first few modes, which take about 331.65/207.43=1.6 times less computation time compared to the state space approach with model reduction technique, at a cost of accuracy (of about 10%).

# 7. CONCLUSION

In the current geopolitical scenario, there is a necessity to consider the blast load in the design calculations of structures. The blast load is a dynamic load that depends on the scaled distance and type of explosion. In the case of an air explosion, the basic load parameters are peak overpressure, positive phase time duration, and reflection coefficient. In this study, the emphasis is given on the approaches used to estimate the reflection coefficient and its effect on the peak crest displacement.

The FE model developed in this study is verified by comparing the fundamental frequency and the dynamic response of the crest of the dam subjected to ground motion. The same philosophy was used to model a typical concrete gravity dam subjected to an air explosion on the downstream side. Since the blast load due to the air explosion is considered only in the x-direction, the model is expected to behave in a plane strain condition; therefore, the analysis is carried out only for the 2D model. This study investigated the effect of the inclusion of the angle of incidence while estimating reflection coefficient on the response of the structure. The analysis shows that for the case considered in this paper, there is a difference of 66.7% in the peak crest displacement between normal reflection and the CONWEP model. Furthermore, the normal reflection estimates 33.3% total load more than that of the CONWEP model. Hence, it can be concluded that the use of normal reflection, especially in large structures, may lead to over-conservative design. In addition to that, the effect of the number of modes included in the analysis is also explored by using the equivalent models in this study. It is concluded that for preliminary analysis, instead of analysing the full model, only the modes having the main contribution to the dynamic response can be included to reduce the computation time. This approach of analysis will be used in the case of threat scenario modelling [22], where a number of simulations will be carried out for the same model.

## ACKNOWLEDGMENTS

This research is funded by Science and Engineering Research Board (SERB), Department of Science and Technology (DST), India (grant number SRG/2023/000109).

## REFERENCES

[1] Kinney, G. F., & Graham, K. J. (2013). *Explosive shocks in air*. Springer Science & Business Media.

[2] IS-4991. *Criteria for blast resistant design of structures for explosions above ground.* Bureau of Indian Standards, 1968.

[3] Brode, H. L. (1955). Numerical solutions of spherical blast waves. *Journal of Applied physics*, *26*(6), 766-775.

[4] Held, M. (1983). Blast waves in free air. *Propellants, Explosives, Pyrotechnics*, *8*(1), 1-7.

[5] Sadovskiy, M. A. (2004). Mechanical effects of air shockwaves from explosions according to experiments. *Sadovskiy MA Selected Works: Geophysics and Physics of Explosion*.

[6] Baker, W. E., Cox, P. A., Kulesz, J. J., Strehlow, R. A., & Westine, P. S. (2012). *Explosion hazards and evaluation*. Elsevier.

[7] Zhang, R., & Phillips, B. M. (2016). Performance and protection of base-isolated structures under blast loading. *Journal of Engineering Mechanics*, *142*(1), 04015063.

[8] Kalateh, F. (2019). Dynamic failure analysis of concrete dams under air blast using coupled Euler-Lagrange finite element method. *Frontiers of Structural and Civil Engineering*, *13*, 15-37.

[9] Department of Defense. (2008). Structures to resist the effects of accidental explosions. *UFC 3-340-02*.

[10] Karlos, V., & Solomos, G. (2013). Calculation of blast loads for application to structural components. *Luxembourg: Publications Office of the European Union*, *5*.

[11] Randers-Pehrson, G., & Bannister, K. (1997). Airblast loading model for DYNA2D and DYNA3D.

[12] Goel, M. D. (2015). Blast: Characteristics, loading and computation—An overview. *Advances in Structural Engineering: Mechanics, Volume One*, 417-434.

[13] Artero-Guerrero, J., Pernas-Sánchez, J., & Teixeira-Dias, F. (2017). Blast wave dynamics: The influence of the shape of the explosive. *Journal of hazardous materials*, *331*, 189-199.

[14] Markose, A., & Rao, C. L. (2017). Mechanical response of V shaped plates under blast loading. *Thin-Walled Structures*, *115*, 12-20.

[15] Chakrabarti, P., & Chopra, A. K. (1972). Hydrodynamic pressures and response of gravity dams to vertical earthquake component. *Earthquake Engineering & Structural Dynamics*, *1*(4), 325-335.

[16] Chopra, A. K. (1967). Hydrodynamic pressures on dams during earthquakes. *Journal of the Engineering Mechanics Division*, *93*(6), 205-223.

[17] Chopra, A. K. (1967). Reservoir-dam interaction during earthquakes. *Bulletin of the Seismological Society of America*, *57*(4), 675-687.

[18] Assessment, F. R. (2005). A how-to guide to mitigate potential terrorist attacks against buildings. *FEMA*, *452*, 3-6.

[19] Beshara, F. B. A. (1994). Modelling of blast loading on aboveground structures—I. General phenomenology and external blast. *Computers & Structures*, *51*(5), 585-596.

[20] Goel, T and Pathak, S. (2023) An algorithm for a certain reliability problem. *Presented in 9th International Congress on Computational Mechanics and Simulation (ICCMS)*. Gandhinagar, Indian Institute of Technology.

[21] Pathak, S., Piron, D., Paknejad, A., Collette, C., & Deraemaeker, A. (2022). On transmission Zeros of piezoelectric structures. *Journal of Intelligent Material Systems and Structures*, *33*(12), 1538-1561.

[22] Pathak, S., & Ramana, G. V. (2020). Probabilistic Characterization of Nuclear-Blast Loads. *Journal of Structural Engineering*, *146*(5), 04020055.

# RESIDUAL AXIAL CAPACITY OF GROUTING SLEEVE CONNECTED PRECAST CONCRETE COLUMNS AFTER EXPLOSIONS

*Jinxian Lyu[1], Hao Wu[2], Gongqing Chen[3], and Yuehua Cheng[4]*

[1] PhD student, Tongji University, 2111022@tongji.edu.cn.

[2] Professor, Tongji University, wuhaocivil@tongji.edu.cn.

[3] PhD student, Tongji University, 2110378@tongji.edu.cn.

[4] Postdoctoral fellow, Tongji University, yhcheng@tongji.edu.cn.

**Corresponding Author: Yuehua Cheng, PhD.**

College of Civil Engineering, Tongji University, Shanghai, China, 200092

**Email:** yhcheng@tongji.edu.cn

## ABSTRACT

In virtue of the convenient construction and environmental protection, the grouting sleeve connected precast concrete (PC) column gradually replaces the traditional reinforced concrete column as the main vertical load-bearing structural member. Nevertheless, under the aggravation of deliberate and accidental explosions, there is a lack of research on the blast resistance of PC columns, especially the residual capacity which is closely related to the collapse of building structures. In this study, the post-blast residual axial capacity of PC and RC columns was assessed and compared on the basis of the high-fidelity numerical simulation. Firstly, the reliability of the finite element analysis method in the explosion and axial compressive stages was verified by reproducing the explosion test of PC columns and post-blast axial compressive test of RC columns conducted by the authors, respectively. Then, based on Chinese structural specifications, the actual PC and RC columns were designed, and the corresponding finite element models were established. Furthermore, the residual capacity of the two types of columns was analysed and compared under different scaled distances and designed basis threats demanded by the Federal Emergency Management Agency. It derives that, PC columns showed more excellent blast resistance, namely slighter lateral deformation and greater residual load-bearing capacities, compared with the RC columns. Finally, the practical threat-based design recommendations for PC and RC columns were put forward.

***Keywords:*** *Residual Axial Capacity, Precast Concrete Column, Blast loadings, Grouting Sleeve, Numerical Simulation.*

# 1. INTRODUCTION

In virtue of the convenient construction and environmental protection, the precast concrete (PC) structures gradually replace the traditional cast-in-place reinforced concrete (RC) structures in new-built buildings. However, terrorist and accidental explosions occur frequently around the world, aggravating the risk of structural damage and collapse of PC buildings. In 1968, the gas explosion of Ronan Point apartment tower led to the fracture of PC slabs, resulting in the collapse of the structure [1]. Besides, the PC walls at the front of Khobar apartment tower were severely damaged under the terrorist explosion in 1996 [2]. As the primary structural members in building structures, the bearing capacity degeneration of PC columns may induce the large-scale collapse of the entire structures, causing the personnel and property losses. Consequently, it is essential to investigate the blast resistance and residual capacity of PC columns.

Over the past years, many scholars conducted the field explosion tests and numerical simulations on RC columns. Williamson et al. [3-5] performed the close-in and contact explosion tests on 16 RC columns, and studied the influences of the cross-sectional shape, slenderness ratio, reinforcement ratio on the dynamic response of columns. It was concluded that the direct shear failure was the main failure mode of columns under close-in explosion. Braimah and Siba [6] performed the explosion tests of 16 full-scale RC columns, and the influences of scaled distance, transverse reinforcing details and axial compressive ratio were analyzed. It was indicated that the stirrup spacing and the position of splice region had a great influence on the blast resistance of columns under close-in explosion. In terms of residual capacity, Chen et al. [7] conducted the post-blast axial compressive test on RC columns under different charge weights and axial compressive ratios. Furthermore, the damage assessments of RC columns were carried out on the basis of the index of residual axial bearing capacity. In order to assess the damage degree of RC column under close-in blast loads, the axial compressive test of blast-damaged RC column was carried out by Shi et al. [8], in which the effects of scaled distance as well as axial compressive ratio was considered. Nevertheless, the field tests for the PC columns under blast loads are still limited. Yu et al. [9] performed a contact explosion test of one RC and six PC columns with grouting sleeve connections. The effects of connection types, initiation positions and charge weights on the damage mode of columns were examined. The results showed that the grouting sleeves improved the blast resistance of columns under contact explosion. For the numerical simulation, plenty of studies were carried out on RC columns [7, 10, 11], while there is a shortage of research on PC columns. Only Yu et al. [9] reproduced the conducted explosion test of PC columns and performed the parametric analysis on reinforcement ratios, cross-sectional sizes, axial force, charge weights and positions.

Generally, there is a lack of experimental and numerical studies on the blast resistance of PC columns under close-in explosion, especially the residual capacity which is closely related to the collapse of building structures. In this study, the accuracy of the finite element (FE) analysis method in the explosion and axial compressive stages are firstly examined by simulating the explosion test of PC columns [12] and post-blast axial compressive test of RC columns [13] conducted by the authors, respectively. Then, based on Chinese structural specifications, the protype PC/RC columns are designed, and the corresponding FE models are established.

Furthermore, the residual capacity of the two types of columns is analyzed and compared under different designed basis threats demanded by the Federal Emergency Management Agency (FEMA). Finally, the specific threat-based design recommendations of PC/RC columns are put forward.

# 2. FE ANALYSIS METHOD AND VALIDATION

## 2.1. Explosion test on PC columns

According to Chinese *Code for seismic design of buildings*, (GB 50011-2010) [14] and *Technical specification for precast concrete structures*, (JGJ 1-2014) [15], four PC columns with grouting sleeve connections were fabricated. The column height was 3 m with the sectional size of 0.25 m×0.25 m. The reinforcing details are presented in Figure 1(a). Figure 1(b) further presents the test setup. The PC column was fixed in the blast resistance instrument through the locking caps at the top and the mechanical jacks at the bottom. Besides, the RC walls of the instrument surrounded the side faces to avoid the diffraction of blast waves. Moreover, the constant axial force was applied by the gas cylinder to describe the stress state of columns during the service stage. For the measuring instruments, five displacement transducers (D1-D5) were arranged along the column height with the 500 mm-vertical spacing. As shown in Table 1, total four explosion scenarios were conducted on PC columns with grouting sleeve connections.

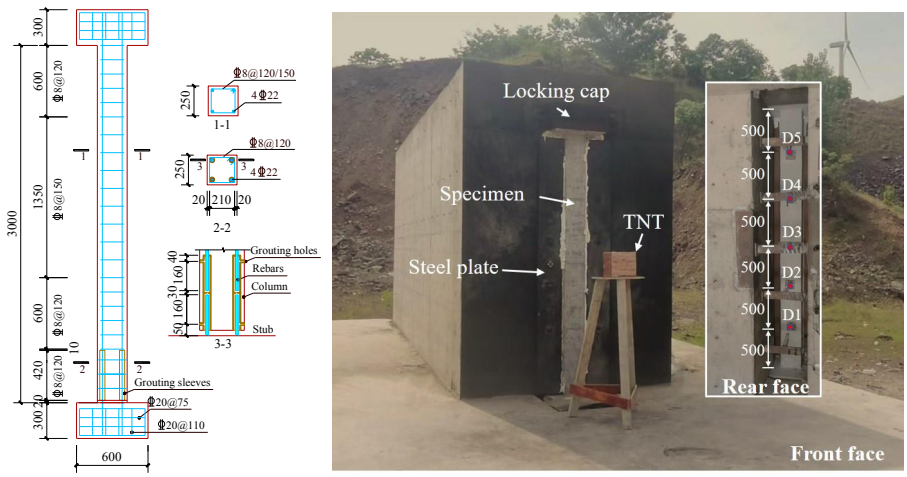


(a) (b)

**Figure 1.** Explosion test on PC columns (a) reinforcing details [12] (b) test setup (unit: mm).

**Table 1.** Explosion test scenarios

| No. | Charge weight (kg) | Standoff distance (mm) | Burst height (mm) | Axial compressive ratio |
|---|---|---|---|---|
| P-1 | 18 | 1600 | 1500 | 0.18 |

| | | | | |
|---|---|---|---|---|
| P-2 | 18 | 1300 | 1500 | 0.18 |
| P-3 | 18 | 1300 | 1500 | 0.36 |
| P-4 | 18 | 1300 | 750 | 0.18 |

Figure 2 presents the 1/2 FE model of the above-mentioned explosion test owing to the symmetry of test set-up. The concrete, as well as grouting sleeves and material are discretized by solid elements with 10-mm mesh sizes. The rebars adopt the Hughes-Liu beam elements with the mesh sizes of 10 mm. The MM-ALE solid elements are selected for the air and TNT with the mesh sizes of 30 mm and 15 mm, respectively. In terms of contact algorithms, the contact between sleeves, lateral restraints and concrete is characterized by the keyword *CONTACT_AUTOMATIC_SURFACE_TO_SURFACE. The grouting sleeves and material are combined by using the sharing node method. In addition, the fluid-structure interactions between concrete and rebars, columns and air, as well as grouting material and rebars are all realized by adopting the keyword *CONSTRAINED_LAGRANGE_IN_SOLID. For the loading condition, the keyword *LOAD_SEGMENT_SET is utilized for applying uniform distributed loads at the stubs. The rigid walls and rigid ground are realized by adopting the material *MAT_RIGID.

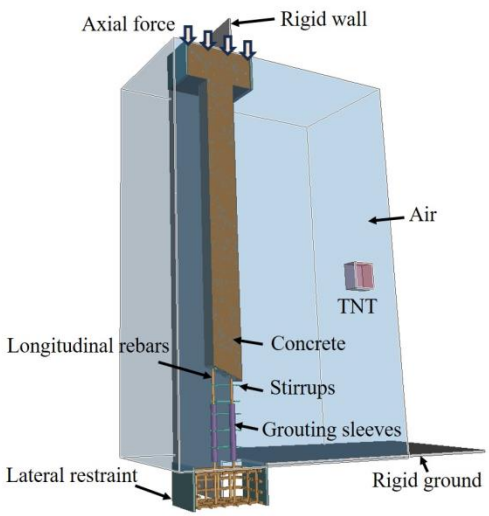


**Figure 2.** Finite element model of explosion test on PC columns.

The *MAT_072R3 (K&C) model is used to describe the dynamic behaviours of concrete and grouting material under explosions, in which the effects of strain rate and damage, as well as strain hardening and softening behaviours are considered. The *MAT_003 material model is applicable to describe the isotropic and kinematic hardening plasticity, and thus it is used to

reflecting the material property of sleeves and rebars embedded in columns. Combined with the *MAT_009 material model and *EOS_001 equation of state, the air is regarded as the non-viscous ideal gas. By utilizing the *MAT_008 material model and *EOS_003 equation of state, the final reaction heat of TNT is determined in the explosive detonation process.

Figure 3 compares the damage patterns of columns after the explosion. The P-1 column experimentally and numerically exhibits flexural failure with the concrete cracks at the rear face along the mid-height. Additionally, the P-2 and P-3 columns suffer serious local damage at the mid-height combined with the global flexural deformation both in the simulation and test. For the P-4 column, the combination of shearing, flexural and local failure occurs at the bottom. Figure 4 and Table 2 compare the simulated and tested lateral displacement-time histories. In each scenario, the relative deviation between the experimental and numerical maximum lateral displacements at measure points D2-D4 do not exceed 25%, reflecting the reliability of FE analysis method. It should be pointed out that the K&C model cannot comprehensively describe the complex failure modes of the PC-4 column, and thus the deviations are greater than those in other scenarios.

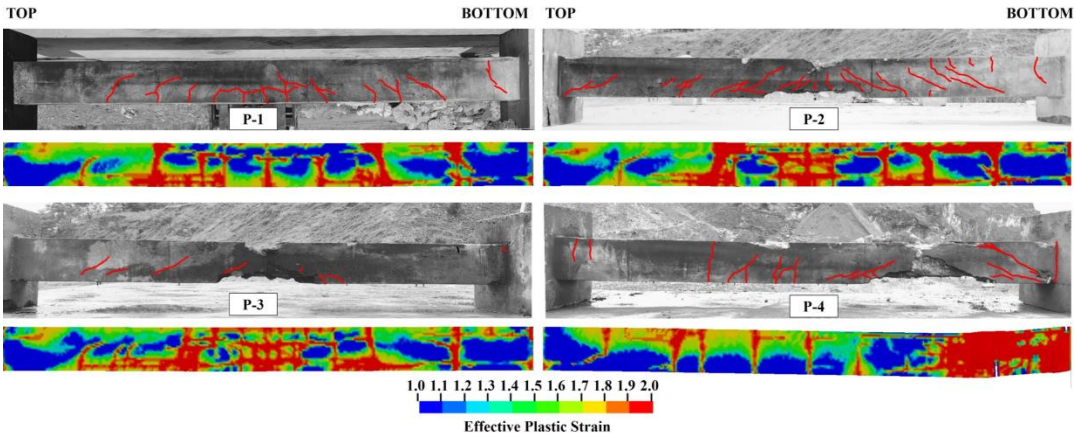


**Figure 3.** Post-blast damage contour of columns at side face [12].

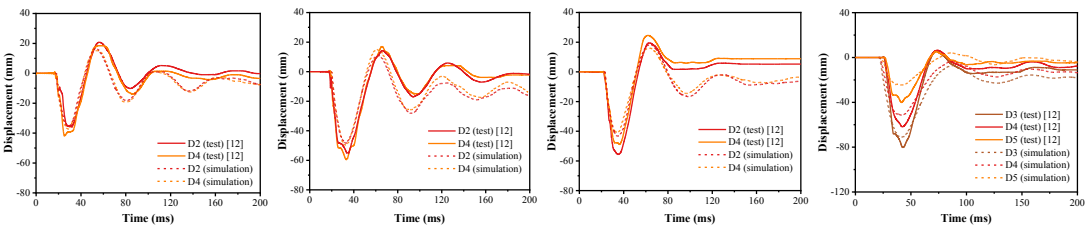


(a) (b) (c) (d)

**Figure 4.** Comparisons of lateral displacement-time histories at (a) P-1 (b) P-2 (c) P-3 (d) P-4.

**Table 2.** Comparisons of maximum lateral displacement

| | P-1 | | P-2 | | P-3 | | P-4 | | |
|---|---|---|---|---|---|---|---|---|---|
| Measuring point | D2 | D4 | D2 | D4 | D2 | D4 | D3 | D4 | D5 |
| Test (mm) | 37.0 | 42.0 | 55.2 | 59.6 | 55.6 | 48.8 | 80.0 | 61.4 | 40.1 |
| Simulation (mm) | 35.2 | 37.3 | 48.3 | 49.6 | 43.3 | 41.0 | 71.0 | 51.5 | 24.5 |
| Deviation | 4.9% | 11.2% | 12.5% | 16.8% | 22.1% | 16.0% | 11.3% | 16.1% | 38.9% |

## 2.2. Post-blast axial compressive test on RC columns

Due to the lack of axial compressive test on PC column, the previously conducted post-blast axial compressive test on RC columns [13] was reproduced to verify the reasonability of FE analysis method at the axial compressive stage. As shown in Figure 5(a), the field contact explosion test on three 1/2-scale RC column (R-1, R-2, and R-3) was conducted with the TNT charge weight of 0.5 kg, 1.0 kg, and 2.0 kg, respectively. Subsequently, the axial bearing capacities of these post-blast columns were experimentally examined through a hydraulic testing machine, as presented in Figure 5(b). The columns were total 3.6 m in height with a foundation of 1.1 m×1.1 m×0.6 m. The circular cross-sectional size was 450 mm in diameter, and the concrete cover was 25 mm in depth. There were 16 longitudinal rebars with the diameter of 16 mm, and the stirrups with the diameter of 8 mm were spaced at 100 mm along the densified zone and 150 mm along the rest zone. The HPB300 and HRB400 rebars were used for stirrups and longitudinal rebars, respectively. The reinforcing details were given in Ref. [13].

Since to improve the computation efficiency, a 1/2 FE model for the above explosion and axial compressive tests is established owning to the symmetry of test set-up. The FE analysis method for the explosion stage is identical to that in Section 2.1. In the axial compressive stage, the corresponding FE model is presented in Figure 5(c). The bottom of foundation is fixed by restraining all degrees of freedom. The axial force is applied by the displacement-controlled pushdown for the top loading plate. Additionally, the contact between the top of columns and the plates is characterized by using the keyword *AUTOMATIC_SURFACE_TO_SURFACE. Between the simulation of explosion and axial compressive stages, the restart algorithm is utilized to deliver the damage and failure of RC columns by using the keyword *STRESS_INITIALIZATION. Figure 6 compares the test and simulated residual axial load-bearing capacity for RC columns. The relative deviations of the peak axial load-bearing capacity for R-1, R-2 and R-3 are 9.3%, 1.4% and 2.3%, respectively. Besides, attributed to the cracks of core concrete during the transportation, the tested axial stiffness of R-1 is less than that in the simulation. Generally, the simulation results are agreed well with the test data, and thus the present FE analysis method is suitable for predicting the post-blast axial load-bearing capacity of columns.


(a) (b) (c)

**Figure 5.** Post-blast axial compressive test on RC columns (a) explosion stage [13] (b) axial compressive stage [13] (c) FE model.

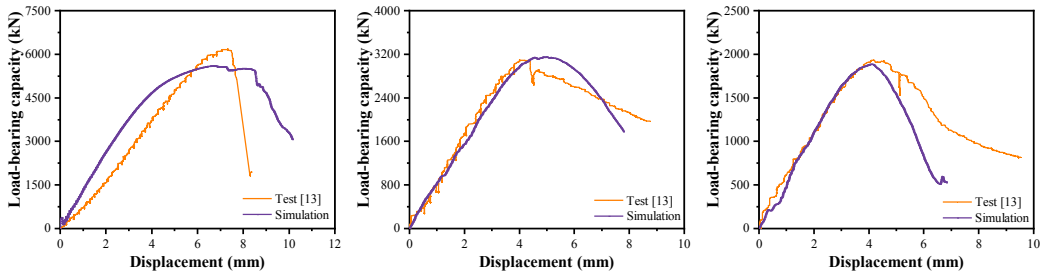


(a) (b) (c)

**Figure 6.** Comparisons of residual axial load-bearing capacity for RC column (a) R-1 (b) R-2 (c) R-3.

# 3. BLAST-RESISTANT ANALYSES OF PROTOTYPE COLUMNS

## 3.1. Designs and FE models of columns

According to GB 50011-2010 [14] and JGJ 1-2014 [15], the height of designed PC/RC columns were all 3000 mm for residential buildings, and the sectional size was 600 mm×600 mm. The reinforcing details are presented in Figure 7. The diameters of longitudinal rebars and stirrups were 25 mm and 8 mm. The yield strength of rebars and compressive strength of concrete were 400 MPa and 40 MPa, respectively. Moreover, the grouting sleeves were 450 mm in length and 50 mm in diameter, configured at the PC column bottom. The 1/2 FE models for PC/RC column were established, as shown in Figure 8. The FE analysis method was identical to that in Section 2.

According to the designed basis threats demanded by FEMA [16], the suicide vest with 9 kg TNT, as well as compact sedan bombs with 227 kg TNT were assumed as the possible explosives for PC/RC columns. Considering that terrorists can access to columns, the suicide vests were regarded as the contact explosion with the height of waist, i.e., 0.9 m. The compact sedan bomb was usually detonated at the height of seats (0.9 m) near the sidewalk, i.e., 4 m

away from the buildings. Furthermore, the axial compressive ratios of 0.18 and 0.36 were selected. It should be noted that Scenario PC/RC-9-0.18 denotes the explosion of 9 kg TNT on the PC/RC columns with the axial compressive ratio of 0.18.

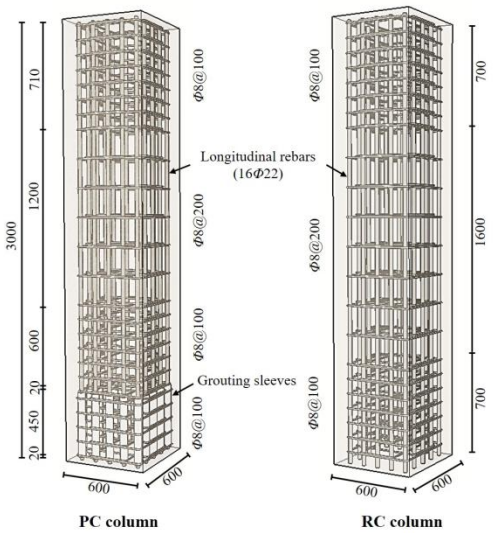


**Figure 7.** Reinforcing details of columns (unit: mm).

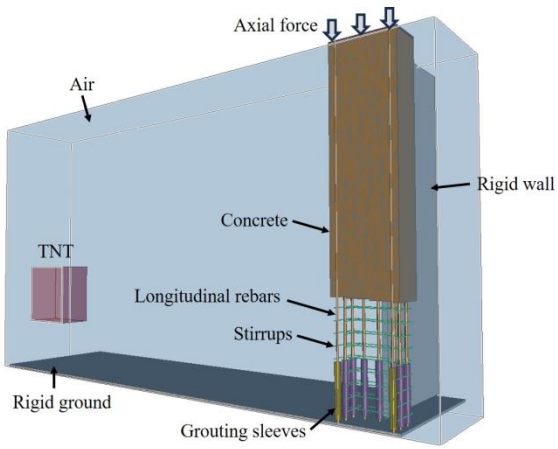


**Figure 8.** 1/2 refined FE model of PC column.

## 3.2. Simulation results and comparisons

Figure 9(a) presents the failure patterns of designed PC/RC columns after the explosion of 9 kg TNT. PC/RC columns are both subjected to the breach failure near the burst height. The rebars are fractured, and the concrete are suffered severe crushing. As a result, the RC/PC columns are unable to endure the contact explosion of 9 kg TNT, and completely lose the load-bearing capacity. Figure 9(b) presents the damage patterns of columns under the explosion of 227 kg TNT. The horizontal cracks at the rear and side faces of both PC/RC columns reflect

the flexural failure at the burst height. In addition, attributed to the grouting sleeves and additional stirrups, the lateral stiffness of PC column is enhanced. Consequently, the shear deformation at the bottom of PC column is relieved in comparison with RC columns.

Furthermore, the residual load-bearing capacities of PC/RC columns are compared, as illustrated in Figure 10. It can be found that the load-bearing capacities of undamaged PC/RC columns are comparable. Under the explosion of 227 kg TNT, the degradation of load-bearing capacities of PC/RC columns exceeds 70% and 84%, respectively. The increases of axial compressive ratio have a certain positive effect on residual properties of PC columns, while not applicable to RC columns. Therefore, the PC columns possess superior blast resistances and residual capacities compared with the identically designed RC columns.

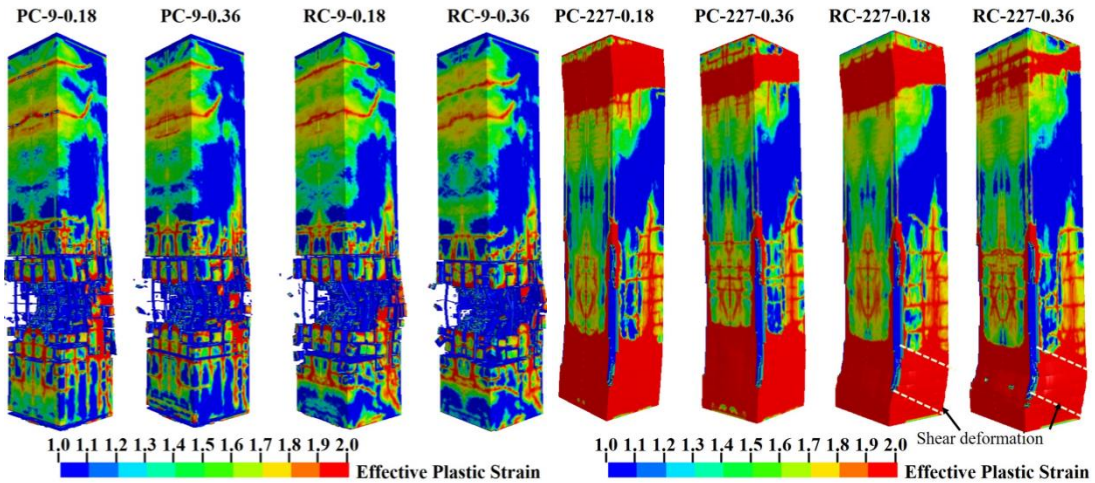


(a) (b)

**Figure 9.** Damage contour of columns under the explosion of (a) 9 kg and (b) 227 kg TNT.

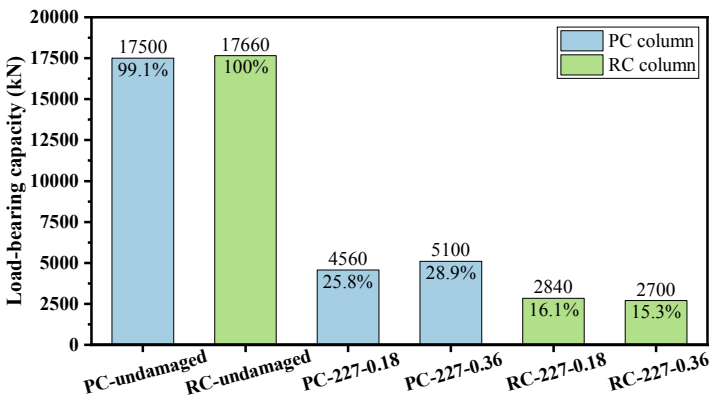


**Figure 10.** Residual load-bearing capacities of columns.

### 3.3. Threat-based design recommendations

To prevent the catastrophic consequence induced by explosions, the practical threat-based design recommendations for buildings are given:

(i) The security check for vehicles should be pay more attention to prevent the side and corner columns from damaged by vehicle bombs (over 227 kg TNT);

(ii) The security inspection for the personnel entering the buildings is necessary to preclude the contact explosion caused by suicide attacks (over 9 kg TNT) on the interior columns;

(iii) Install barriers around buildings to preclude the contact explosion caused by suicide vests on side and corner columns.

## 4. CONCLUSIONS

Based on the explosion test and post-blast axial compressive test conducted by the authors, the reliability of FE analysis method for PC columns under the explosion and axial compressive stages was comprehensively verified, and the blast-resistant analysis of prototype PC and RC columns was performed. The main conclusions are summarized as follows:

(i) Under the explosion of 227 kg TNT, the shear deformation of PC columns is slighter in comparison with RC columns. Besides, the degradation of load-bearing capacities of PC and RC columns exceeds 70% and 84%, respectively. Therefore, PC columns exhibit more excellent blast resistance under close-in explosion.

(ii) Neither PC nor RC columns can sustain load-bearing capacities subjected to the contact explosion induced by suicide vests, i.e., 9 kg of TNT equivalence.

(iii) The practical threat-based design recommendations for PC and RC columns are put forward to prevent the catastrophic consequence induced by vehicle bombs or suicide attacks.

## ACKNOWLEDGMENTS

The project was supported by National Natural Science Foundations of China (52078379, 52308522), China Postdoctoral Science Foundation (023M742663, GZB20230527).

## REFERENCES

[1] Pearson, C. & Delatte, N. (2005). Ronan Point apartment tower collapse and its effect on building codes. *Journal of Performance of Constructed Facilities*, 19(2), 172-177.

[2] Department of Homeland Security. (2011). Reference manual to mitigate potential terrorist attacks against buildings. FEMA 426, Washington, DC.

[3] Williamson, E. B., Bayrak, O., Williams, G. D., Davis, C. E., Marchand, K. A., Mckay, A. E., Wassef, W. & Kulicki, J. (2009). Blast-resistant highway bridges: design and detailing guidelines. National Cooperative Highway Research Program.

[4] Williamson, E. B., Bayrak, O., Davis, C. & Williams, G. D. (2011). Performance of bridge columns subjected to blast loads. I: experimental program. *Journal of Bridge Engineering*, 16(6), 693-702.

[5] Williamson, E. B., Bayrak, O., Davis, C. & Williams, G. D. (2011). Performance of bridge columns subjected to blast loads. II: Results and recommendations. *Journal of Bridge Engineering*, 16(6), 703-710.

[6] Braimah, A. & Siba, F. (2017). Near-field explosion effects on reinforced concrete columns: an experimental investigation. *Canadian Journal of Civil Engineering*.

[7] Chen, L., Hu, Y., Ren, H., Xiang, H., & Fang, Q. (2019). Performances of the RC column under close-in explosion induced by the double-end-initiation explosive cylinder. *International Journal of Impact Engineering*, 132, 103326.

[8] Shi, Y., Hu, Y., Chen, L., Li, Z., & Xiang, H. (2022). Experimental investigation into the close-in blast performance of RC columns with axial loading. *Engineering Structures*, 268, 114688.

[9] Yu, J., Yu, X., Tang, J. & Deng, Y. (2022). Local damage of precast concrete columns with grout sleeve connections under contact detonation. *Engineering Structures*, 265, 114499.

[10] Kyei, C. & Braimah, A. (2017). Effects of transverse reinforcement spacing on the response of reinforced concrete columns subjected to blast loading. *Engineering Structures*, 142, 148-164.

[11] Thai, D. & Kim, S. (2018). Numerical investigation of the damage of RC members subjected to blast loading. *Engineering Failure Analysis*, 92, 350-367.

[12] Lu, J., Wu, H., Cheng, Y. & Chen, G. (2024). Blast resistance of grouting sleeve connected precast concrete columns under close-in explosions. *International Journal of Impact Engineering*, 187, 104908.

[13] Xu, J., Wu, H., Ma, L. & Fang, Q. (2023). Experimental and numerical study on the residual axial capacity of RC bridge piers after contact explosion. *Journal of Bridge Engineering*, 28(6), 1-19.

[14] Ministry of Housing and Urban-Rural Development of the People's Republic of China. (2016). Code for seismic design of buildings, GB 50011-2010. Beijing: China Architecture & Building Press.

[15] Ministry of Housing and Urban-Rural Development of the People's Republic of China. (2014). Technical specification for precast concrete structures, JGJ 1-2014. Beijing: China Architecture & Building Press.

[16] Department of Homeland Security. (2012). Primer to design safe school projects in case of terrorist attacks and school shootings. FEMA-428, Washington, DC.

# EXPERIMENTAL AND NUMERICAL STUDY ON DYNAMIC BEHAVIORS OF PRECAST CONCRETE COMPOSITE SLABS UNDER BLAST LOADING

*Gongqing Chen[1], Hao Wu[2], Jinxian Lyu[3], De Chen[4]*

[1] PhD student, Tongji University, 2110378@tongji.edu.cn.

[2] Professor, Tongji University, wuhaocivil@tongji.edu.cn.

[3] PhD student, Tongji University, 2111022@tongji.edu.cn.

[4] PhD, Tongji University, chende@tongji.edu.cn.

**Corresponding Author: De Chen, PhD.**

College of Civil Engineering, Tongji University, Shanghai, China, 200092

**Email:** chende@tongji.edu.cn

## ABSTRACT

Precast concrete composite (PCC) slabs are widely applied in prefabricated construction due to their advantages of rapid construction, quality control, durability and cost-effectiveness. Terrorist incidents and accidental explosions have increased abruptly, causing huge economic losses and casualties. As the main load-bearing members of structures, the slabs are prone to damage due to larger load surface under blast loading. To examine the dynamic behaviours of the PCC slab, the field blast test under different explosion distances was firstly conducted. The incident and reflected overpressures-time histories, as well as the damage patterns and displacement-time histories of PCC slabs were measured. Then, the explicit dynamic finite element (FE) program LS-DYNA was employed. The reliability of the FE analysis approach was verified by reproducing the responses of PCC slabs. Furthermore, the influence parameters, i.e., strength of concrete of cast-in-place and precast layers, rebar yield strength, interface position, as well as thickness on the blast-resistant performance of the PCC slabs were further discussed. The compressive strength of the concrete and interface position have negligible influence on the dynamic response of PCC slab, while increasing the rebar yield strength and slab thickness can significantly reduce the maximum and residual deflection. Thus, an appropriate increase of slab thickness in structural design can significantly improve the blasting resistance of structures.

***Keywords:*** *Blast Loading, Precast Concrete Composite Slabs, Field Test, Numerical Simulation, Dynamic Behaviours.*

# 1 INTRODUCTION

Environment friendly, energy-saving and emission reduction have become the inevitable trend of current industrial development. Construction industrialization and environmental development require the structure to have the characteristics of excellent structural performance, rapid construction and low-carbon. Prefabricated construction is widely applied and developed due to its advantages of environmental protection and convenient construction. Terrorist incidents and accidental explosions have increased abruptly in recent years, which not only bring huge economic losses, but also cause a large number of casualties. Therefore, the blast-induced catastrophic incidents motivated the urgent need to study the dynamic responses, damage evolution, and blast resistance of building structures. Precast concrete composite (PCC) slabs are the main load-bearing members of the prefabricated structure, which are prone to damage due to larger load surfaces under blast loading. Therefore, it is of great significance to study the dynamic response of PCC slabs under blast loading.

Considerable existing studies have been performed to examine the blast-induced dynamic responses and damage patterns of cast-in-place reinforced concrete (RC) slabs. The PCC slab is composed of precast and cast-in-place layers, and the former part reduces workload and the use of template, and the latter part improves its integrity. Mohamed et al. [1] carried out a series of tests under flexural loading on five prototype semi-precast slabs to evaluate the overall flexural behaviour of slabs, and interface shear and tensile strengths with different surface treatments were examined through experimental and numerical studies. Tian et al. [2] conducted the field explosion test on three PCC slabs under different scaled distances, and the blast resistance was compared with that of RC slabs in terms of the dynamic responses, cracking patterns and damage patterns. It was derived that the maximum vertical deflection of PCC slabs was greater than that of RC slabs, and more cracks emerged and distributed more uniformly of PCC slabs.

Generally, the existing studies still have the following main limitations: the majority of existing work focused on the static mechanical properties [3-5] of PCC slab, e.g., seismic capacity and fire resistance, and there is still a lack adequate studies on dynamic behaviours under blast loadings; The concept “equivalent cast-in-place” of prefabricated construction was commonly adopted in structural design to achieve industrialization. However, the influence of parameter variation on the dynamic response of the PCC slabs needs to be further clarified. Therefore, more studies are needed to investigate the blast resistance of PCC slabs.

To address the above limitations, in this work, experimental and numerical studies on dynamic behaviour of PCC slabs under blast loading were conducted. Firstly, a total of three shots of field blast test on the PCC slabs considering different scaled distances were carried out. Then, the high-fidelity finite element (FE) approach, using Fluid-Structure Interaction (FSI) and multi-material Arbitrary Lagrangian-Eulerian (MM-ALE) algorithms, was adopted to reproduce the explosion tests. Furthermore, based on a validified FE analysis approach, the influence parameters, i.e., concrete strength of cast-in-place and precast layers, rebar yield strength, interface position, as well as thickness on the blast-resistant performance of the PCC slabs were further discussed. The present work can provide helpful references for the blast-resistant design of PCC slabs.

# 2 EXPLOSION TEST AND MODEL VALIDATION

## 2.1 Explosion test

### *2.1.1 Slab specimens*

The geometrical dimensions and the reinforcement details of three PCC slabs are shown in Figure 1, and the length, width and thickness of the slabs are 2400 mm, 1000 mm and 100 mm, respectively. The thickness of both cast-in-place and precast layers was designed to be 50 mm with a concrete cover of 10 mm. The transverse and longitudinal rebars were 10 mm in diameter, and the upper and lower ends of the web reinforcement bars (a diameter of 8 mm) were welded with the rebars of the cast-in-place and the precast layers, respectively. The compressive strength of unconfined cubic concrete in cast-in-place and the precast layer are 54.2MPa and 49.6 MPa, respectively. Besides, the yield strengths of both longitudinal and transverse rebars are 448.8 MPa, and that of steel truss is 420 MPa.

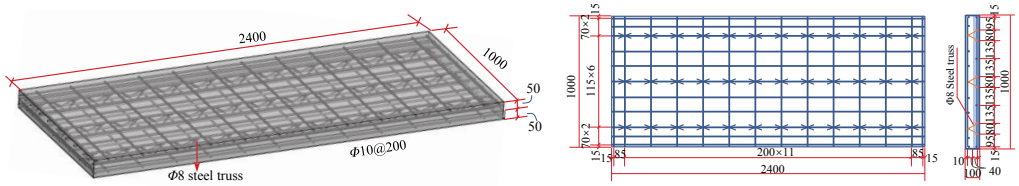


**Figure 1.** Dimensions and reinforcements of PCC slabs (unit: mm)

### *2.1.2 Test setup*

As shown in Figure 2(a), a box-like test apparatus was self-designed to mitigate the influence of blast wave diffraction on the bottom slabs. The simple support constraint boundary condition was realized by the round roller of the upper and lower sealing plates. To examine the blast resistance of the PCC slabs, the field explosion test was conducted on three PCC slabs with the scaled distances of 0.8, 0.6, and 0.4 m/kg$^{1/3}$, corresponding to explosion distances of 1.37 m, 1.07 m and 0.68 m, denoting PCC-0.8, PCC-0.6 and PCC-0.4, respectively. During the test, the explosive was suspended above the slabs using a bamboo frame. The 5kg cuboid TNT explosive charge, with dimensions of 200×150×100 mm, was initiated using a centre point initiation method. To obtain the overpressure-time histories of blast waves, two incident pressure sensors ($P_{i1}$ and $P_{i2}$) were arranged at 3995 mm, and the height consistent with that of the explosive centre. Three reflected overpressure sensors $P_{r1}$, $P_{r2}$, and $P_{r3}$ were arranged aside from the test box to prevent a potential breakdown during the test. In addition, four linear variable displacement sensors ($D_1$-$D_4$) were installed at the bottom face of slabs to record the dynamic responses of the PCC slab. The sensors $D_1$ and $D_4$ were located at the mid-span of the PCC slab bottom face, and the sensors $D_2$ and $D_3$ were located at 1/4 and 3/4 spans of the specimen which are both 500 mm away from $D_1$.

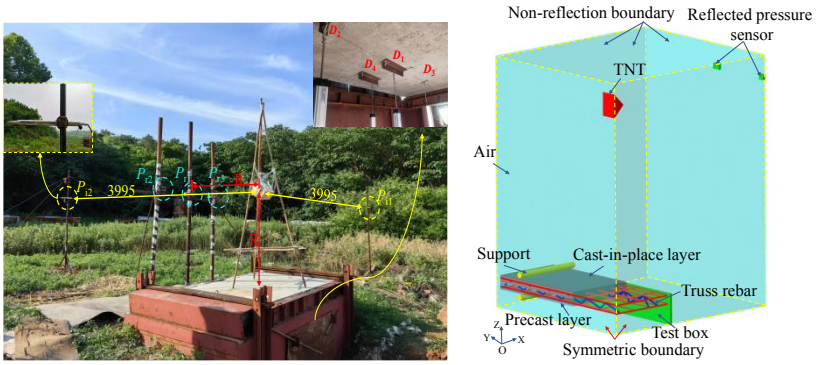


(a) (b)

**Figure 2.** Test setup (a) photograph (b) 1/4 FE model (unit: mm)

## 2.2 Model validation

Numerical simulation has become an effective approach for blast-resistant analyses due to its convenient operation and economy, and plays a good complementary role in experimental study. In this section, the explosion tests were reproduced to validate the feasibility and applicability of the FE model and analysis approach.

### *2.2.1 FE analysis method*

The 1/4 symmetric FE model was established to improve computational efficiency, as shown in Figure 2(b). The propagation of the blast wave and its instantaneous interactions with PCC slabs were simulated using the fluid-structure interaction (FSI) and multi-material arbitrary Lagrangian-Eulerian (MM-ALE) algorithms available in LS-DYNA [6]. Eight-node hexahedral single-point integration solid elements (*SECTION_SOLID/ELFORM=1) were used to discretize the concrete slab, steel supports and test box. Rebars were modelled using Hughes-Liu beam elements with cross-section integration (*SECTION_BEAM/ELFORM=1). The air and TNT domains were modelled using MM-ALE solid elements with one integration point (*SECTION_SOLID_ALE/ELFORM=11). The element sizes adopted for all components were determined through a sensitivity study involving trial simulations and comparison to experimental data. The PCC slab, steel supports and test box elements were all 10 mm. and those of air and TNT were determined as 30 mm and 15 mm, respectively. FSI between the rebars and concrete, as well as between the blast waves and slabs, are modelled using the keyword *CONSTRAINED_LAGRANGE_IN_SOLID. The interface between precast and cast-in-place concrete employed the keywords *CONTACT_AUTOMATIC_SURFACE_TO_SURFACE_TIEBREAK(OPTION=2), in which the static and dynamic friction coefficients were both adopted as of 1 [7].

### *2.2.2 Comparisons and discussions*

The comparisons of the experimental and simulated reflected overpressure-time histories are shown in Figure 3. It can be drawn that, the predicted reflected overpressure-time histories exhibit good agreement with the test data, and the corresponding deviations of peak overpressure are less than 30%. Considering the influence of a complex propagation environment, the predicted results are considered to agree well with the measured data.

Furthermore, Figure 4 shows the comparisons of deflection-time histories of PCC slab, the deviations of the predicted maximum deflections compared with the test data are both within 25%. Besides, Figure 5 shows the post-blast damage contours of PCC slabs. Both the experimental and predicted damage patterns indicate that all the test slabs exhibit a typical flexure failure mode under blast loadings. For the damage on the top and bottom face of slabs, the predicted crack distributions are basically consistent with the experimental observations. Therefore, the proposed FE analyses approach is reliable, and the corresponding element types, material model and parameters, as well as the numerical algorithms can be further utilized to influence the parameters on the dynamic behaviors of PCC slabs under blast loadings.

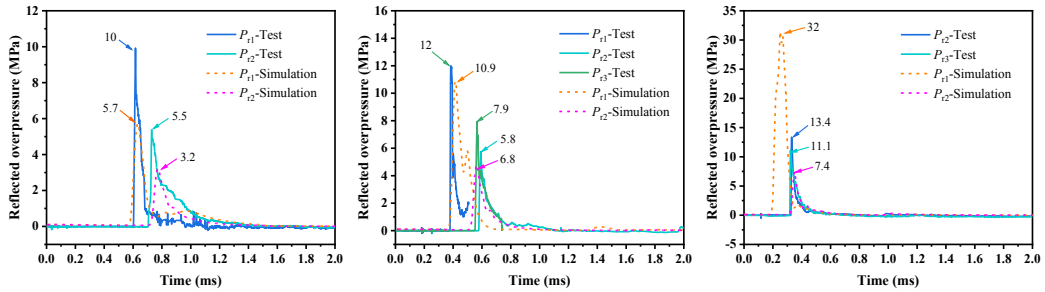


(a) (b) (c)

**Figure 3** Reflected overpressure-time histories in Scenarios (a) PCC-0.8 (b) PCC-0.6 (c) PCC-0.4

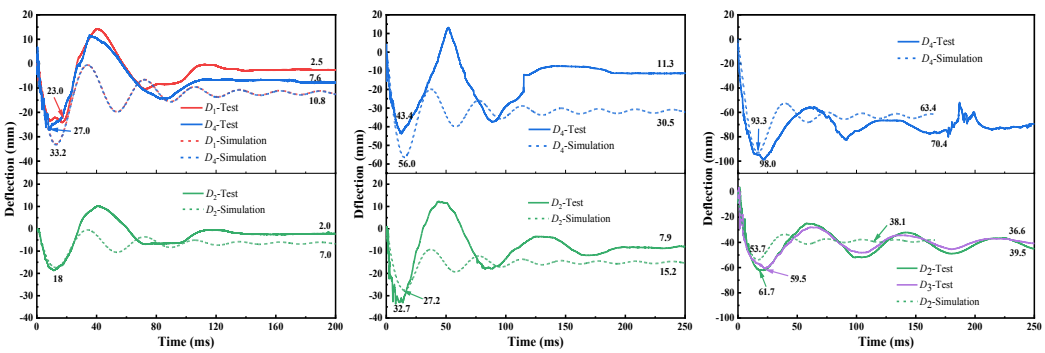


(a) (b) (c)

**Figure 4** Deflection-time histories in Scenarios (a) PCC-0.8 (b) PCC-0.6 (c) PCC-0.4

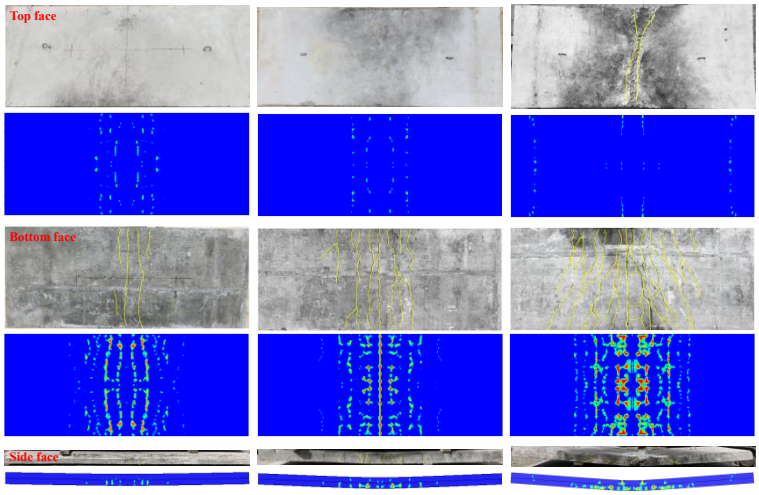


(a) (b) (c)

**Figure 5** Damage patterns of post-blast (a) PCC-0.8 (b) PCC-0.6 (c) PCC-0.4 slabs

# 3 PARAMETRIC STUDY

In this section, the validated FE model in Section 2.2 was utilized to examine parameters influence the blast resistance of PCC slabs. A baseline Scenario was first established, where the PCC slab thickness is 100 mm with 50 mm precast and cast-in-place layers, and the concrete compressive strengths are respectively 40 MPa and 50 MPa, and the yield strength of rebar is 400 MPa. The TNT equivalent charge is 5 kg, and the explosion distance is set as 1.37 m. The PCC slab geometry, reinforcement configuration, boundary conditions, and explosive threat were consistent with experimental test conditions. Then, parametric studies were further discussed by systematically varying key parameters in the model to analyse their influence on the dynamic response of the PCC slab under blast loading.

## 3.1 Concrete strength

To examine the influence of concrete compressive strength on the blast resistance of PCC slabs, a series of simulations was conducted utilizing the baseline slab model. The concrete compressive strength in both the cast-in-place and precast layers was systematically varied between 30-70 MPa, e.g., cast-in-place and precast layers are 40 MPa and 50 MPa, recorded as C40-C50, and other design parameters were consistent with those adopted in above baseline Scenario.

Figure 6 shows the mid-span deflection-time histories and maximum deflection of PCC slabs under different concrete compressive strengths. It can be observed that maintaining the precast layer strength at 40 MPa, while increasing the cast-in-place layer strength from 30 to 70 MPa, resulted in a 9.6% reduction in maximum deflection, i.e., from 31.3 mm to 28.3 mm. Conversely, when the cast-in-place layer strength was held constant, increasing the precast layer strength from 30 to 70 MPa decreased the maximum deflection by 13.0%, i.e., from 31.5 mm to 27.4 mm. The findings suggest that increasing the concrete compressive strengths of both the precast and cast-in-place concrete can marginally improve the blast resistance of PCC

slabs, which is mainly attributed to the enhancements of the mid-span bending capacity. Notably, As illustrated in Figure 7(b), enhancing the precast layer strength has a more pronounced influence on reducing maximum deflection. In summary, the results indicate that compressive strengths modestly enhance the blast resistance of PCC slabs, and strengthening the precast layer exhibits a better effect.

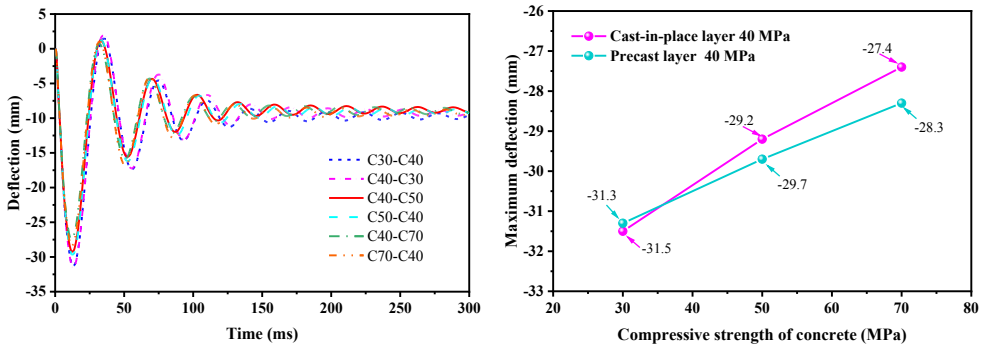


(a) (b)

**Figure 6** Under different concrete compressive strength (a) deflection-time histories (b) maximum deflection

## 3.2 Rebar strength

To investigate the impact of rebar yield strength on the blast resistance of PCC slabs, rebar yield strengths ranging from 235 MPa to 600 MPa were considered. As depicted in Figure 7, at a rebar yield strength of 235 MPa, the maximum and residual deflections were 34.9 mm and 20.5 mm, respectively. When the rebar strength is improved to 600 MPa, the maximum deflection (28.5 mm) and residual deflection (5.9 mm) were notably reduced by 18.3% and 71.2%, respectively. The results revealed that improved rebar yield strength effectively reduced the maximum deflection of the PCC slab under blast loading. In summary, as demonstrated by the notably reduced residual deflections, the resilience of the PCC slab was effectively by increased yield strength, thereby improving the blast resistance of the PCC slab.

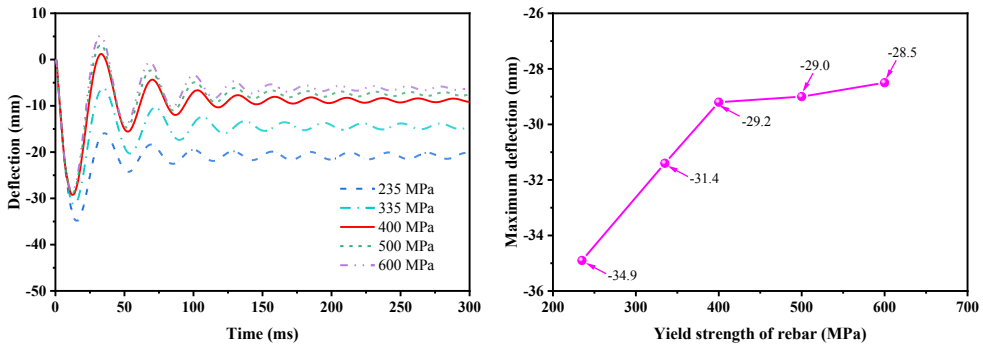


(a) (b)

**Figure 7** Under different yield strength (a) deflection-time histories (b) maximum deflection

## 3.3 Interface position

For a total thickness of 100 mm, five interface configurations were analysed by varying the thickness of the precast and cast-in-place layers: 30-70 mm, 40-60 mm, 50-50 mm, 60-40 mm, and 70-30 mm. As shown in Figure 8, the maximum deflections were observed to be 29.5 mm, 29.6 mm, 29.2 mm, 29.6 mm, and 29.9 mm, respectively. The deflection-time histories were nearly identical, indicating negligible influence of interface position on the flexural response of PCC slabs. This insensitivity to interface position can be attributed to the reliable connection between the precast and cast-in-place layers. Furthermore, the shear stresses are transferred uniformly in the interface, and the attenuation of the blast wave penetrating the PCC slab appears unaffected by where the interface is located. Consequently, provided the connection quality meets the required standards, PCC slabs can achieve consistent blast resistance performance regardless of precast-cast configuration.

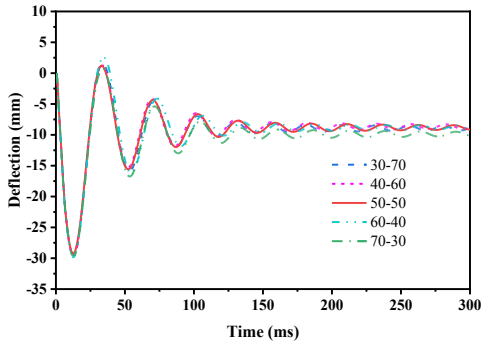


**Figure 8** Deflection-time histories of different interface positions

## 3.4 Thickness of slab

To study the influences of slab thickness on blast resistance, three total thicknesses of PCC slab were considered: 80 mm, 100 mm and 120 mm, and the slab was divided evenly into precast and cast-in-place layers, with consistent concrete cover thickness. As shown in Figure 9, increasing the PCC slab thickness from 80 mm to 140 mm resulted in a substantial reduction in the maximum deflection, which decreased from 50.1 mm to 13.2 mm, representing a 73.7% decrease. These results demonstrate that slab thickness has a significant influence on dynamic response under blast loading. Thus, an appropriate increase of slab thickness in structural design can significantly improve the blasting resistance of structures.

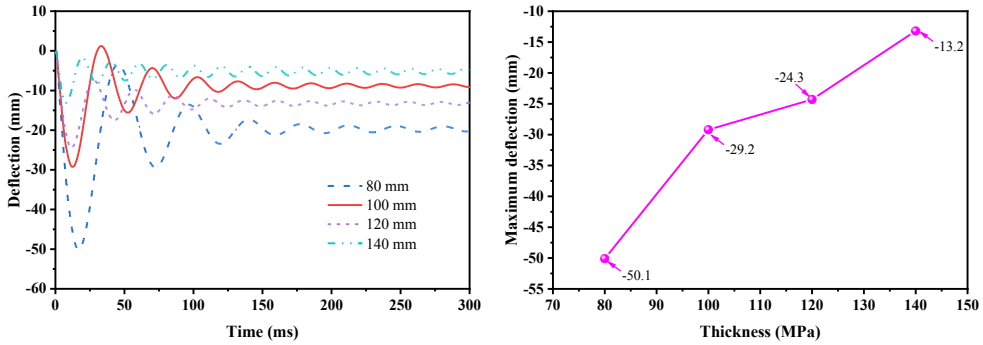


(a) (b)

**Figure 9** Under different slab thicknesses (a) deflection-time histories (b) maximum deflection

# 4 CONCLUSIONS

Based on the field explosion test and the high-fidelity numerical simulation, the parametric influences on blast resistance of PCC slab are further discussed, and the dynamic responses of PC slabs are systematically evaluated. The main conclusions are summarized as follows:

(i) The field explosion test was conducted on three PCC slabs with three identical scaled distances. Both PCC slabs exhibited global flexural failure under scaled distances ranging from 0.4-0.8 m/kg$^{1/3}$, and the deflections and damage of the PCC slab increased as the scaled distances of explosives decreased.

(ii) By comparing with the experimental overpressures and deflections of slabs, the proposed FE analysis approach for predicting the dynamic behaviors of the PCC is comprehensively validated.

(iii) The parametric influences on blast resistance of PCC slab are further discussed. The compressive strength of the concrete and interface position have negligible influence on the dynamic response of the PCC slab, while increasing the rebar yield strength and slab thickness can significantly reduce the maximum and residual deflection. Besides, an appropriate increase of slab thickness in structural design can significantly improve the blasting resistance of structures.

# ACKNOWLEDGMENTS

The authors acknowledge research grant from the National Natural Science Foundation of China (Nos. 52078379, 52308522), China Postdoctoral Science Foundation (023M742663, GZB20230527).

# REFERENCES

[1] Mohamed, M. S., Thamboo, J. A., & Jeyakaran, T. (2020). Experimental and numerical assessment of the flexural behaviour of semi-precast-reinforced concrete slabs. *Advances in structural engineering*, 23(9), 1865-1879.

[2] Tian, S., Yan, Q., Du, X., Chen, F., & Zhang, B. (2023). Experimental and numerical studies on the dynamic response of precast concrete slabs under blast load. *Journal of Building Engineering*, 70, 106425.

[3] Deng, B. Y., Tan, D., Li, L. Z., Zhang, Z., Cai, Z. W., & Yu, K. Q. (2023). Flexural behavior of precast ultra-lightweight ECC-concrete composite slab with lattice girders. *Engineering Structures*, 279, 115553.

[4] Liu, Y. L., Huang, J. Q., Chong, X., & Ye, X. G. (2021). Experimental investigation on flexural performance of semi‐precast reinforced concrete one‐way slab with joint. *Structural Concrete*, 22(4), 2243-2257.

[5] Kanchanadevi, A. K., Ramanjaneyulu, K., & Srinivas, V. (2021). Behaviour of concrete composite slabs with truss type shear connectors of different orientation angle. *Advances in Structural Engineering*, 24(13), 3070-3084.

[6] Hallquist J.O. (2007). LS-DYNA Keyword User's Manual, Livermore Software Technology Corporation, 970.

[7] ACI318. (2005). Building code requirements for structural concrete (ACI 318-05) and commentary (ACI 318R-05). Farmington Hills, Mich.

# AN INSIGHT INTO THE BLAST-INDUCED COLLAPSE OF SIMPLY-SUPPORTED HIGHWAY BRIDGES

*Liangliang Ma[1], Hao Wu[2]*

[1] Doctoral Student, Tongji University, maliangliang0521@163.com.

[2] Professor, Tongji University, wuhaocivil@tongji.edu.cn.

**Corresponding Author: Hao Wu, Prof.**

No. 1239 Siping Road, Shanghai, China, 200092

**Email:** wuhaocivil@tongji.edu.cn

## ABSTRACT

To deepen the understanding of the collapse of simply-supported highway bridges, the shear force distribution-based and stability theory-based analysis methods for bridge collapse were proposed. The finite element approach (FEA) was adopted and validated against the explosion test on RC piers through comparisons with experimental reflected overpressure-time histories and the pier damage patterns. Then, based on the validated FEA, the FE model of a prototype highway bridge was established, and explosion sources were determined as the sedan bomb specified by Federal Emergency Management Agency (FEMA). By varying the standoff distances, the explosion analyses were carried out, and the collapse response of the prototype highway bridge was examined from the both shear force distribution and stability theory perspectives. Finally, a safe standoff distance for the prototype bridge under sedan bomb explosion was determined. This work can improve the understanding of bridge collapse, and help city planners properly set standoff barriers.

***Keywords:*** *Blast-induced, Bridge collapse, Numerical simulation, Standoff distance, Analysis method.*

# INTRODUCTION

Bridge structures are key components of transportation lifeline projects and vulnerable to terrorist attacks and accidental explosions in peacetime, as well as military assault in wartime. However, China has not yet published design specifications for bridge structures and their protection against explosions. Therefore, the research on explosion damage mechanism and safety protection technology of bridge structures is of great theoretical significance and practical engineering value to improve the existing design concept and enhance the safety and disaster prevention capability of transportation infrastructure.

In existing studies, most of them focus on the damage and responses of bridge components instead of the entire bridges. For example, Bruneau [1, 2], Williams [3-6], and Zong et al. [7, 8] all carried out field explosion tests on reduced-scale bridge piers to evaluate their blast-resistant performance. Foglar and Kovar [9-11] experimentally compared different countermeasures against blast load. A consensus was reached that the increasing the standoff distance is the most effective way to protect the bridge structures from blast-induced collapse. However, since the above-derived conclusion is based on single bridge component without considering the entire bridge, the understanding of the influence of standoff distances on the bridge collapse, is not enough.

To address this limitation, this paper aims to improve the blast-induced bridge collapse from both shear force distribution and stability theory perspectives. The finite element approach (FEA) was adopted and validated against the explosion test on RC piers [8] through comparisons with experimental reflected overpressure-time histories and the pier damage patterns. Then, the FE model of a prototype highway bridge was established, and explosion sources were determined as the sedan bomb specified by FEMA (Federal Emergency Management Agency) [12]. By varying the standoff distances, the explosion analyses were carried out to examine the collapse response of the prototype highway bridge from both shear force distribution and stability theory perspectives. This work can improve the understanding of bridge collapse, and help city planners properly set standoff barriers.

# FE MODELS AND VALIDATIONS

The FE model was established and solved by the explicit dynamic analysis codes LS-DYNA [13]. For numerical simulations, to obtain the reliable results, it is of great significance to select the element types and their mesh sizes, material models and their parameters, as well as contact algorithms and corresponding parameters. Therefore, at present, these FE related parameters are determined through comparisons with field explosion tests, which will be discussed as follows.

## Element types and sizes

A highway bridge is composed of bridge spans, bents, piers, abutments and piles which are most made of concrete and steel. For the element types of the bridge, the concrete, reinforcing steel and steel slab are discretized by the solid, beam and shell elements, respectively.

As for element sizes, the mesh sizes of the bridge components are determined through comparisons with experimental failure modes of piers, while the mesh sizes of the TNT-air are trialed by comparing with the experimental reflected overpressure-time histories, which will be illustrated in detail in Section "Validations". Table 1 lists the mesh sizes of the bridge components and the TNT-air. It is noteworthy that the range of the refined region with 10-mm mesh size is from the pier bottom to the height of 650 mm.

**Table 1.** Mesh Sizes of FE Models

| Part | Support | Pier | Bent | Air | Rubber base |
|---|---|---|---|---|---|
| Size (mm) | 50 | 36 | 40 | 40 | 5 |
| Part | Rebar | Girder | Deck | Anchorage | TNT |
| Size (mm) | 10 | | | 20 | |

## Material models

Concerning the bridge part, the material models in LS-DYNA [13] for the concrete, steel and rubber are *MAT_072R3, *MAT_003 and *MAT_006, respectively. Besides, the strain rate effect is considered through introducing the dynamic increase factor (*DIF*) of the material strength, i.e., the ratio of the dynamic strength to the static strength. The *DIF* defined in CEB-FIP MODEL CODE [14] is adopted for concrete while the Cowper-Symonds (CS) model [13] is used to consider the *DIF* for the steel. Furthermore, the keyword *MAT_ADD_EROSION was utilized to delete the over distorted structural elements, and describe the failure pattern. At present, the maximum principal strain-based erosion criterion is adopted and taken as 0.04 and 0.5 for contact and non-contact explosion scenarios, respectively [15].

The material models of TNT and air in LS-DYNA are *MAT_008 combined with *EOS_002 (Eq. (1)), and *MAT_009 combined with *EOS_001 (Eq. (2)), respectively. The adopted material models and corresponding parameters can refer to our previous work [15].

$$P = A(1-\frac{\omega}{R_1 V})e^{-R_1 V} + B(1-\frac{\omega}{R_2 V})e^{-R_2 V} + \frac{\omega E}{V} \tag{1}$$

where $P$ is the detonation pressure, $V$ is the relative volume, $E$ is the initial unit volume energy, and the coefficients $A, B, R_1, R_2, \omega$ are determined experimentally.

$$P = C_0 + C_1\mu + C_2\mu^2 + C_3\mu^3 + (C_4 + C_5\mu + C_6\mu^2)E \tag{2a}$$

$$\mu = \frac{1}{V} - 1 \tag{2b}$$

where $P$ is the pressure value, $E$ is the initial specific internal energy, and $V$ is the relative volume. When the linear polynomial equation of state is used for air, it is preferable to

$\gamma = C_p / C_v$, $C_0 = C_1 = C_2 = C_3 = C_6 = 0$, $C_0 = C_1 = C_2 = C_3 = C_6 = 0$, in which $C_P, C_v, \gamma$ are the heat capacity at constant pressure, the heat capacity at constant volume and the adiabatic index of the gas, respectively.

## Contact and boundary algorithms

For the contact algorithms, sharing nodes method is adopted to constrain the mesh nodes with the same material, while for interaction between the rebars and the concrete, Fluid-Solid Interaction (FSI) algorithm realized by the keyword *CONSTRAINED_LAGRANGE_IN_SOLID is adopted. Besides, the FSI algorithm is also applied to the interaction between blast wave and the bridge structure. Last but not the least, contacts between different bridge parts, e.g., the bent and rubber base, is simulated through keyword *CONTACT_AUTOMATIC_SURFACE_TO_SURFACE. It is noteworthy that the parameters of contact algorithms are default and recommended by the LS-DYNA user's manual [13].

Concerning the boundary algorithms, by referring to the actual boundary conditions, the keyword *BOUNDARY_SPC_SET is utilized to constrain both the rotational and translational degrees of freedom at the pile bottom. Considering that in the real world, the air domain is infinite, the keyword *BOUNDARY_NON_REFLECTING is used to let the blast wave flow out. Besides, the keyword *RIGIDWALL_PLANAR is adopted to create the assumed rigid ground.

## Validations

The abovementioned FEA will be validated from two aspects, i.e., blast load and pier damage pattern, against the explosion tests on RC piers [8]. Tang [8] carried out these tests to study the characteristics of dynamic responses of piers under both non-contact and contact explosions, and explore the influences of the cross-section types, slenderness ratios, concrete types, stirrup types, etc., on the blast-resistant performance of bridge piers. Precisely, for non-contact explosion scenarios, three TNT charge weights (0.4 kg, 1.0 kg and 2.0 kg) with 1.5-m standoff distance are selected; while for contact explosion scenarios, the TNT charge weights are constant as 1.0 kg.

The test setup and the FE model are presented in Fig. 1. The height of the pier is 3700 mm, and the pier diameter is 400 mm. The rebar diameter is 12 mm and the corresponding yield strength is 400 MPa. The concrete compressive strength is 40 MPa. Besides, the reflected overpressure sensors are spaced at a distance of 1000 mm at the blast front surface of the pier. More information about the test can refer to Ref. [8].

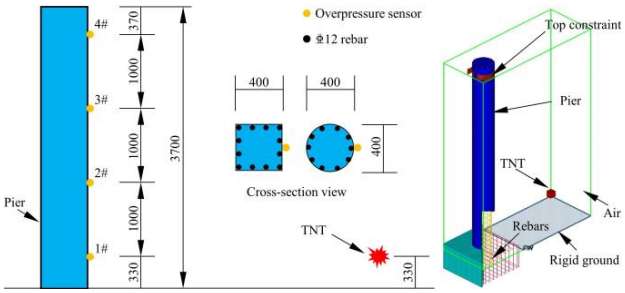


**Figure 1.** Test setup and FE model

Two explosion scenarios are selected to validate the FEA, as listed in Table 2. The non-contact explosion scenario is mainly used to validate the mesh sizes of the air and TNT, while the contact explosion scenario aims to verify the adopted erosion criteria.

**Table 2.** Detailed test information for model validation

| Explosion type | No. | Standoff distance | TNT charge |
|---|---|---|---|
| Non-contact | - | 1.5 m | 1.0 kg |
| Contact | S1 | - | 1.0 kg |

Fig. 2 presents the comparisons of the predicted and experimental reflected overpressure-time histories of mearing points 1# and 2# in Fig. 1. It can be found that both the peak reflected overpressure and the duration of the positive phase are in a good agreement with the test data. Therefore, it is considered that the adopted mesh sizes of the air and TNT, the material models and corresponding parameters, and the FSI algorithms are reliable, and can be adopted for the following analyses.

The damage mechanism of piers under contact explosions is studied through plotting the damage contours and comparing with the post-explosion photos, as shown in Fig. 3. It can be found that compared with the test photos, the pier experiences identical failure patterns, i.e., cracks far away from the detonation, concrete spalling at the rear surface and rebars disclosed at the front surface. Besides, the deviation between the predicted and experimental spalling heights is less than 10%, which indicates that the pier mesh sizes, material models, erosion criteria, and the FSI algorithms are reliable and can be used in the following analyses.

To conclude, the abovementioned FEA has been fully validated from both the blast load and the damage patterns of pier, and can be adopted in the subsequent analyses.

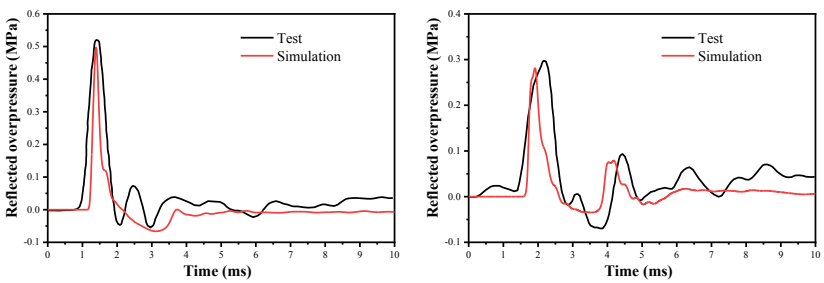

**Figure 2.** Comparisons with the experimental reflected overpressure-time histories at measuring point (a) 1# (b) 2#

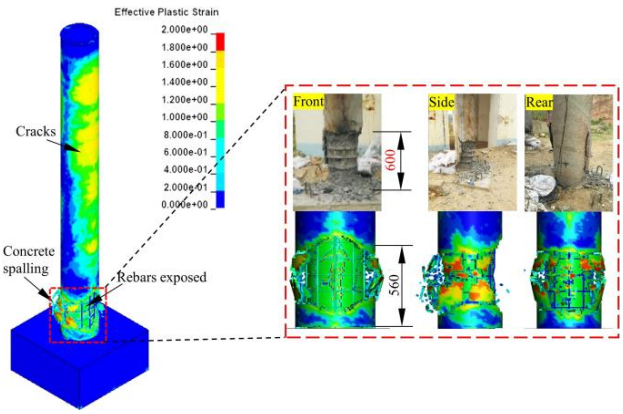


**Figure 3.** Damage contours of the blast loaded pier

# PROTOTYPE RC HIGHWAY BRIDGE UNDER BELOW-DECK EXPLOSIONS

Based on the above-validated FEA, the FE model of a prototype highway bridge was established, and explosion scenarios were determined. Finally, the corresponding explosion analyses were carried out to examine the collapse response and mechanism.

## FE model

The prototype RC highway bridge is 30 m long and 10.5 m wide, with 8.54-m high piers spaced at a distance of 6.1 m, as shown in Fig. 4. Concerning the material properties, the concrete compressive strength is 40 MPa and the reinforcing steel strength is 400 MPa. To balance the computing efficiency and prediction accuracy, the FEA is kept identical to that of the validated one, except that for structural regions far away from the detonation point, larger mesh sizes are adopted as 100 mm to reduce the computational cost. Additionally, the interaction between the soil and the pile is considered by FSI algorithms, and *MAT_014 material in LS-DYNA is used to describe the soil behavior.

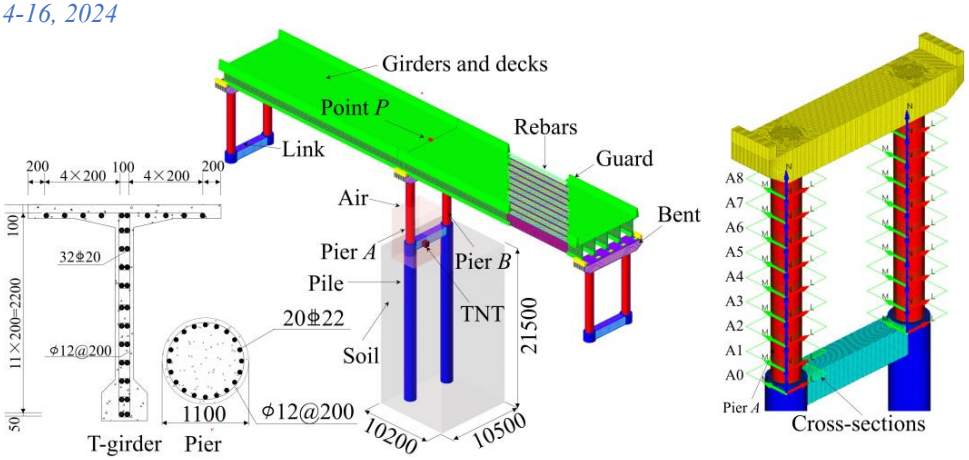


**Figure 4.** FE model of the prototype bridge

## Explosion scenarios

Since the prototype highway bridge has been established, for explosion analyses, TNT charge weights and locations are the remaining items that need to be determined rigorously. According to statistics [16], before 2015, one of every five cars sold was a sedan, revealing a tremendous number of sedans. Additionally, FEMA [12] specifies sedan bomb as one of the design basis threats. As a result, at present, the sedan bomb threat is adopted as the explosion source and its equivalent TNT charge weight is 545 kg [12]. Considering that the dimension of a sedan is approximately 4.0 m in length, 1.8 m in width and 1.4 m in height, thus the smallest standoff distance and burst height can be roughly determined as 1.4 m and 0.7 m, respectively. By varying the standoff distances from 1.4 m to 2.5 m at a step of 0.1 m, total 12 explosion scenarios are set, and the following nomenclature is adopted. S-1.4 denotes that the pier is blast loaded by 1.4-m standoff distance sedan bomb.

# RESULTS AND DISCUSSIONS

The explosion analyses were carried out on a personal computer with 8-core-16-thread Intel 8700k CPU, 36-GB-RAM, and for one explosion scenario, 240 clock hours are needed. After completing the explosion analyses, the iso-damage concours of the blast loaded bridge, shear forces at pier cross-sections, and the vertical responses of point P in Fig. 4 are output for discussions herein.

## Results

The iso-damage concours of the blast loaded bridge are plotted to directly judge whether the blast load renders the bridge with collapse, and find out the critical safe standoff distance for the prototype bridge subjected to the sedan bomb explosion, as shown in Fig. 5. It can be concluded that the critical safe standoff distance is 2.3 m, i.e., under sedan bomb explosion, if the standoff distance is less than 2.3 m, the prototype bridge will definitely collapse.

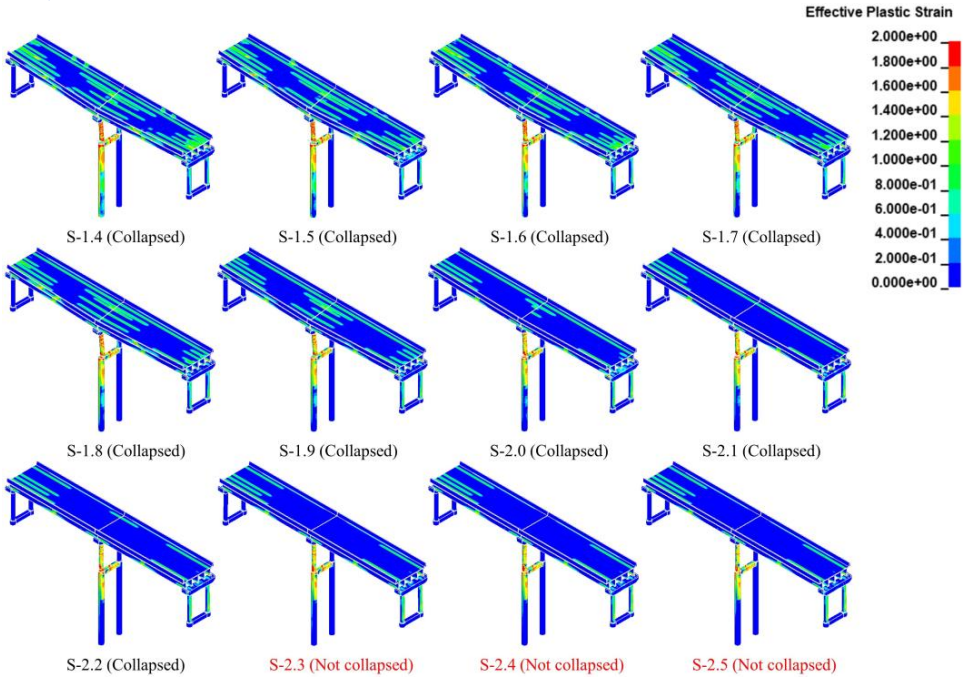


**Figure 5.** Iso-damage contours of the prototype bridge

## Discussion I: Shear force distribution-based perspective

The peak shear forces at cross-section of pier *A* are plotted against the cross-section height normalized by the pier height. Assuming that once a pier experiences shear failure, the entire bridge will collapse. Based on this assumption, by comparing the peak shear force with the allowable value, the bridge collapse can be judged. It should be noted that the cross-sectional shear force can be regarded as direct shear force, and Krauthammer et al. [17-19] has done much work on the direct shear resistance in in a unified piecewise linear form, as shown in Fig. 6. At present, the allowable direct shear force with unit of N is concerned, and it is derived by maximum direct shear stress multiplied by the pier cross-sectional area, as illustrated in Eq. (7), which has taken into account the strain rate effect.

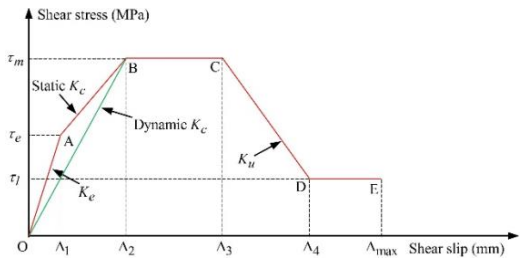


**Figure 6.** Direct shear resistance [19]

$$V_{s,allowable} = \pi D^2 (1.40\sqrt{f_c'} + 0.98\rho_{sv} f_y)/4 \tag{3}$$

where $D$ is the pier diameter (mm), $f'$ is the concrete compressive strength (MPa), $\rho_{sv}$ is the longitudinal reinforcement ratio, and $f_y$ is the yield strength of the reinforcing steel (MPa).

Fig. 7 presents the comparisons of predicted shear force distribution along the pier height and the allowable shear force. With the standoff distance decreasing, the cross-sectional shear force increases, gradually exceeding the allowable cross-sectional shear force. It can be judged that herein the critical safe standoff distance is 2.1 m, which deviates from that obtained by iso-damage contours. The reason may be attributed to the overestimate of the allowable shear force. For explosion scenarios with standoff distance less than 2.1 m, direct shear failure will occur for Scenario S-2.0, which was also observed by field explosion tests [2], as shown in Fig. 8.

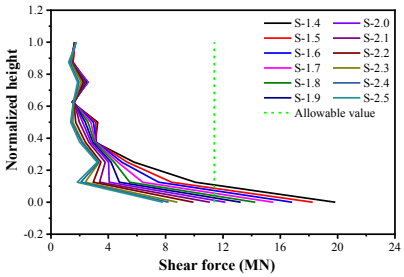


**Figure 7.** Comparisons with the allowable shear force

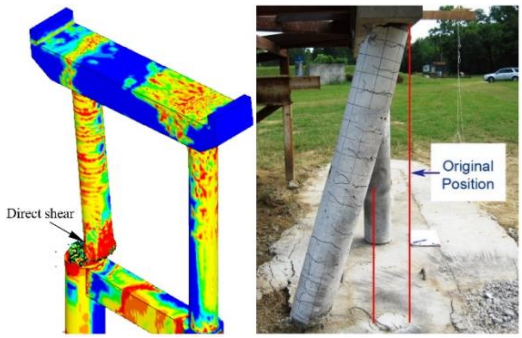


**Figure 8.** Direct shear failure

## Discussion II: Stability theory based-perspective

From a stability theory perspective, the bridge collapse is an unstable state, while the bridge without collapse is a stable state. A common way to judge whether a system is stable is to plot the phase portrait, i.e., the general location against the general momentum [20]. At present, the vertical displacement and the velocity of point *P* are output for stability analyses. Fig. 9 presents the phase portraits of Scenarios S-2.2 and S-2.3. It can be found that the system of Scenario S-2.2 is unstable since the velocity-displacement curve is diverging. While for Scenario S-2.3, the velocity-displacement curve is converging, and it indicates that the corresponding system is stable. Therefore, the critical safe standoff distance is determined as 2.3 m, which is identical to the iso-damage contour-based results.

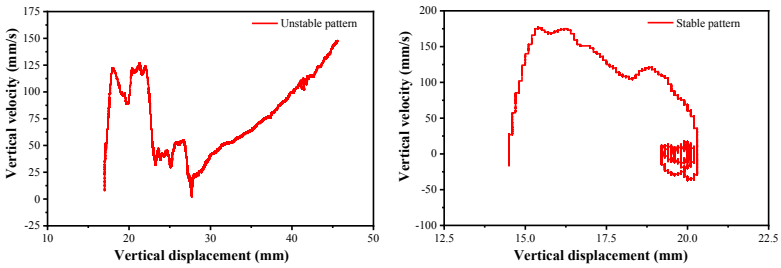


(a) (b)

**Figure 9.** Phase portraits of Scenarios (a) S-2.2 (b) S-2.3

# CONCLUSIONS

To deepen the understanding of the blast-induced collapse of simply-supported highway bridges, the shear force distribution-based and stability theory-based analysis methods for bridge collapse are proposed. The main findings and conclusions are:

(i) The critical safe standoff distance determined as 2.3 m for the prototype bridge under sedan bomb explosion.

(ii) The blast-induced collapse of highway bridges is attributed the direct shear failure of the pier.

(iii) Compared with the shear force distribution-based collapse analysis method, the stability theory-based method can yield a relatively conservative result, which can help the city planners properly set standoff barriers.

## ACKNOWLEDGMENTS

This work is supported by National Natural Science Foundations of China (Grant No. 52078379).

## REFERENCES

[1] S Fujikura, M Bruneau. (2011). Experimental investigation of seismically resistant bridge piers under blast loading. *Journal of Bridge Engineering*, 16(1), 63-71.

[2] S Fujikura, M Bruneau. (2008). *Experimental and analytical investigation of blast performance of seismically resistant bridge piers*. Buffalo: University at Buffalo, State University of New York.

[3] E B Williamson, O Bayrak, C Davis, et al. (2011) Performance of Bridge Columns Subjected to Blast Loads. I: Experimental Program. *Journal of Bridge Engineering*, 16(6), 693-702.

[4] E B Williamson, O Bayrak, C Davis, et al. (2011). Performance of Bridge Columns Subjected to Blast Loads. II: Results and Recommendations. *Journal of Bridge Engineering*, 16(6), 703-711.

[5] G D Williams, E B Williamson. (2011). Response of Reinforced Concrete Bridge Columns Subjected to Blast Loads. *Journal of Bridge Engineering*, 137(9), 903-913.

[6] G D Williams, E B Williamson. (2012). Procedure for Predicting Blast Loads Acting on Bridge Columns. *Journal of Bridge Engineering*, 17(3), 490-499.

[7] Z Zong, B Tang, C Gao, et al. (2017). Experiment on Blast-resistance Performance of Reinforced Concrete Piers." *China Journal of Highway and Transport*, 9(30).

[8] B Tang. *Experimental investigation of reinforced concrete bridge piers under blast loading*. (2016). Master thesis, Nanjing: Southeast University. (in Chinese)

[9] M Foglar, M Kovar. (2013). Conclusions from experimental testing of blast resistance of FRC and RC bridge decks. *International Journal of Impact Engineering*, 59, 18-28.

[10] R Hajek, J Fladr, J Pachman, et al. (2018). An experimental evaluation of the blast resistance of heterogeneous concrete-based composite bridge decks. *Engineering Structures*, 179, 204-210.

[11] R Hajek, K Horníkova, M Foglar. (2020). Numerical assessment of the response of a heterogeneous concrete-based composite bridge deck to a near field explosion. *Engineering Structures*, 2020, 225.

[12] Department of Homeland Security, Science and Technology Directorate, Infrastructure Protection and Disaster Management Division. (2012). *Primer to Design Safe School Projects in Case of Terrorist Attacks and School Shootings*. Buildings and Infrastructure Protection Series, 2012, 1.

[13] J O Hallquist. (2007). *LS-DYNA keyword user's manual*. Livermore Software Technology Corporation, 2007, 970.

[14] Euro-International Committee for Concrete. (1990). *CEB-FIP MODEL CODE 1990*.

[15] L L Ma, H Wu, Q Fang. (2021). Damage mode and dynamic response of RC girder bridge under explosions. *Engineering Structures*, 243, 112676.

[16] Ulrich Lawrence. (2019). S.U.V. vs. Sedan, and Detroit vs. the World, in a Fight for the Future. *The New York Times*. 2019.9.12. https://www.nytimes.com/2019/09/12/business/suv-sedan-detroit-fight.html

[17] T Krauthammer, H M Shanaa, A Assadi. (1994). Response of structural concrete elements to severe impulsive loads. *Computers & Structures*, 53(1), 119-130.

[18] T Krauthammer, N Bazeos, T J Holmquist. (1986). Modified SDOF Analysis of RC Box-Type Structures. *Journal of Structural Engineering*, 112, 4.

[19] R French, E Maher, M Smith, et al. (2017). Direct shear behavior in concrete materials." *International Journal of Impact Engineering*, 108, 89-100.

[20] H Broer, F Takens. (2010). *Dynamical Systems and Chaos*. Springer New York Dordrecht Heidelberg London.

# Fatigue Issues of BFRP Protective Door in Metro Tunnel Subjected to Train-Induced Wind Pressure

*Jialu Ma[1], Wuhan Li[2], and Zhenxing Zhang[3]*

[1] Associate Professor, Institute of Engineering Mechanics, China Earthquake Administration, jialuma@163.com.

[2] M. C. E, Institute of Engineering Mechanics, China Earthquake Administration, limingzhong0928@163.com.

[3] M. C. E, School of Civil Engineering, Northeast Forestry University, 2984477030@qq.com.

**Corresponding Author: Jialu Ma, PhD, Associate Professor.**

29 Xuefu Road, Harbin, Heilongjiang Province, China, 150080

**Email:** jialuma@163.com

## ABSTRACT

The protective door, in the tunnel between two metro stations, plays a very important role. Traditionally, it is made by steel. However, the steel doors are easy to corrode in the dark and humid environment, which leads the potential risk. With the advantages of lightweight, high-strength, corrosion-resistant, the basalt fibre-reinforced polymer (BFRP) protective doors have been used in protection projects recently. In the metro tunnel, the train-induced wind pressure will cause effects on the door, such as vibration, even fatigue issues. In this paper, a new type of BFRP protective door was setup by ABAQUS, the responses under the train-induced wind pressure were investigated. In addition, the fatigue issues were studied. The simulation results show that the BFRP protective door is always keep in elastic range when the train passing with the normal speed. S-N Curve method was used to both the BFRP and steel parts for judging the fatigue issues. It shows that there is no fatigue concern for the new BFRP protective door during its design life-cycle of 50 years.

***Keywords:*** *BFRP, Protective door, Fatigue, Train-induced wind pressure.*

## INTRODUCTION

Due to the restrictive effect of the tunnel walls, the metro pushes on the tunnel air as it moves through the interval tunnel. The front part of the metro presents a positive pressure, while the rear part presents a negative pressure. Under this circumstance, the gas will be pushed out of the tunnel and into the next station, and part of it flows from the front to the rear through the annular space between the train and the tunnel, thus creating a train-induced wind [1-9].

The protective door, in the tunnel between two metro stations, plays a very important role. Traditionally, it is made by steel. However, the steel doors are easy to corrode in the dark and humid environment, which leads the potential risk. With the advantages of lightweight, high-strength, corrosion-resistant, the basalt fibre-reinforced polymer (BFRP) protective doors have been used in protection projects recently. In the metro tunnel, the train-induced wind pressure will cause certain effects on the door, such as vibration, even fatigue issues.

In this paper, a new type of BFRP protective door was setup by ABAQUS, the responses under the train-induced wind pressure were investigated. In addition, the fatigue issues were studied. The simulation results show that the BFRP protective door is always keep in elastic range when the train passing with the normal speed. S-N Curve method was used to both the BFRP and steel parts for judging the fatigue issues. It shows that there is no fatigue concern for the new BFRP protective door during its design life-cycle of 50 years.

## Train-induced wind pressure

To study the effect of train-induced wind on the performance of metro tunnel interval doors, the first step is to find the train-induced wind pressure when the metro passes through. There is no direct access to the existing research results related to the train-induced wind on the interval door. However, a large number of metro platform screen door on the role of the train-induced wind had been carried out. In the daily working condition, protective door is keeping on its open state, the door is parallel to metro, which is very similar to train-induced wind pressure on metro platform screen door.

Kim recorded the wind pressure load on the fully closed screen door through on-site measurement in Seoul Line 2 (shown in Figure 1). They had systematically recorded and studied the time history of the train-induced wind pressure with different conditions, including the train entering the station, passing the station, and staggering the train, as well [1].


**Figure 1.** Train-induced wind pressure measurement device.

The test results show that the maximum wind pressure occurs when the head of the train passes through the station. The test results show that the maximum value of the wind pressure of the train-induced wind appears at the moment that the head of the train passes the measurement point, and the wind pressure quickly becomes negative after the train passes.

The measured data of the train-induced wind for Case 3 (speed of 62 km/h) recorded by Kim et al.[1] were used as the input load for the following analysis (shown in Figure 2). The maximum value of the train-induced wind pressure of 14.8 kgf/m$^2$ was converted to the International System of Units (SI) of approximately 145.14 Pa.

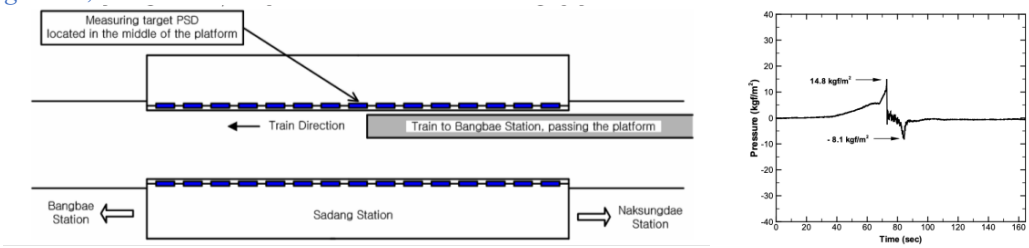


a) Condition of Case 3 b) Wind pressure

**Figure 2.** Train-induced wind pressure measurement.

## Finite element model of protective door

ABAQUS software was used to establish a new BFRP protective door finite element model containing the door plate, door frame, pre-embedded parts and connecting parts, as shown in Figure 3.

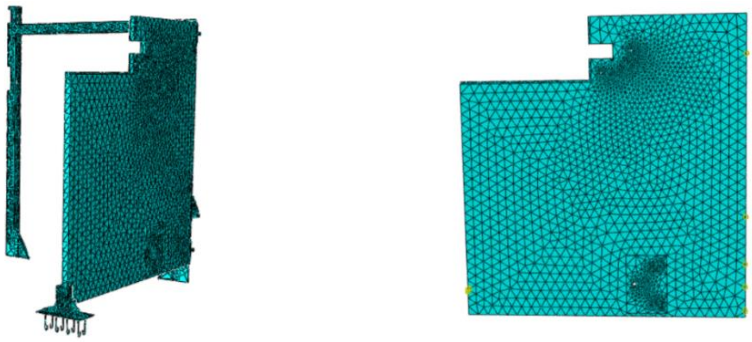

**Figure 3.** Finite element model of BFRP protective door.

Although the BFRP belongs to orthotropic anisotropic materials, but the analysis of orthotropic anisotropic materials is mainly used to simulate the direction of the material damage. Due to the entire analysis process by the train-induced wind pressure value is very small, strength damage is hardly occurred. Therefore, the orthotropic anisotropic material constitutive model is not used in this analytical model, an elastic constitutive model is instead, and the specific values of material properties are shown in Table 1.

After convergence analysis and comparison, the final choice to use the grid division as shown in Figure 6 calculation model, the total number of cells in the model is about 55,000, in which C3D10 element was used.

**Table 1.** Material properties

| Material | Variables | | |
|---|---|---|---|
| | Densities t/mm$^3$ | Young's Modulus N/mm$^2$ | Poisson's Ratio |
| BFRP | $2.00 \times 10^{-9}$ | $4.5 \times 10^4$ | 0.29 |
| Q235 steel | $7.85 \times 10^{-9}$ | $2.1 \times 10^5$ | 0.30 |

The main loads were considered with gravity and train-induced wind respectively. The train-induced wind pressure was applied vertically to the side of the door plate near the railroad track

by using the measured data with Kim. With the door open, the weight is almost entirely borne by the load-bearing arm on the door shaft side. The upper and lower hinges on the door shaft side, as well as the locking system, which limits the deformation of the door in horizontal directions.

## Analysis of train-induced wind vibration

It can be known that the location of the maximum stress in the door panel under the action of train-induced wind is most likely to occur near the support. Therefore, the location of the stress maximum in the steel joint and in the composite material can be considered as the control parts of the fatigue issues.

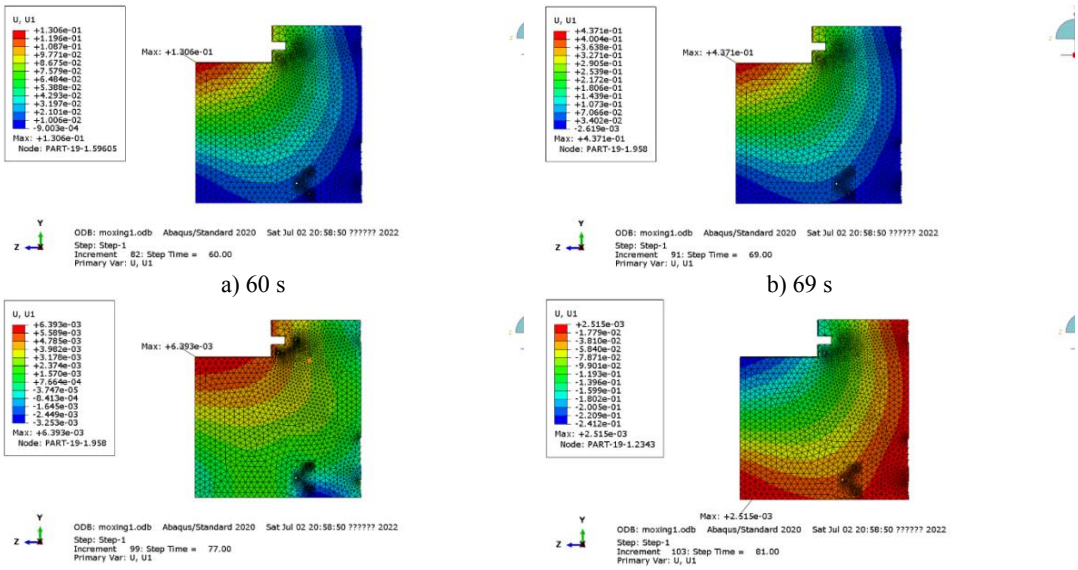


**Figure 4.** Vibration process of door under train-induced wind.

To understand the vibration process and its vibration amplitude, several typical moments in the process were listed, and the displacement contours of the door plate along the direction of the train-induced wind and the displacement-time curve of the maximum deformation position are plotted, which are shown in Figure 4.

According to the analysis data, the deformation of the door plate during the whole vibration process is very small, and the maximum moment occurs in 69 s with only 0.4371 mm. When other trains pass by, the vibration process occurs again and again.

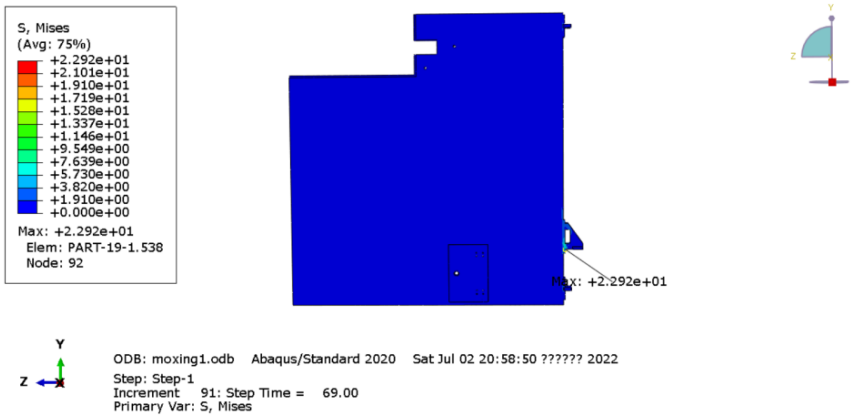


**Figure 5.** Stress contour of the interval door under the action of train-induced wind (69 s).

According to the analysis results, the maximum stress of the interval door in the whole process appeared at the 69 s, and the most unfavorable part was the corner weld connection between the load-bearing arm and the pre-embedded part, and the Mises stress contour was shown in Figure 5, and its maximum stress value was about 22.92 MPa.

The stress contour of BFRP was shown in Figure 6. Its maximum value is about 2.986 MPa, which occurs at the connection between the composite and the steel preload.

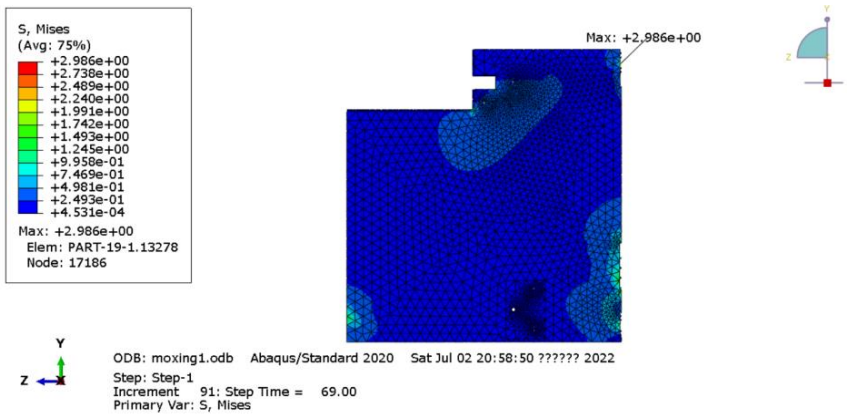


**Figure 6.** Stress contour of BFRP under train-induced wind (69 s).

From the results of the above analysis, under the action of train-induced wind caused by the metro, the stress value of the new BFRP protective door were small, and will not generate plastic deformation.

## Fatigue issue with different speeds

The metro section door is in the middle of the tunnel, and there is no slowing down or stopping of the metro during normal operation. The speed of the train passing through the gate is nearly by a constant velocity. Therefore, it is a constant fatigue issue. According to an average of one train passing through the metro every 3 minutes, 16 operation hours per day, and 365 days per

year, the total number of times the gate passes through the metro is about 5.84 million times within 50 years of its design.

S-N curve is commonly used in engineering to determine whether there is a fatigue issue. For the steel, the Chinese Code for design of steel structures (GB50017-2017) defined that the fatigue calculation adopts the traditional constructional classification method based on nominal stress amplitude. The stress concentration part is in the connection, which is classified as J1 according to its Appendix Table K.0.6, and the value of fatigue cutoff limit (100 million times) of J1 is 16 MPa, which is shown in Figure 7, according to the Table 16.2.1-2 in the Chinese Code [10].

$$\Delta\tau < [\Delta\tau_L] = 16\ \text{MPa} \tag{1}$$

The shear stress time course data of the weld unit with the largest stress position, its maximum value is about 4.726 MPa, and the minimum value is about 2.148 MPa, and its shear stress amplitude is about 2.578 MPa, which is far less than the fatigue cut-off limit of 16 MPa. It means that no fatigue damage will occur in the steel connection part of the door under its this condition.

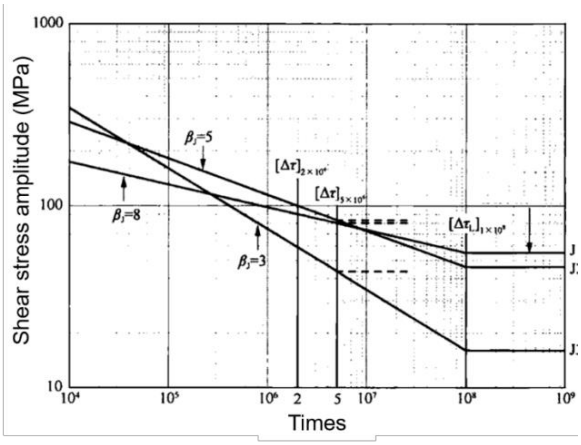


**Figure 7.** Fatigue S-N Curve for Shear Stress Amplitude in Chinese Steel Code [10].

The fatigue analysis methods for BFRP are slightly different from those for metallic materials. Their fatigue life is related to the stress level to which they are subjected.

The maximum main tensile stress of the composite material under the action of train-induced wind appeared in the position of the pre-embedded parts connection, and its maximum value was about 3.061 MPa. The ultimate tensile strength of the basalt composite material was 379 MPa, and the stress level was calculated to be about 0.008.

According to the S-N curve of BFRP material provided by the literature [11] (Figure 8), even if the lower curve was adopted in accordance with the data points in the figure with 97.5% guarantee rate, the fatigue life of BFRP material under this stress level was much larger than 100 million times. Therefore, it can be assumed that the BFRP parts of the protective door will not have fatigue issues under this condition.

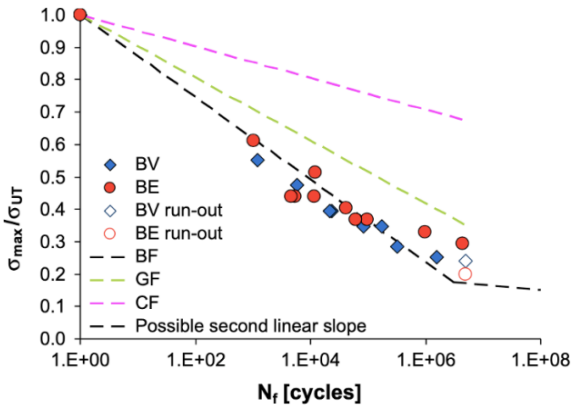


**Figure 8.** Fatigue S-N curve of BFRP [11].

In addition, the train-induced wind fatigue issues by different vehicle speeds were also studied. The usual speed limit of the metro is about 80 km/h. Limited to the fact that there is no field test data of train-induced wind pressure of other speeds. However, it is known that the train-induced wind speed is proportional to the train speed, and the train-induced wind pressure is proportional to the square of the train speed. Therefore, based on the measured data of Kim et al [1]. The train speed was increased as twice as 62 km/h, which is about 124 km/h. The wind pressure data was enlarged by four times, and its maximum value was increased to 580.56 Pa from the previous 145.14 Pa.

With the speed about 124 km/h case, the FE analysis results show that the maximum value of the maximum shear stress of is about 9.290 MPa, and the minimum value is about 0.004 MPa, with a shear stress amplitude of 9.286 MPa, which is lower than the fatigue cut-off limit 16 MPa as shown in Figure 7.

The maximum principal tensile stress of the composite material is about 8.821 MPa and a maximum value of about 1.580 MPa. The stress level is about 0.023, with the fatigue life of basalt fibre composites is also much larger than 100 million times (Figure 8). Therefore, it can be assumed that the new BFRP protective door will not experience fatigue damage within 50 years of its design cycle.

## CONCLUSIONS

The train-induced wind fatigue of a new BFRP protective door was investigated. The measured data of the train-induced wind formed by the metro crossing at a speed of 62 km/h was used as the input load. The dynamic response of the door under the action of the train-induced wind was numerically simulated using ABAQUS. Analysis results show that the train-induced wind acting on the new BFRP composite interval door, and the vibration amplitude is small. During that, the door body did not generate plastic deformation. Both the steel and BFRP parts of new BFRP protective door fulfil the fatigue requirements. It means that in the design cycle of 50 years, fatigue damage will not occur for the new BFRP protective door by train-induced wind pressure.

## ACKNOWLEDGMENTS

The research presented in this paper was jointly supported by the Scientific Research Fund of Institute of Engineering Mechanics, China Earthquake Administration (Grant No. 2023C08 and 2023D25) and the Natural Science Foundation of Heilongjiang Province, China (Grant No. LH2023E018).

## REFERENCES

[1] Kim, Jung-Yup. Field Experiment of Train-Induced Wind Pressure on Platform Screen Door at Subway Station [J]. *International Journal of Air-Conditioning and Refrigeration*, 2010, 18(04):309-316.

[2] D. C. Eckfordet al., The ventilation of metro systems with/without full height platform screen doors, *Proc. Eleventh Int. Symp. the Aerodynamics and Ventilation of Vehicle Tunnel* (2003) pp. 701–713.

[3] R. M. H. Yau and V. S. Y. Cheng, CFD analysis of pressure fluctuation due to train passage in tunnel, *Proc. Tenth Int. Symp. Aerodynamics and Ventilation of Vehicle Tunnel* (2000) pp. 953–965.

[4] Zhang G, Kim T H, Kim D H, et al. Prediction of micro-pressure waves generated at the exit of a model train tunnel[J]. *Journal of Wind Engineering and Industrial Aerodynamics*, 2018, 183: 127-139.

[5] Roh J S, Ryou H S, Yoon S W. The effect of PSD on life safety in subway station fire[J]. *Journal of Mechanical Science and Technology*, 2010, 24: 937-942.

[6] Qu L, Chow W K. Platform screen doors on emergency evacuation in underground railway stations[J]. *Tunnelling and Underground Space Technology*, 2012, 30: 1-9.

[7] Baron A, Molteni P, Vigevano L. High-speed trains: Prediction of micro-pressure wave radiation from tunnel portals[J]. *Journal of sound and vibration*, 2006, 296(1-2): 59-72.

[8] Sohn J R, Kim J C, Kim M Y, et al. Particulate behavior in subway airspace[J]. *Asian Journal of Atmospheric Environment*, 2008, 2(1): 54-59.

[9] Juraeva M, Ryu K J, Jeong S H, et al. A computational analysis of the airflow in a twin-track subway tunnel with a sliding-curtain to improve ventilation performance[J]. *Journal of Mechanical Science and Technology*, 2013, 27: 2359-2365.

[10] GB 50017-2017, Code for design of steel structures (In Chinese) [S].

[11] Colombo C, Vergani L, Burman M. Static and Fatigue Characterization of New Basalt Fibre Reinforced Composites [J]. *Composite Structures*, 2012, 94(3):1165-1174.

# PROTECT2024